

**INTERACTION OF BURNING METAL PARTICLES**

Final Report  
Contract No. NAS3-96017

Period Covered: 1 July 1996 - 31 August 1999  
NASA Contracting Officer's Technical Representative: Robert Friedman, Code 6711

Prepared by:

Edward L. Dreizin (Principal Investigator), Charles H. Berman, and Vern K. Hoffmann

AeroChem Research Laboratory, Titan Research and Technology, The Titan Corporation  
P.O. Box 2229  
Princeton, NJ 08543-2229

August 31, 1999

Submitted to  
NASA-Glenn Research Center  
Cleveland, OH 44135

1. Introduction .....	2
2. Constant Pressure Combustion of Aerosol of Coarse Magnesium Particles in Microgravity .	3
2.1. Introduction .....	3
2.2. Experimental .....	5
2.3. Results .....	7
2.4. Discussion .....	14
2.5. Summary .....	19
2.6. References .....	19
2.7. Figures .....	22
3. Further Experiments on Magnesium Aerosol Combustion in Microgravity .....	40
3.1. Introduction .....	41
3.2. Experimental .....	42
3.3. Results and Discussion .....	42
3.4. Concluding Remarks .....	47
3.5. References .....	48
3.6. Figures .....	49
4. Magnesium Aerosol Combustion Modeling .....	58
Figures .....	61
5. Combustion of Aerosolized Zirconium And Titanium Particles in Microgravity .....	64
5.1. Fine Zirconium Powders .....	64
5.2. Coarse Powders of Zirconium and Titanium .....	67
5.3. References .....	69
5.4. Figures .....	70
6. High Temperature Phases in Ternary Zr-o-n Systems .....	81
6.1. Introduction .....	81
6.2. Experimental .....	81
6.3. Results and Discussion .....	82
6.4. References .....	83
6.5. Figures .....	85
7. New Technology .....	87
8. Summary and Future Work .....	87
9. Acknowledgments .....	88

## 1. INTRODUCTION

Combustion processes in two-phase systems, such as sprays, dust clouds, and various aerosols, are of interest for numerous applications in propellants, explosives, and incendiaries. In addition, similar processes need to be characterized and understood for a number of fire suppression applications. However, experimental data characterizing combustion in two-phase systems and, specifically, describing effects of multiparticle interaction on the flame propagation, are limited. This, primarily, is due to difficulties in organizing an experiment that would enable a researcher to establish a flame in a two-phase system and, at the same time, observe behavior of individual particles. One crucial problem is that in two-phase systems in which flame propagation can be established the size of the particles is small and they are hard to distinguish optically. Another problem is associated with strong buoyant flows induced in a cloud when a flame starts to propagate. These buoyant flows entrain particles and mask particle motion induced by diffusiophoretic and thermophoretic flows and other possible particle interaction mechanisms (e.g., induced electric fields). However, particle interaction effects are expected to be significant and cause changes in the flame propagation mechanism, affect the size and morphology of combustion products, and modify the temperature and concentration gradients developing in a burning two-phase system.

Experiments in which combustion of two-phase systems is carried out in the microgravity environment allow one to avoid production of buoyant flows. In addition, large particles can be used, that will remain aerosolized (i.e., will not fall down as they would at normal gravity) so that their behavior ahead, behind, and within the propagating flame can be observed using optical techniques routinely used in single particle combustion studies. This approach has been exploited in this program, in which microgravity combustion of coarse metal particle aerosols was addressed. A new experimental setup has been designed, built, and tested. This setup has been used in more than one hundred of microgravity experiments utilizing NASA Glenn 2.2 s drop tower. Experiments with Mg, Zr, and Ti aerosols were conducted and a number of new and interesting phenomena characterizing combustion in these aerosols were observed. The selected metals represent two different metal groups, namely, a typical "vapor-phase burner", Mg, and typical "surface burners", Zr and Ti. Experiments were conducted at constant pressure and used real-time diagnostics included a high speed movie camera and a regular speed video camera equipped with microscope lenses and various interference filter assemblies. Combustion products were collected and analyzed after the microgravity experiments.

Most of the results of this effort have been reported in conference proceedings and peer-reviewed journals. Verbatim copies of the peer-reviewed publications follow below as the report chapters 2, 3, and 6. Chapter 4 briefly describes a developed numerical model of the flame propagation in magnesium aerosol in microgravity. Chapter 5 describes currently unpublished results of microgravity experiments with Zr and Ti particles. The final chapter 7 discusses general conclusions and recommendations for future research.

## 2. CONSTANT PRESSURE COMBUSTION OF AEROSOL OF COARSE MAGNESIUM PARTICLES IN MICROGRAVITY

Reference: Combustion and Flame 118:262-280 (1999)

### ABSTRACT

The combustion mechanisms of clouds of metal particles are addressed in this research. A microgravity environment was used to create a "stationary model aerosol" consisting of relatively large (100-300  $\mu\text{m}$  diameter), initially motionless particles. The development of individual particle flames, motion of individual particles, and overall aerosol combustion process could be observed simultaneously. The experiments used the 2.2 s Drop Tower at the NASA Lewis Research Center. Various image analysis procedures were employed to extract information on the flame structure from the high-speed movie and video records. Mg particle aerosol combustion at constant pressure was addressed. The observed flame structure contained pre-heat and combustion zones typical of the volatile type aerosol flames. The pre-heat and combustion zones were identified by differences in intensity and spectral content of the emitted radiation. The velocity of propagation of the pre-heat zone into the unburnt mixture was in the range of 0.15-0.30 m/s, consistent with the microgravity flame speed measurements reported in the literature. The combustion zone propagated at a slower rate of less than 0.1 m/s. The width of the pre-heat zone increased and the width of the combustion zone decreased during the flame propagation. Particle inertia caused significant velocity lag relative to the cold gas that was pushed ahead of the flame. The particles were, however, efficiently entrained by the hot gas in the pre-heat and combustion zones. Thus, the particle number density in the pre-heat and combustion zones increased as the flame propagated, eventually resulting in flame quenching due to oxygen deficiency. Also, collective particle motion was observed in the direction opposite to that of the flame propagation; the nature of this motion needs further investigation. Unburnt metal particles were observed to re-ignite when fresh air from the constant pressure ballast reservoir returned to the combustion chamber as it cooled.

### 2.1. INTRODUCTION

Multiple particle/droplet flames are ubiquitous in practical combustion systems, and thus the multiple particle flame interaction processes are of great practical importance. This explains the strong current interest in interactive combustion phenomena. Numerous theoretical and experimental combustion studies of liquid fuel drop arrays have been conducted to determine the interaction effects. Major results in this field were recently summarized in a comprehensive review [1]. Recent experiments with two adjacent liquid droplets burning under microgravity conditions [2,3] revealed new aspects of flame interaction processes, such as "positive" and "negative" interactions, which can either increase or decrease burning rates depending on the droplet separation and the combustion stage. Interaction of solid fuel flames has been studied only for bulk samples and for relatively low temperature flames [4-6].

Although metals are widely utilized in solid propellants and in explosives involving multiple interacting metal particles, no direct experimental studies of the burning metal particle interactions

and their effect on flame propagation have been reported. Apparently, this is due to experimental difficulties associated with studying metal aerosol combustion behavior while simultaneously analyzing the processes occurring with individual particles. Individual particle behavior cannot be optically resolved in a burning metal cloud because only very fine (1-10  $\mu\text{m}$  particle size range) and relatively heavily loaded metal aerosols can be ignited and burned. Thus, only gross parameters describing cloud combustion are recovered from aerosol combustion experiments. The structure of the metal aerosol flame is not usually expected to be homogeneous, instead it is anticipated to consist of multiple single particle flame substructures, i.e., Nusselt type of aerosol flame [7]. This structure, however, has never been experimentally identified for metal aerosols. The relationship of the general cloud flame structure and combustion scenario with the specific features of combustion of individual particles could be better understood if larger size particles were used in experiments, so that both the individual particle behavior and the common cloud combustion characteristics could be simultaneously observed. However, it is impossible to produce and burn a stable aerosol of large metal particles because of rapid gravitational settling.

Microgravity provides a unique opportunity to create a "model aerosol" consisting of relatively large (100-300  $\mu\text{m}$  diameter) particles. Combustion of such particles in a cloud can be studied using methods developed in single particle combustion experiments. In microgravity, the particles will not settle, rather their motion will be due exclusively to the forces originating during combustion. Therefore, individual flame development, particle trajectories, temperature histories, smoke transport, etc., in this "model aerosol" will simulate many features of an actual fine metal aerosol combustion. Clouds with different metal type particles and with different particle number densities can be readily created in microgravity, which allows detailed experimental investigation of the processes caused by the interaction of burning metal particles.

Our current understanding of individual metal particle combustion suggests that there are many processes which significantly affect metal aerosol combustion but do not occur in clouds of non-metal particles, which burn at lower temperatures, or in liquid fuel sprays. Among such processes are efficient radiative heat transfer caused by the high combustion temperatures [7,8] and changes in the reaction mechanism during combustion (the transitions from heterogeneous to vapor phase combustion and from spherically symmetric to non-uniform combustion, the occurrence of microexplosions, and temperature jumps [9-13]). Different combustion products and intermediates, including those formed as a nanoscale condensed phase [14], are produced during combustion and participate in further multi-step reactions. Both the particle surface layer and the particle internal composition are modified during combustion [15]. Ionized species and electrically charged particles are efficiently produced at high metal combustion temperatures for low metal ionization potentials [16,17]. These processes affect particle interactions and can be crucial for the performance of practical devices utilizing metal combustion.

This paper presents the first experimental results of an investigation of the combustion parameters of microgravity "model aerosols": size classified, relatively large metal particles aerosolized in the microgravity environment.

## 2.2. EXPERIMENTAL

### *A. Objective and approach*

The objective of the experiments is to create a stationary model aerosol of relatively large particles to study the development of individual particle flames, motion of individual particles, and overall aerosol combustion process. The experiment consists of the following steps:

- a) aerosolizing 100-300  $\mu\text{m}$  diameter metal particles in an oxygen-containing environment under microgravity,
- b) ignition of the aerosol using a local high energy density heat source,
- c) simultaneous observations of both the entire aerosol combustion and the behavior of single burning particles.

### *B. Experimental Hardware*

A simplified schematic of the experimental apparatus designed and built for the microgravity experiments utilizing the 2.2 s Drop Tower at NASA Lewis Research Center, is presented in Fig. 2.1. The central part of the experimental apparatus is an approximately 0.5 liter chamber in which an aerosol is created. It is built of aluminum and is equipped with two Lexan® windows, three gas-ports, and two electrical feedthroughs. The chamber's floor is a silicone rubber membrane which aerosolizes the powder using acoustic oscillations transmitted from an acoustic exciter. The chamber is mounted on top of the acoustic exciter and connected to a large, 11.3 L (3 gal) reservoir via 0.93 cm (3/8") diameter, 1 m long tubing. The reservoir served to prevent pressure build-up in the combustion chamber during the experiments. A metal mesh (filter) is installed in the line between the combustion chamber and the reservoir to retain the particles in the combustion chamber. The reservoir, in turn, is connected back to the approximately 11 L acoustic exciter vessel housing a speaker. The 0.93 cm diameter line from the reservoir to the acoustic exciter is also about 1 m long. An additional miniature inert gas tank is connected to the combustion chamber through a normally-closed solenoid valve. A second solenoid valve is installed in a vent from the reservoir chamber to atmosphere. Before the end of the microgravity experiment, both solenoid valves are activated and the combustion chamber is flushed with an inert gas to quench the reaction.

A sketch (to scale) of the combustion chamber is shown in Fig. 2.2. The chamber dimensions are 102×110×45 mm. However, in order to make the flame optically transparent, a narrower zone of 60×60×19 mm, is restricted in the middle of the chamber by two transparent 13 mm thick Lexan® inserts. Aerosol is ignited using an electrically heated (30 W DC power) 100  $\mu\text{m}$  diameter tungsten igniter wire mounted inside the chamber. To minimize the effect of tungsten oxidation on magnesium particle cloud combustion, the igniter wire was coated with a thin layer of a zirconia-based paste that forms a refractory solid coating capable of withstanding temperatures up to 2200°C. The typical shape of the flame front that would form in microgravity experiments and the field of view of a high-speed movie camera (30×21 mm) are also shown in Fig. 2.2. The location at which the camera has been focused, was varied from experiment to experiment (for example, in some experiments a portion of ignition wire was included in the corner of the field of view), however the

size of the field of view remained essentially unchanged. The high-speed images constricted within this field of view (as shown in Fig. 2.2) have been used to examine the flame structure and particle motion, as discussed below. Because only a small portion of the flame was within this field of view, the curvature and the changes in the flame shape occurring during the experiment have not affected noticeably the recorded high-speed images of the flame. The field of view of the regular speed video camera normally included the entire 60×60 mm area restricted by the Lexan® inserts.

Electronic components mounted on the experimental rig include an audio generator, an audio amplifier, a 12 V DC dry cell battery, and a regulated power supply for heating the ignition fuse wire. In addition, the apparatus includes a custom-built triggering circuit.

The diagnostics used in the experiments included a video camera and a high-speed movie camera. The video camera was used to obtain an overall picture of the flame. To better understand processes occurring in the flame front it was desirable to separate flame radiation bands generated by the MgO and Mg vapors from the black body radiation. In order to do that, an additional optical system consisting of two slightly tilted relative to each other mirrors and two interference filters was installed in front of the video camera in certain tests. The two images, taken through a different interference filter each, were spatially separated and recorded in each video-frame. In that way it was possible to separate and directly compare two radiation patterns that were measured at exactly the same time. Interference filters for 500 and 520 nm were used to separate the Mg and MgO vapor phase radiation bands, respectively [18]. The high speed movie camera was used to resolve detailed particle trajectories and the development of individual particle flames using both dark field and bright field settings. In the dark field setting, the flame was the sole source of light, and with a bright field setting, a tungsten light bulb was used to illuminate the background, so that particles were visible independent of the flame luminosity.

Preliminary normal gravity tests were performed to evaluate the aerosol particle number density as a function of the floor vibration frequency. The number density of the aerosolized particles was evaluated based on the measured attenuation of 670 nm laser radiation. A laser diode and a photodiode with filter were mounted on a linear slide outside the combustion chamber; they could be moved together to different vertical and horizontal positions, and could be removed prior to ignition to provide a clear view for the video-camera.

### *C. Microgravity experiment sequence*

When a microgravity test starts, the acoustic exciter is turned on for a 0.4 s interval that results in aerosolizing particles in the combustion chamber. Since the frequency of the acoustic oscillations of the chamber floor is above 150 Hz, an interval of 0.4 s provides at least 60 complete vibrations to aerosolize particles. After the acoustic exciter is turned off, a time delay is provided so that the velocities of particles decrease due to aerodynamic drag. The relaxation time,  $t$ , for the velocity of an airborne particle is  $t=(2\rho r^2)/(9\eta)$  [19], where  $\rho$  is the particle density,  $\eta$  is gas viscosity ( $\eta=1.8\cdot 10^{-5}$  kg/(m·s) for room temperature air), and  $r$  is particle radius. For the Mg particles in the 100 - 300  $\mu\text{m}$  size range, the relaxation time is in the range of 0.05-0.48 s. In the experiments, the

ignition delay varied from 0.2 to 0.3 s that was sufficient for deceleration of most of the particles. After the delay, the tungsten wire is rapidly heated (it reaches a temperature above 1000°C in less than 50 ms, as measured optically) and the aerosol ignites. The entire aerosol combustion event usually occurs within 0.5-0.8 s. After a time delay of 1.9 s measured from the beginning of the test, the solenoid valves are activated to flush the combustion chamber with an inert gas and quench all post-combustion reactions.

#### *D. Metal Powder Used*

Magnesium was chosen for the first group of micro-gravity experiments since it has been shown previously that even 100-200  $\mu\text{m}$  size aerosolized magnesium particles can be easily ignited [20]. Particles used in our experiments were purchased from Aldrich Chemical. The particle size distribution was determined using digitized video-images of particles taken with a camcorder equipped with close-up lenses. The camcorder resolution was 20  $\mu\text{m}$ . Particle diameters varied in the range of 100-550  $\mu\text{m}$ , however, more than 80 % of the particles had diameters in the range of 100-320  $\mu\text{m}$ . For a series of tests particles were preliminarily size-classified using a set of precision sieves of 150, 180, 250, and 350  $\mu\text{m}$  opening sizes.

### 2.3. RESULTS

#### *A. Preliminary Normal Gravity Experiments*

Preliminary experiments were conducted to define conditions needed to ignite particles and to better evaluate timing for microgravity tests. Based on the laser light attenuation measurements, it was found that the maximum number density aerosol was formed in the combustion chamber when acoustic oscillations with frequencies ranging from 150 to 200 Hz were used. For frequencies exceeding this range, the amplitude of the oscillations of the silicone rubber floor dropped dramatically. Using the acceleration of the silicone rubber floor estimated from the vibration frequency, the measured vibration amplitude, and a theoretical study [21], it was estimated that only about 10% of the total particles loaded could be suspended more than 15 particle diameters (approximately 3 mm) above the rubber floor. Accordingly, light attenuation measurements determined that the magnesium particle number density decreased by a factor of 5 as the height increased from 55 to 80 mm from the chamber floor (the chamber could only be viewed through a window above the height  $h \approx 40$  mm from the floor). Since the middle of the igniter wire was located approximately 70 mm above the chamber floor, only a very small fraction of the total particle mass load could participate in the aerosol ignition. Even though in these normal gravity tests the particle loading was much greater at the chamber floor, it was not anticipated that the flame would propagate downwards, due to buoyancy. It was found that to achieve ignition in these normal gravity experiments, the total mass of the magnesium particles loaded had to exceed 5 g, whereas only 0.21 g of magnesium would be needed to achieve an equivalence ratio of unity ( $\phi=1$ ) based on the total amount of oxygen in the 0.5 L chamber. Due to the decrease in the particle number density with height, when 5 g of powder was loaded in the combustion chamber, the particle concentration at the level of the middle of igniter wire was only 0.075 g/l, corresponding to approximately 20 particles



per cubic centimeter, or an inter-particle separation of about 0.37 mm. The corresponding equivalence ratio  $\phi$  (estimated for 200  $\mu\text{m}$  diameter particles) was only 0.34. However, it became greater (close to 0.7) at the bottom of the igniter wire.

Several normal gravity ignition experiments were conducted using a high-speed video camera to visualize flame propagation. Examination of the video-recordings revealed that multiple particles adhered to the surface of the igniter-wire prior to heating and ignited when the wire was heated. Later on, the multiple particle cloud flame developed and burned in the chamber. The overall flame development process is illustrated by high-speed video-images presented in Fig. 2.3. The first frame in Fig. 2.2 shows how the flame ignited around the tungsten wire (indicated by a dotted line) and spread upward vertically, which, apparently was the result of buoyancy. Later on, as shown on the following two frames, the flame width increased at a rate of about  $\sim 0.1$  m/s and reached up to 35-40 mm for 100-150 ms. The flame width was later observed to decrease and the entire lifetime of the visible flame was around 300-350 ms prior to flame extinguishment. This flame lifetime can be compared to the combustion time of single magnesium particles in air. For a 200  $\mu\text{m}$  diameter (close to the average particle size in the aerosol used) particle, the combustion time in air is 80 ms [18], i.e., it about 4 times shorter than that observed in our experiments. Based on this comparison it can be concluded that not only ignition and burn-out of a group of single particles adjacent to the igniter wire, but also actual (even though limited) flame propagation into the aerosol was observed in these experiments. After the flame extinguished, several particles could still continue to burn, and from time to time a cluster of particles could ignite.

The horizontal width of the flame zone,  $w$ , and the velocity of the flame front (in the horizontal direction)  $v_f = dw/dt$ , were derived from a high-speed video-record. The width of a bright zone at a fixed vertical level was measured, as indicated in Fig. 2.3. As can be seen from Fig. 2.3, this width was somewhat different at different vertical levels due to curving of the flame zone edges. To choose the vertical level at which the measurements were to be made, the video-record was reviewed and the level at which the curvature appeared to be minimal, was identified. Typical results of these measurements are shown in Fig. 2.4. The inferred flame velocity is in the range reported earlier for large particle size magnesium aerosol flames [20, 22]. Oscillations observed in the flame velocity plot appear random, but similar oscillations were observed for all of the experiments.

## *B. Microgravity Experiments*

### Microgravity aerosol

In the first series of drop-tower experiments, unclassified (as-received) Mg powder was used and mass loadings were varied from 0.65 to 5.4 g (0.21 g would correspond to  $\phi=1$ ). It was found that only 0.7 g total mass load was necessary to achieve repeatable aerosol ignition and flame propagation in microgravity (versus 5 g needed in the normal gravity experiments). In the following experiments, three size-classified powder fractions were used with particle diameters  $d_1 = 165 \pm 15$   $\mu\text{m}$ ,  $d_2 = 215 \pm 35$   $\mu\text{m}$ , and  $d_3 = 300 \pm 50$   $\mu\text{m}$ . For each of these powder fractions, the mass loadings were 0.7, 1.1, and 1.6 g.

Before ignition, aerosolized particles were visualized using the bright field optical setting. Some of the particles were observed to adhere to the windows and did not move during the experiment, and these particles were excluded from the particle count. It was observed that the aerosolized (i.e., observed to move) particles were scattered throughout the chamber quite uniformly, unlike the previously discussed normal gravity experiments. The anticipated distance between the uniformly distributed particles with an average diameter  $d$ , density  $\rho$ , and the total mass loading,  $M$ , can be roughly estimated as  $l \approx (V/N)^{1/3}$ , where  $V = 0.5$  L is the chamber volume and  $N = M/(\pi d^3 \rho / 6)$ , is the number of particles in the chamber. Based on the loadings used, these expected distances between the particles varied in the range of 85 to 260  $\mu\text{m}$ . The actual distances between the aerosolized particles determined from the video-images were much greater, in the range of 700 - 3500  $\mu\text{m}$ . The discrepancy of the expected and actual inter-particle distances was most likely due to partial adhesion of the powder to the chamber walls and floor. Based on the number density of the aerosolized particles in the combustion chamber observed in the video-images, it could be concluded that the equivalence ratio  $\phi$  in the microgravity experiments varied in the range of 0.25 to 5 depending on particle size and mass loading. This initial equivalence ratio, however, did not remain constant during our constant pressure experiments since unburnt gas was forced out of the chamber by the hot expanding burnt gas while most of the particles stayed in the combustion chamber, as discussed below.

#### General Flame Front Shape

Flame propagation through aerosolized magnesium particles in microgravity experiments differed significantly from that observed in normal gravity. After the igniter wire was heated, a bright radiating zone (flame front) was formed parallel to the igniter. Later on, this flame front propagated through the chamber leaving a darker area behind even though the wire igniter continued to be electrically heated (Fig. 2.5a). Such dark area behind the flame front was never observed in the normal gravity experiments in which the luminous flame zone only appeared to widen around the igniter wire rather than propagate away from it as in these microgravity experiments. Alternatively, the original flame front could split into several shorter fronts propagating in different directions and with somewhat different speeds (Fig. 2.5b). In the video-images recorded without filters installed in front of the camera (as those shown in Figs. 2.5 a,b), one can see both bright spots and an extensive radiating zone, making it hard to decide whether the flame front consisted of a number of closely spaced individual particle flames, or it was filled uniformly with burning magnesium vapor. When normal speed video was recorded using interference filters separating Mg and MgO radiation bands, the luminous zone indicative of the flame front appeared very uniform with no traces of individual particle flames (cf. Fig. 2.5c).

In most cases, the flame front was observed to travel through the chamber until it reached the wall. However, at lower particle loadings, it was also observed that the flame could disappear (extinguish) in the middle of the chamber.

### Structure of the Flame Front

Higher spatial resolution flame images were produced using the high-speed camera equipped with a close focus lens. These images showed that both brightness and the dominating color are different for different regions of the flame. Assuming that the flame consisted of pre-heat and combustion zones, a separation of these zones was attempted by comparing the red (650 nm central wavelength) and green (540 nm central wavelength) components of the high-speed color video-images of the flame (obtained by transferring the high-speed movie into the video-format). Green radiation was expected to dominate in the combustion zone due to the strong characteristic radiation bands at the wavelengths of 518 and 500 nm for Mg and MgO vapors, respectively [23, 24]. In the pre-heat zone, where particles are expected to be heated but not burned, the spectrum was expected to be closer to that of a gray-body radiator, and thus red radiation was expected to dominate.

The three color components of the video-signal, blue, green, and red were digitally separated for each (digitized) video-image. Color-Differential (C-D) images were then produced by the digital subtraction of the red component images from the respective green component images. The value  $I_d$  ascribed to each pixel in a C-D image was equal to  $I_d = I_{\max}/2 + (I_g - I_r)$ , where  $I_g$  and  $I_r$  are the intensities measured for the same pixel in green and red component images, respectively, and  $I_{\max}/2$  is a constant medium (gray) intensity level. Examples of an original video-image and the corresponding C-D image are shown in Fig. 2.6. The C-D images showed that green radiation indeed consistently dominated in the brighter flame zone, and they also revealed that a region where red radiation dominated always existed ahead of that zone. These two parts of the visible flame will be referred below as the combustion and pre-heat zones, respectively. Widths of the combustion and pre-heat zones were measured using intensity profiles inferred from the C-D images. An example of such a profile is shown in Fig. 2.7. A reference background level marked by a dashed line indicates the gray level on the C-D image produced when the values of the red and green intensity signals were the same. The intensity profile was under the background (gray) level when the red radiation intensity (assumed to characterize the black body radiation) was greater than green, and it is above the background level when the green radiation intensity (indicative of the Mg and MgO bands) was greater than red. For reference, an intensity profile measured for the corresponding original image (transformed into gray scale) is also shown. It indicates a monotonic increase in the general radiation intensity throughout the pre-heat zone, and essentially continuous radiation intensity within the combustion zone.

### Temporal Flame Evolution

For better visualization of the temporal flame evolution and also the particle velocities, artificial Time-Differential (T-D) images were constructed digitally (similar to the C-D images) as a difference between two flame images recorded at a known time interval  $\tau$ ; for example,  $\tau=30$  ms, for a pair of the sequential regular video-frames. An example of an artificial T-D image produced as a difference between two sequential high-speed movie frames (first transformed to the video-format and then digitized), is shown in Fig. 2.8. For this T-D image,  $\tau=2.5$  ms, and the areas that did not change during that time period, appear gray. The difference in the position of the flame front

produced bright and dark zones indicating the displacement of the leading and the trailing edges of the flame, respectively. The width of the bright zone divided by the time between the images,  $\tau$ , yields the velocity of the flame's leading edge propagation and the distance between the bright and dark zones shows the flame width. It should be noted that the measurements based on the widths of the various zones of the T-D images discussed below should not be used for quantitative flame description, but rather for identifying the major qualitative trends. These measurements were made at a level perpendicular to the flame front. The location of the level was chosen arbitrarily where the minimal flame curvature was observed to develop.

Depending on what kind of the video-frames were used to produce the T-D images, the position and displacement of either the pre-heat or the combustion zones could be observed better. For example, the video-frames used to produce the T-D image shown in Fig. 2.8 were recorded using the high-speed movie camera equipped with the close focus lens. In these recorded images, both the pre-heat and flame zones were significantly brighter than the unburnt mixture. Therefore, the first bright zone in the corresponding T-D image clearly shows the displacement of the leading edge of the pre-heat zone (that is the first bright zone in the flame's T-D image), and the dark zone observed in the T-D image corresponds to the displacement of the trailing edge of the combustion zone. The normal speed video-frames recorded using an interference filter (either 500 or 520 nm) showed great contrast in the combustion zone and essentially cut off the red-color dominated radiation from the pre-heat zone. Therefore, the corresponding T-D images showed only evolution of the combustion zone, while the pre-heat zone became invisible.

Propagation velocities of the leading edge of the pre-heat zone were measured for several microgravity experiments using high-speed movies transformed to the video-format. One example of the results of such measurements, for Run # 20 ( $M=1.1$  g,  $180\text{ }\mu\text{m}<d<250\text{ }\mu\text{m}$ ) is shown in Fig. 2.9. The velocity of the leading edge of the pre-heat zone fluctuates about a value of 0.18 m/s. Generally speaking, this velocity can also be referred to as the flame velocity, since it indicates the visible rate at which the luminous flame zone propagates into the unburnt mixture.

The position of the edge of the combustion zone was also monitored in time for several experiments using regular video-frames recorded through a 500 nm interference filter. Figure 2.10 presents a typical plot of the measured coordinate of the leading edge of the combustion zone and the inferred velocity at which the combustion zone propagates. Oscillations in the combustion zone velocity were observed consistently in all the experiments, similar to those observed for the velocity of the leading edge of the pre-heat zone (Fig. 2.9). The oscillating pattern of the flame propagation could also be clearly seen in the video-records. The comparison of Figs. 2.9 and 2.10 shows that the combustion zone propagated slower than the pre-heat zone. This conclusion is further confirmed by comparisons of the radiation profiles constructed for sequential C-D images. An example of such profiles is shown in Fig. 2.11. It shows a substantial increase (from 7-8 to 15-18 mm) in the pre-heat zone width during the time when both combustion and pre-heat zones were within the camera field of view (approximately 50 ms). The displacement of the leading edge of the pre-heat zone was almost 10 mm while the leading edge of the combustion zone moved less than 2 mm. The trailing edge of the combustion zone moved about 5 mm, indicating that the width of the combustion zone

decreased slightly (approximately from 13 to 11 mm).

A plot showing the positions of the leading and trailing edges of the combustion zone, inferred from a sequence of T-D images produced using normal speed video-frames recorded through a 500 nm interference filter, is shown in Fig. 2.12. The shaded area indicates the width of the combustion zone observed at different times. Interestingly, it can be seen that combustion zone width changes non-monotonically during the experiment.

While no interference filters were used in the reference normal gravity experiments described above (Figs. 2.3,2.4), the measurements of the flame edges were made using the brightest zone, with approximately constant brightness across the horizontal axis. Therefore, the flame velocity reported in Fig.2.4 for normal gravity can now be interpreted more accurately as the velocity at which the combustion zone propagated. A legitimate comparison, therefore, can be made for the velocities reported in Fig. 2.4 versus those presented in Fig. 2.10 for the similar experiments conducted in the normal and microgravity conditions, respectively. This comparison shows that the absolute values for the combustion zone velocity measured in microgravity were generally smaller than those observed in normal gravity experiments. Similar velocity oscillations are observed for both environments.

A simpler data reduction routine was also used to directly determine times characterizing the evolution of the pre-heat and combustion zones identified from the recorded video. Temporal variations of the radiation intensity at a fixed location during the flame propagation were measured by monitoring signal intensity at the same coordinate (a chosen pixel in the image) using a sequence of high-speed frames. The results of these measurements for two different microgravity runs (20 and 30) are presented in Fig. 2.13. The difference between the two experiments was in using different size particles: 180-250  $\mu\text{m}$  and 150-180  $\mu\text{m}$  diameters were used in runs 20 and 30, respectively. A smooth increase of the radiation intensity in the post-flame zone observed in Fig. 2.13 for Run 30 is due to the continuously increasing brightness of the propagating flame front (that is clearly identified from the video recording) causing a brighter background as well. Similar increase in the flame brightness with time was observed repeatedly, but it was most pronounced for Run 30. The noticeable trend of a wider combustion zone associated with the larger particle size (i.e., Run 20 versus Run 30) was observed consistently in our experiments.

The time for the combustion zone to pass through a volume represented by a chosen point (pixel) was determined from Fig. 2.13. For Run 30 the time for the combustion zone to pass through the fixed point is close to 50 ms and for Run 20 that time is about 120 ms.

A common feature observed in both Fig.2.13 a and b is that intensity at a fixed point oscillates with time. The intensity often changes from one frame to the another, which makes it unclear whether there was a real luminosity change during that time period or if the framing rate was not fast enough to observe an actual (faster rate) change in the luminosity.

### Behavior of Individual Particles

As mentioned above, the particles were distributed quite uniformly in the combustion chamber prior to ignition. The T-D images constructed as a difference of two sequential video frames, were used to visualize particle motion. Each moving particle is represented in the T-D image as a pair of closely spaced dark and bright spots. A dark spot shows the particle location on the first video frame and a bright spot shows particle location on the second frame. The velocities of the particles' motion were evaluated based on the distances between light and dark spots signifying positions of each particle in sequential frames. It was observed that before ignition aerosolized particles moved with velocities in the range of 0.06 - 0.14 m/s and there was no preferred direction for their motion. After a flame front was developed, most of the particles visible in the pre-heat zone and in the unburnt gas, started to move with the velocities ranging from 0.05 to 0.25 m/s in the direction of the flame propagation. In most of the experiments, one could clearly identify one direction in which the particles would start to move, that direction was assumed to coincide with the direction in which a gas flow was forming due to the gas expansion in the flame. The fact that one direction of the gas flow could be identified for most of the experiments could be used to justify that a flame structure that has been examined using the high-speed video recordings was close to that of a one-dimensional flame.

For the particles adjacent to the flame front, the observed velocity was higher as compared to that for the particles far from the flame. This is illustrated by Fig. 2.14 showing two magnified fragments of one T-D image. One can clearly see that particles positioned 8 mm from the flame front moved faster than particles positioned 20 mm from the flame. It was also observed that particle number density immediately ahead of the flame front was increased compared to the original number density. To measure the particle number density, an area (20×20 mm) was selected on a T-D frame and the total number of particles within that area was computed. This was repeated for a series of sequential frames from the moment of aerosol ignition to the moment the bright flame zone entered the selected area. The results of these measurements are presented in Fig. 2.15 showing how the particle number density within a selected region changes when a flame front approaches this region. The initial number density (at time = 0) was obtained from an image taken before ignition, this number density did not change noticeably during the first 10 ms after the igniter wire (located approximately 7 mm away from the selected area, became clearly visible. Later on, as can be seen from Fig. 2.15, the number density of particles increased rapidly as the flame front approached the selected area.

No motion pattern that would indicate either attraction or repulsion between the particles was observed. An example of a video-frame and a corresponding T-D image showing the general pattern of the motion of individual particles in the pre-heat zone and unburnt gas is given in Fig. 2.16a and Fig. 2.16b, respectively. Most of the particles observed in Fig. 2.16 b, move in the direction coinciding with the direction of the flame propagation (indicated by an arrow), as can be seen by the orientation of the adjacent dark and bright spots which indicate, as noted above, respectively initial and final positions of the particles. Particles could be seen in the unburnt gas mixture and the pre-heat zone, but they were not observed (with a few exceptions) within the combustion zone. An

interesting observation can be made from the close-up presented in Fig. 2.16c. Several particles (circled in Fig. 2.16c) appear to move in the direction opposite to that of the flame front and to that of the other particles. This motion becomes evident when an animation containing sequence of the T-D frames is produced. Such motion of a group of particles in the pre-heat zone against the main flow was observed in a number of experiments.

Individual particle flames were observed to form in the pre-heat zone. They would disappear when the combustion zone reached their location. Inside the combustion zone there was no visible individual particle flames. Separate single particle flames could sometimes be observed at a variety of locations in the post-flame zone.

In all the experiments, clusters of particles were observed that seemed to behave as one large (several millimeters diameter) burning particle. These clusters moved faster than the flame front and the direction of their motion was random. It appeared that the burning clusters self-propelled themselves, similar to single metal particles with asymmetric flames observed in the earlier microgravity experiments [25]. Examples of such clusters can be seen clearly in Figs. 2.8 (bottom center) and 2.16 (upper left corner of the area selected in Fig. 2.16b).

### Re-ignition

One striking observation was that in all the microgravity experiments a secondary violent ignition was observed. A sequence of video-frames showing extinction of the original flame front and subsequent re-ignition is shown in Fig. 2.17. The re-ignition always occurred after the original flame extinguished and there always was a delay on the order of a couple hundred milliseconds. A significant number of rapidly moving (often, in a swirling pattern) single burning particles was always observed. However, there was no clearly identified flame front, instead it appeared that a large number of scattered particles ignited simultaneously.

## 2.4. DISCUSSION

### Advantages and Limitations of the Experiment

An important advantage of this microgravity experiment was that a metal aerosol flame was formed allowing the simultaneous observation of both the cloud flame structure and individual particle behavior. In addition, due to large particle size and the absence of buoyancy driven flows, it was possible to identify details of the magnesium aerosol flame structure that were not possible to resolve in the previous experiments in normal gravity and also in the microgravity experiments using finer particles.

The most important limitation of this experiment was due to the “narrow cell” design of the combustion chamber used. This design made it possible to create an optically transparent flame. However, it inevitably introduced wall effects on both flow and temperature profiles in the flame that in turn could have affected flame speed and flame front width. Another experimental shortcoming

was that the number of particles aerosolized in the chamber depended on uncontrolled (even though, repeatable) processes of particle adhesion to walls and the floor; that introduced an uncertainty in controlling the aerosol number density. In addition, diagnostics were limited to only video and movie cameras due to restrictions on the room and power available in the drop-tower experiments.

### Re-ignition

The mechanism of the observed re-ignitions can be understood if flows induced in the combustion chamber and their interaction with the particles are considered. In these constant pressure combustion experiments, part of the unburnt gas was forced out of the combustion chamber when the burnt gas expanded. However, large magnesium particles did not move as fast as the gas and could have been “trapped” within the chamber. Some of the particles carried by the gas flow have been retained in the filter (as was confirmed when particles were found in the filter mesh after each experiment) and became unavailable for the secondary ignition since they stuck in the metal mesh and rapidly cooled down. Other particles that might have remained aerosolized within the combustion chamber, would have been pre-heated by (and partially burned in) the propagating flame. These aerosolized particles cooled slower than the gas and could re-ignite immediately if oxygen became available. After the flame’s extinguishment, the gas in the combustion chamber cooled down and occupied a smaller volume, therefore, a flow of air from the reservoir to the combustion chamber was produced. This flow carried oxygen into the combustion chamber and a re-ignition could occur if high-temperature metal remained in the chamber. Therefore, such re-ignitions, actually observed in some of our normal gravity experiments and in all of the microgravity experiments, present important (as discussed below) evidence that the incompletely reacted magnesium particles remained aerosolized in the combustion chamber after the flame extinguished.

### Flame Structure

Analysis of the flame images showed that pre-heat and combustion zones could be clearly identified by both radiation intensity and spectrum. At the same time, no structures similar to single particle flames were observed in the combustion zone. These observations indicate that the magnesium aerosol flame can be classified as “volatile” flame, according to Cassel [26]. Such a flame is normally controlled by the rate of fuel gasification while the chemical reaction occurs primarily in the premixed gas flame zone [7,26]. The pre-heat zone corresponds to the region where fuel is gasified but the reaction rate is slow. The existence of such a zone in the magnesium aerosol flame signifies that the magnesium evaporation rate reaches its maximum at a lower temperature than its reaction rate does. This conclusion is consistent with an estimate of the temperature dependent magnesium reaction rate:

$$k=k_0\exp(-E/RT)$$

where  $T$  is temperature,  $R$  is molar gas constant, and the values recommended in Ref [27] are used for the constant  $k_0=10^6 \text{ m}^3/\text{mol}\cdot\text{s}$  and activation energy  $E=40\pm5 \text{ kcal/mol}$ . At the magnesium boiling point,  $T=1380 \text{ K}$ , the reaction rate is quite small:  $k\approx 0.5 \text{ m}^3/\text{mol}\cdot\text{s}$ , whereas in a realistic flame temperature range,  $2000 \text{ K}<T<3000 \text{ K}$ , the reaction rate varies in the range of  $45\text{-}1230 \text{ m}^3/\text{mol}\cdot\text{s}$ .



The absence of the “Nusselt” kind of the flame structure [7, 26] consisting of multiple single particle flames and predicted to be typical for metal particles such as magnesium, for which the large oxide shells are known to form [7,26,28], was somewhat unexpected. When large aerosolized particles burn, as clearly was the case in these experiments, Nusselt flame structure is also normally anticipated to follow the volatile flame [7], however that was not observed. The re-ignitions occurring in our experiments show that a significant number of the unburned metal particles remained in the combustion chamber. Thus, in spite of the lean mixtures inferred in most experiments from our measurements for the number density of aerosolized particles prior to ignition, the complete burn-out of magnesium was not the reason for the absence of Nusselt type flame (or, multiple single particle flames) behind the volatile flame front. Another mechanism suppressing single particle flames could be oxygen deficiency. Different processes could cause the formation of a fuel-rich mixture in spite of the starting lower equivalence ratios (inferred from the measured particle number density). Due to the complexity of the experimental system, the conclusive analysis of these processes can only be accomplished based on the detailed modeling in which mass and heat flows are considered for both particles and gases. While development of such a model is currently in progress, it is possible to indicate several processes that could have caused oxygen deficiency. Soon after ignition, the particle inertia could result in a significant particle velocity lag relative to the gas quickly expanding in the pre-heat zone. Thus, most of the particles (only partially evaporated and burned) could be left within the combustion zone surrounded by low density (hot) gas. The observed increase in the particles number density ahead of the flame front (Fig. 2.15) indicates that other processes could have contributed to the formation of an oxygen deficient flame. Particles could have been “trapped” in the flame front due to significant difference in the viscosity of the hot gas (in the pre-heat zone) and cold gas ahead the pre-heat zone. The difference in the gas viscosity could thus have resulted in the significant particle velocity lag relative to the cold gas (with low viscosity) and much closer particle and gas velocities in the hot (highly viscous) gas. In addition, thermophoretic forces could have accelerated particles in the regions with strong temperature gradients, i.e., in the part of the pre-heat zone adjacent to the flame front. In fact, particles were observed to move faster in the vicinity of the flame front as compared to the particles positioned further in the unburnt gas (cf Fig. 2.14). As was noted above, the detailed understanding of the role of each of these and other processes affecting flame structure and evolution should await results of the current modeling effort.

### Temporal Changes in the Flame Structure

The present experiments did not show steady state flame propagation; instead, the observed rate of the flame propagation and the growth of the widths of the pre-heat and combustion zones changed during each experiment. This may not seem surprising considering the above mentioned limitations on the experimental geometry. However, even though the geometric limitations of the experiment preclude one from making quantitative conclusions, the observed flame speed evolution and temporal variations of the widths of pre-heat and combustion zones illuminate some qualitative mechanisms of the flame propagation.

It is useful to compare the rates of flame propagation observed in this research with the

burning velocities reported earlier for aerosols of magnesium particles in air. For normal gravity, the flame propagation velocity for aerosolized 30-220  $\mu\text{m}$  size magnesium particles was reported to be in the 0.5-0.75 m/s range [20]. For the microgravity environment, flame propagation velocities from 0.2 to 0.35 m/s were observed for magnesium particles of 34  $\mu\text{m}$  diameter [22]. In the microgravity experiments reported here, the pre-heat zone front velocity was observed to vary from 0.15 to 0.30 m/s (Fig. 2.9), that is in the same range as the previous microgravity observations [22]. However, the velocity of the combustion zone front (unresolved in the previous studies) was observed to be noticeably smaller, less than 0.1 m/s (Fig. 2.10).

Oscillations in flame velocity and radiation were consistently observed in both normal and microgravity experiments. In the normal gravity experiments they could be caused by a periodic additional supply of fresh particles into the combustion zone from the vibrating chamber floor. In the microgravity experiments, however, there was no pulsating supply of particles in the flame.

Similar oscillations were observed in many previous aerosol combustion experiments, for example in normal gravity [29] and in microgravity [30]. In contrast, steady flame propagation was reported for the microgravity experiments [22], in which, however, the time resolution of the diagnostics used could be insufficient to register the oscillations. Usually, oscillations observed in the flame front are associated with the exciting acoustic oscillations in the combustion chamber [7, 29, 30]. In these experiments, the characteristic frequency of the acoustic oscillations that would resonate in the combustion chamber was in the range of 10 kHz. This frequency is too high to be noticed using the high-speed movie camera utilized in these experiments. The oscillations observed in the flame velocity and width were of significantly lower frequency of about 100 Hz (with periods of several tens of milliseconds, Figs. 2.9, 2.10). They could, however, be caused by a reflection of an acoustic wave traveling through the tube from the combustion chamber to reservoir. Additional measurements would be needed to better identify the origin for these oscillations.

The observed experimental increase of the width of the pre-heat zone could simply be caused by the insufficient time available to establish a steady state temperature gradient ahead of the combustion zone. The trend of the combustion zone width to decrease could be qualitatively interpreted considering the increase in the particle number density in the combustion zone due to the difference in the hot and cold gas viscosities, as discussed above. That could have caused flame extinguishment in the internal, fuel-rich part of the combustion zone and thus the decrease in the width of the combustion zone. A more substantiated interpretation should rely on the quantitative modeling.

### Particle Motion

The most noticeable pattern of the particle motion was that in which particles followed the expanding gas flows, i.e., particles in the unburnt gas and in the pre-heat zone were observed to move away from the flame front. Since very large particles were employed in these experiments, the inertial lag between the particles and the gas must have been significant. It can be expected that such a lag could affect the flame propagation observed in these experiments. For example, since particles moved slower than the gas as the flame propagated, the number density of particles

“caught” in the pre-heat and flame zones increased. This could produce a richer mixture and higher combustion temperatures and rates, i.e., result in the flame acceleration. On the other hand, this faster reaction rate could eventually cause a local deficiency in the oxidizer, and thus slow down the flame propagation rate. It is therefore possible that such processes could have caused the observed oscillatory changes in the flame velocity.

The significance of the inertial lag between gas and particles in aerosol flames (usually ignored in dust combustion models) can be roughly evaluated by comparing the flame width with the particle stopping distance. For simplicity, a previously published model [22] for a magnesium aerosol flame was used to estimate the flame widths. A particle stopping distance,  $S$ , can be readily computed [19] using a gas velocity,  $v$ :

$$S = \frac{\rho_p v d_p^2 C_c}{18\eta}$$

where  $\rho_p$  is the particle density,  $v$  is the gas velocity (assumed to be equal to the flame front velocity),  $d_p$  is the particle diameter,  $C_c$  is the Cunningham slip correction factor [19], and  $\eta$  is the gas viscosity. The parameters that were substituted into the estimate were: flame velocity of 0.5 m/s [20], fuel to air ratio of 1 g/l of magnesium, and particle size range: 1 - 250  $\mu\text{m}$ . The gas viscosity was computed at two temperatures: 300 and 1300 K, i.e., room temperature and the Mg boiling temperature. The temperature in the pre-heat zone was (arbitrarily) taken to be 600 K and the temperature in the combustion zone was taken as 2600 K (these parameters are needed for Ballal’s model [22] estimate of the flame front width). The results of this estimate are presented in Fig. 2.18 as the ratio of the flame width to the particle stopping distance as a function of particle diameter. These results show that inertial phenomena have been very important in the experiments reported here but become unimportant for magnesium particles of, roughly, less than 5  $\mu\text{m}$  diameter. Finally, it should be noted that the estimate at its best can give only an order of magnitude accuracy.

In the end, we would like to comment on an unusual particle behavior noted in Fig. 2.16c. This kind of particle motion, seemingly “against the flow” was observed in several combustion tests. One explanation could be a formation of vortices in the flame zone. Another possibility could be formation of Stefan flows [31] between the pre-heat and combustion zones. In the pre-heat zone additional quantities of gas were produced due to magnesium evaporation, whereas in the combustion zone both oxygen molecules and magnesium atoms were consumed from the gas forming condensed MgO. Therefore, it is possible that local flow from the pre-heat to combustion zone could have affected the motion of the particles. Numerical modeling is needed to investigate the importance of these processes.

## 2.5. SUMMARY

Magnesium particles in the 150-220  $\mu\text{m}$  size range were aerosolized and ignited in microgravity allowing simultaneous observation of the flame evolution and individual particle behavior. The constant pressure flame structure was observed using high-speed movie and video-cameras. The magnesium aerosol flame was observed to consist of pre-heat and combustion zones whose radiation differed in both intensity and spectrum. The observed flame structure is typical of "volatile" aerosol flames, but is not usually anticipated for a coarse metal particle aerosol. The velocity of propagation of the pre-heat zone into the unburnt mixture was found to be in the range of 0.15-0.30 m/s, consistent with the microgravity flame speed measurements reported in the literature. The combustion zone that was visually separated from the pre-heat zone for magnesium aerosol flame for the first time, propagated significantly slower than the pre-heat zone, at a rate of less than 0.1 m/s. It was observed that the width of the pre-heat zone increased and the width of the combustion zone decreased during the flame propagation. It was also observed that the rates of propagation of both the pre-heat and combustion zones oscillated with periods of several tens of milliseconds.

Secondary ignitions were observed consistently in the microgravity experiments several hundred milliseconds after the extinguishment of the original flames. In the secondary ignition, multiple single particles were observed to burn and move rapidly in contrast to the original flame in which no single particle flames were observed.

In the original flame, particles could be seen in the unburnt gas and in the pre-heat zone. They were observed to move primarily away from the flame front; however, in several experiments a group of particles in the pre-heat zone moved towards the flame front. No particle motion indicating inter-particle attraction or repulsion was observed.

The discussion of the flame extinguishment and secondary ignition indicates the importance of the inertial lag (depending on particle size and gas temperature) between the particles and the expanding gas in the development of an aerosol flame. The phenomena caused by this lag may be generic for many burning aerosols and need further investigation.

## 2.6. REFERENCES

1. Annamalai, K., and Ryan, W., "Interactive Processes in Gasification and Combustion. Part I: Liquid Drop Arrays and Clouds" *Prog. Ener. Combust., Sci.* **18**:221-295 (1992).
2. Mikami, M., Kato, H., Sato, J., and Kono, M., "Interactive Combustion of Two Droplets in Microgravity," Twenty-Fifth Symposium (International) on Combustion. The Combustion Institute, Pittsburgh, 1994, pp. 431-438.
3. Kono, M., "Japan's Research on Droplet and Droplet Array Combustion," Third International Microgravity Combustion Workshop, NASA CP 10174, pp. 83-88 (1995).
4. Itoh, A. and Kurosaki, Y., "Downward Flame Spread Along Several Vertical Parallel Sheets of Paper," *Combust. Flame* **60**:269-277 (1985).

5. Tamanini, F. and Moussa, A.N., "Experiments on Turbulent Burning of Vertical Parallel Walls," *Combust. Sci. Tech.* 23:143-151 (1980).
6. Urban, D.L., "Interactions Between Flames on Parallel Solid Surfaces," Third International Microgravity Combustion Workshop, NASA CP 10174, pp. 233-238 (1995).
7. Eckhoff R.K., Dust Explosions in Process Industries, Butterworth-Heinemann, 1991.
8. Leushke, G., "Beitrage zur Erforschung des Mechanismus der Flammenausbreitung in Staubwolken," *Staub* 25, pp.180-186 (1965).
9. Friedman, R., and Macek, A. "Ignition and Combustion of Aluminum in Hot Ambient Gases," *Combust. Flame*, 6:9-19 (1962).
10. Drew, C.M., Gordon, A.S., Knipe, R.H., Kraeutle, K.J., Prentice J.L., and Price, E.W. Metal Particle Combustion Progress Report. Naval Weapons Center, China Lake, CA, *NWC TP 4435* (1968).
11. Prentice, J.L., "Combustion of Pulse-Heated Single Particles of Aluminum and Beryllium" *Combust. Sci. Tech.*, 1: 358-398 (1970).
12. Nelson, L.S., Rosner, D.E., Kurzius, S.C., and Levine, H.S., "Combustion of Zirconium Droplets in Oxygen/rare Gas Mixtures-kinetics and Mechanism". Twelfth Symposium (International) on Combustion, The Combustion Institute, Pittsburgh, 1968, pp. 59-70.
13. Dreizin, E.L., Suslov, A.V., and Trunov, M.A., "General Trends in Metal Particle Heterogeneous Combustion" *Combust. Sci. Tech.*, 90:79-99 (1993).
14. Florko, A.V. and Golovko, V.V., "Characteristics of the Radiation Emitted by and the Conditions for Nucleation of Submicron Oxide Particles During Combustion of Magnesium" *Fizika Goreniya i Vzryva* 29:17-22 (1992) (in Russian).
15. Dreizin, E.L., Molodetsky I.E., and Law C.K., "Internal and Surface Phenomena in Metal Combustion," Third International Microgravity Combustion Workshop, Cleveland, OH, NASA CP 10174, pp. 129-134 (1995).
16. Florko, A.V., Kozitskii, S.V., Zolotko, A.N., and Golovko, V.V., "Mechanism of Transport of Condensed Combustion Products to the Surface of a Burning Magnesium Particle," *Fizika Goreniya i Vzryva* 19:24-29 (1983) (in Russian).
17. Golovko, V.V., Kozitskii, S.V., and Florko, A.V., "Electric Field of a Single Burning Magnesium Particle," *Fizika Goreniya i Vzryva* 2:27-32 (1984) (in Russian)
18. Valov, A.E., Kustov, Y.A., and Shevtsov, V.I., "Spectroscopic Study of the Combustion of Solitary Magnesium Particle in Air and in Carbon Dioxide", *Combustion, Explosion, and Shock Waves*, 30:431-436 (1994).
19. Baron, P.A. and Willeke, K., "Gas and Particle Motion" in *Aerosol Measurements: Principles, Techniques, and Applications* (Willeke, K., and Baron, P.A., Eds.) Van Nostrand Reinhold, NY, 1993
20. Shevchuk, V.G., Goroshin, S.A., Klyachko, L.A., Ageyev, N.D., Kondratyev, E.N., and Zolotko, A.N., "Speed of Flame Propagation in Magnesium Particle Aerosols," *Fizika Goreniya i Vzryva* No 1, pp. 57-63 (1980) (in Russian).
21. Lan, Y., and Rosato, A.D., "Macroscopic Behavior of Vibrating Beds of Smooth Inelastic Spheres," *Phys. Fluids*, 7(8):1818-1831 (1995).
22. Ballal, D.R., "Flame Propagation Through Dust Clouds of Carbon, Coal, Aluminum, and Magnesium in an Environment of Zero Gravity," *Proc. R. Soc. Lond. A* 385, pp. 21-51

- (1983).
23. Brzustowski, T.A., and Glassman, I. In *Heterogeneous Combustion* (H.G. Wolfhard, I. Glassman, and L. Green, Eds), Academic Press, NY, 1964, pp. 117-158
  24. Sullivan, H. F., and Glassman, I., "Vapor-Phase Diffusion Flames in the Combustion of Magnesium, Calcium and Strontium" *Combustion Science and Technology*, 4:241-256 (1972)
  25. Dreizin, E.L. "Experimental Study of Aluminum Particle Flame Evolution in Normal And Micro-gravity", *Comb. Flame*, (1998) in press
  26. Cassel, H.M., "Some Fundamental Aspects of Dust Flames", *US Bureau of Mines Report of Investigations 6551*, Bureau of Mines, Washington, 1964.
  27. Florko, A.V., Golovko, V.V., Ohrimenko, N.A., and Shevchuk, V.G., "Structure of the Magnesium Particle Combustion Zone. 1. Optico-Spectrum Investigations. *Fizika Gorenia I Vzryva*, Vol. 27, No 1, pp. 37-42 (1991) (In Russian)
  28. Law, C.K., and Williams, F.A., "Combustion of Magnesium Particles in Oxygen-Inert Atmospheres" *Comb. Flame* 22:383-405 (1974)
  29. Goroshin, S.V., Shevchuk, V.G., and Ageyev, N.D., "Oscillatory Combustion of Aerosols", *Fizika Gorenia I Vzryva*, No 6, pp. 15-21 (1981) (In Russian)
  30. Berlad, A.L., Ross, H., Facca, L., and Tangirala, V., "Particle Cloud Flames in Acoustic Fields", *Comb. Flame* 82:448-450 (1990)
  31. Fuchs, N.A., *Evaporation and Droplet Growth in Gaseous Media*, Pergamon Press, London, 1959

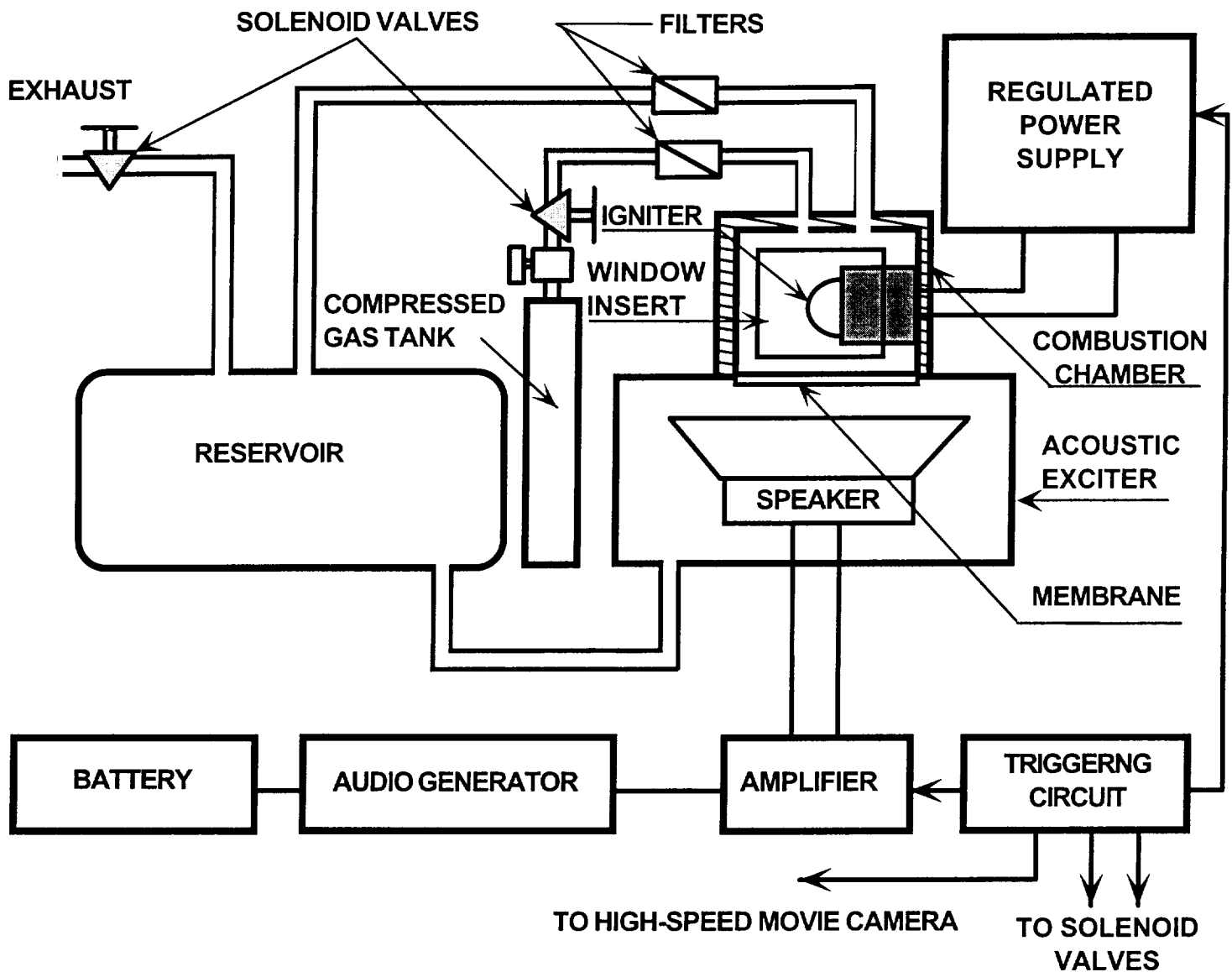


Fig. 2.1. Simplified schematic of the experimental rig used for the drop-tower tests

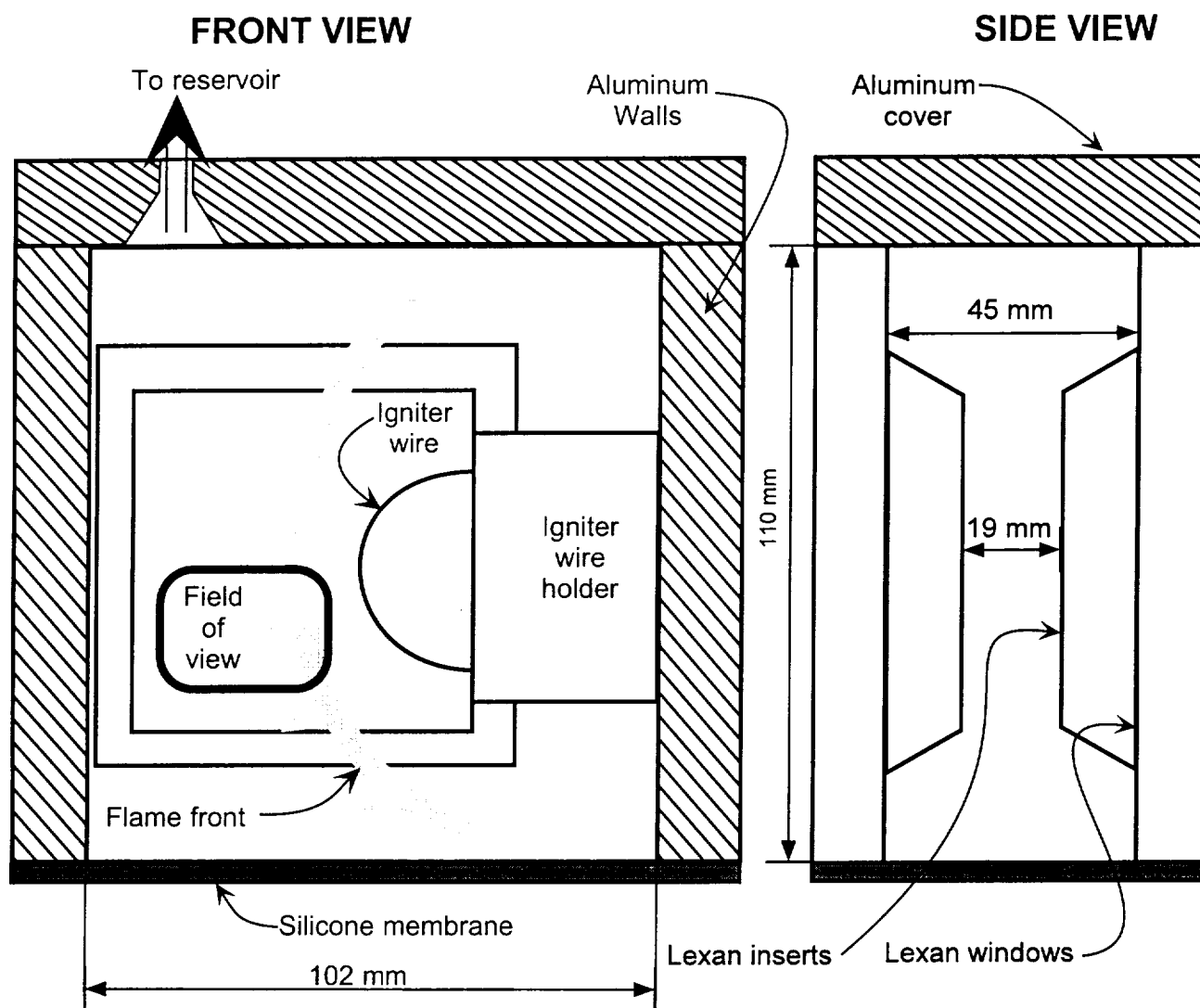


Fig. 2.2. Sketch (drawn to scale) of the chamber in which aerosol was created and burned



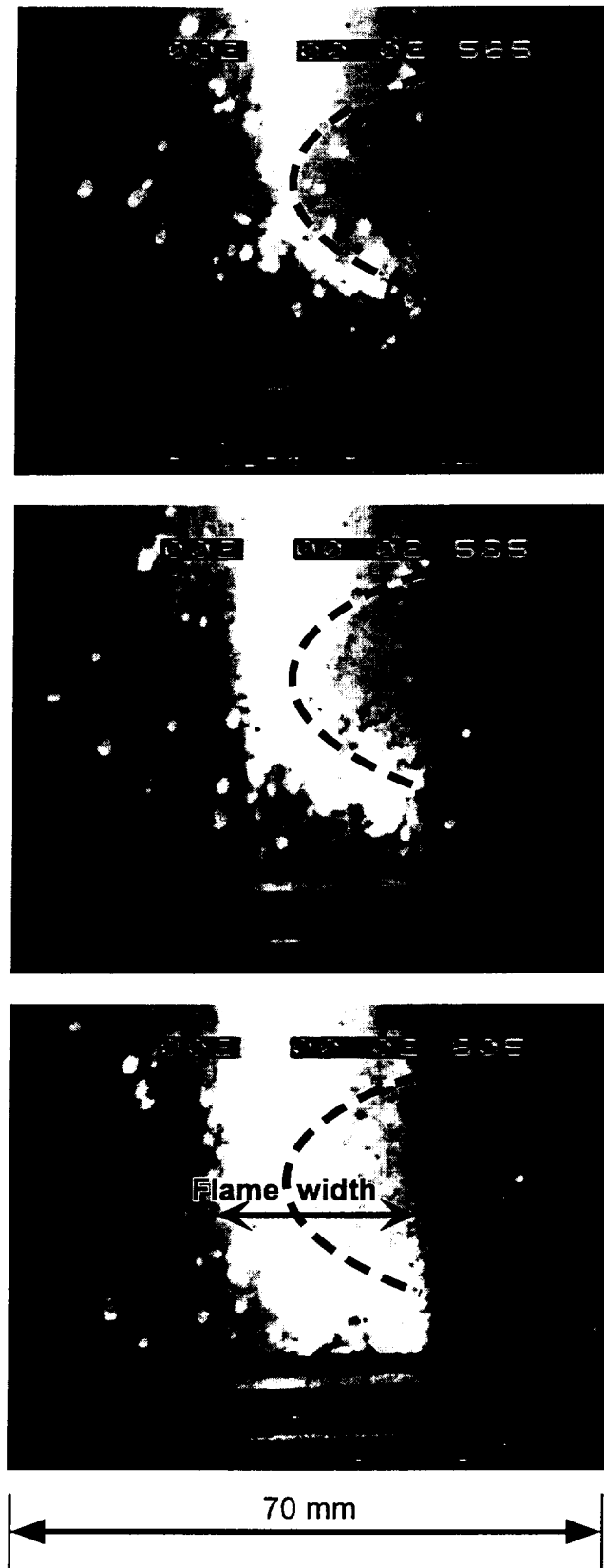


Fig. 2.3. Sequence of 20 ms apart high-speed video frames illustrating magnesium aerosol flame development in normal gravity. Igniter wire is shown by a dashed line.

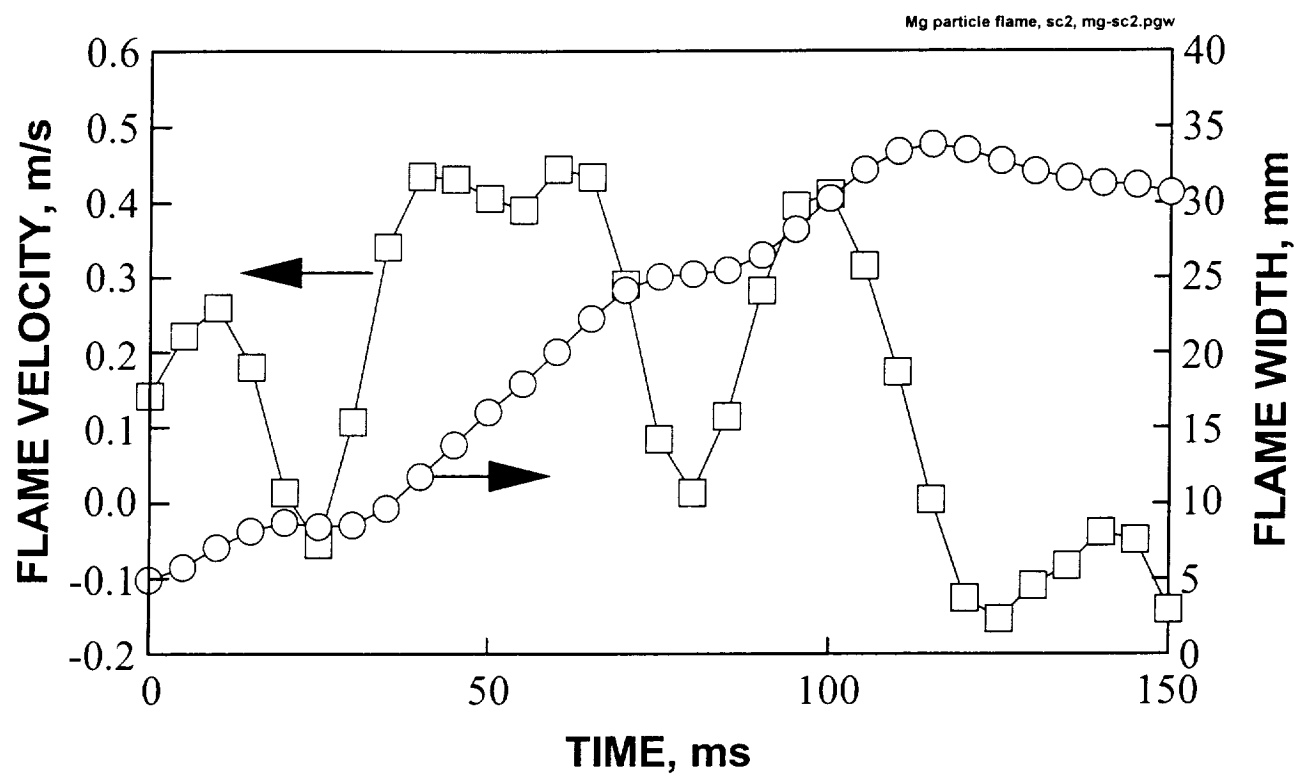


Fig. 2.4. Temporal variations of the width and velocity of expansion of magnesium aerosol normal gravity flame

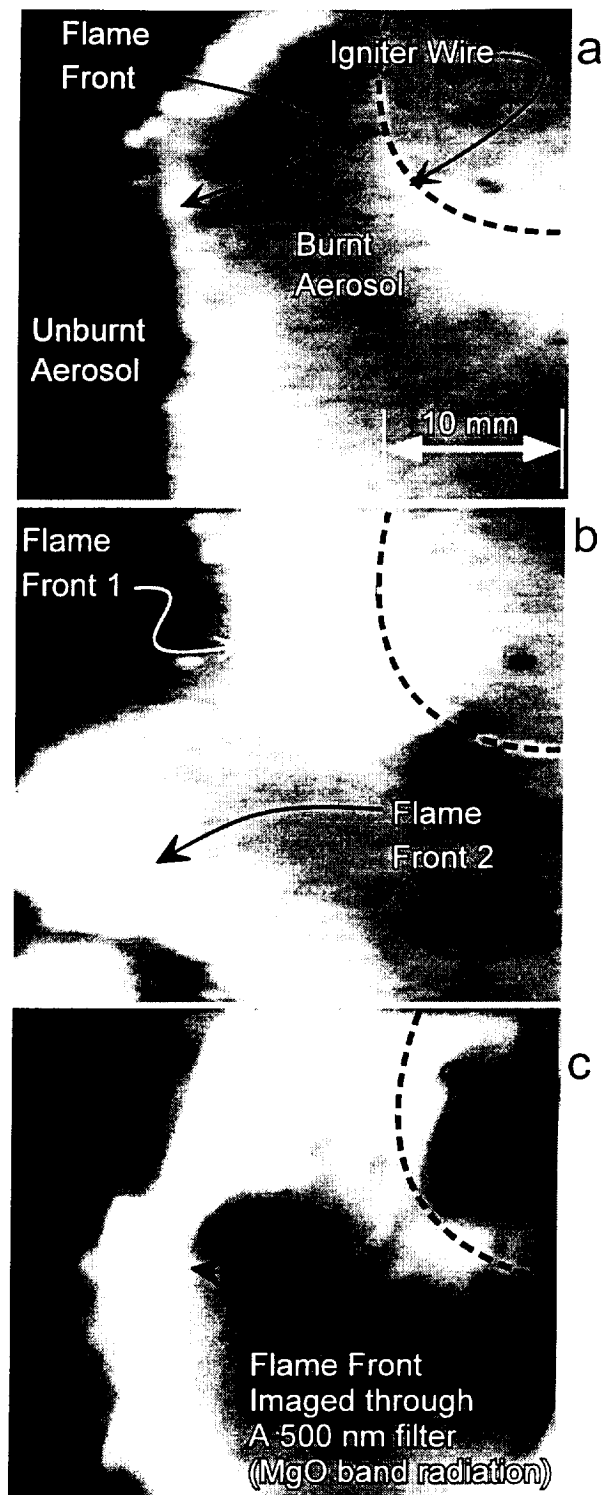


Fig. 2.5. Video frames illustrating magnesium aerosol flame development in microgravity:

- a. Continuous flame front
- b. Multiple flame fronts
- c. Continuous flame front imaged through a 500 nm filter

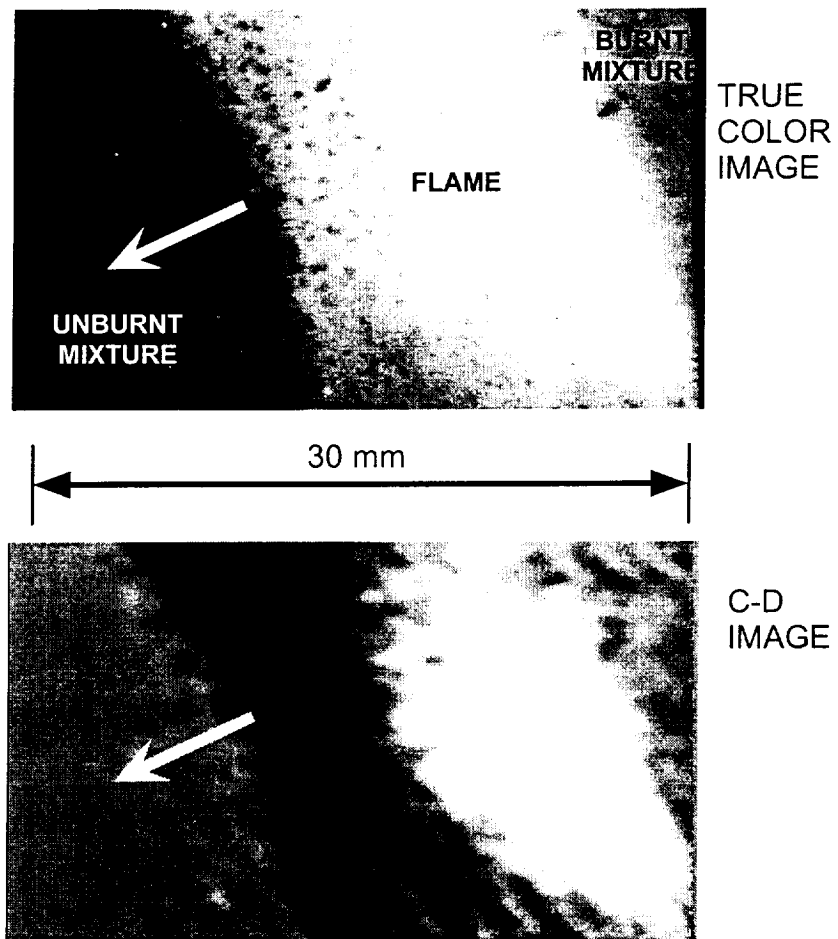


Fig. 2.6. True color video-frame and corresponding C-D image showing separation of pre-heat and combustion zones. White arrows show the direction of the flame propagation.

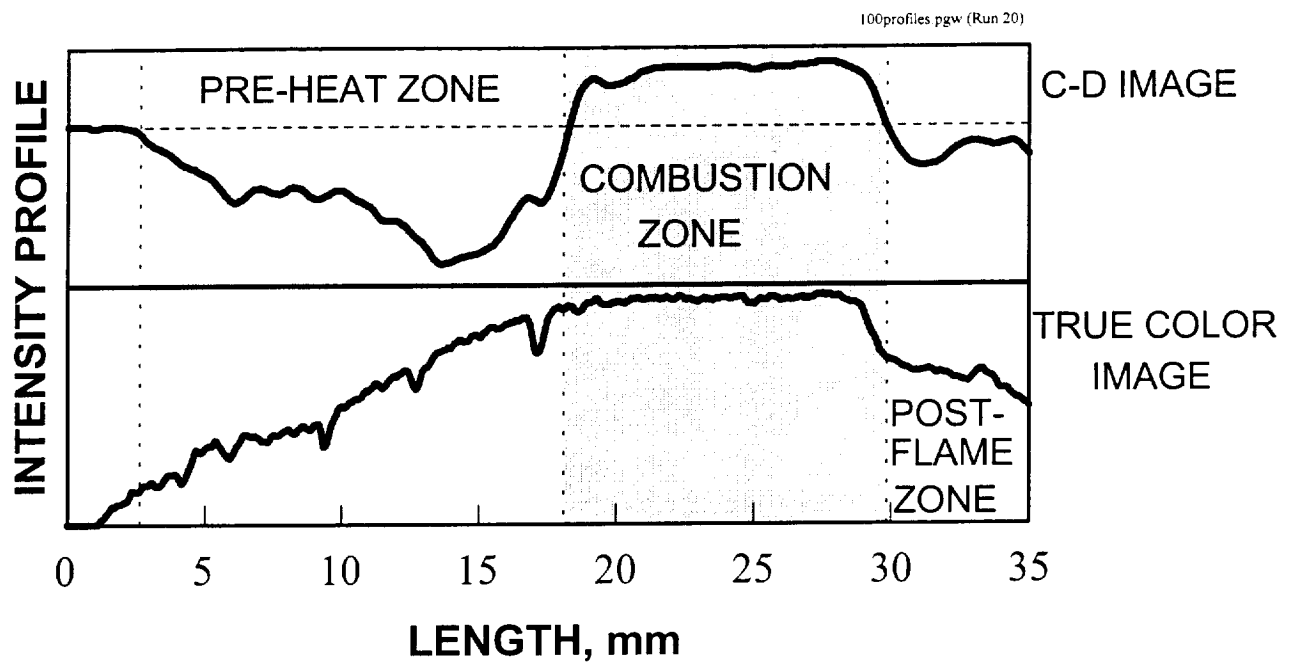


Fig. 2.7. Intensity profiles for the C-D and true color images presented in Fig. 2.6

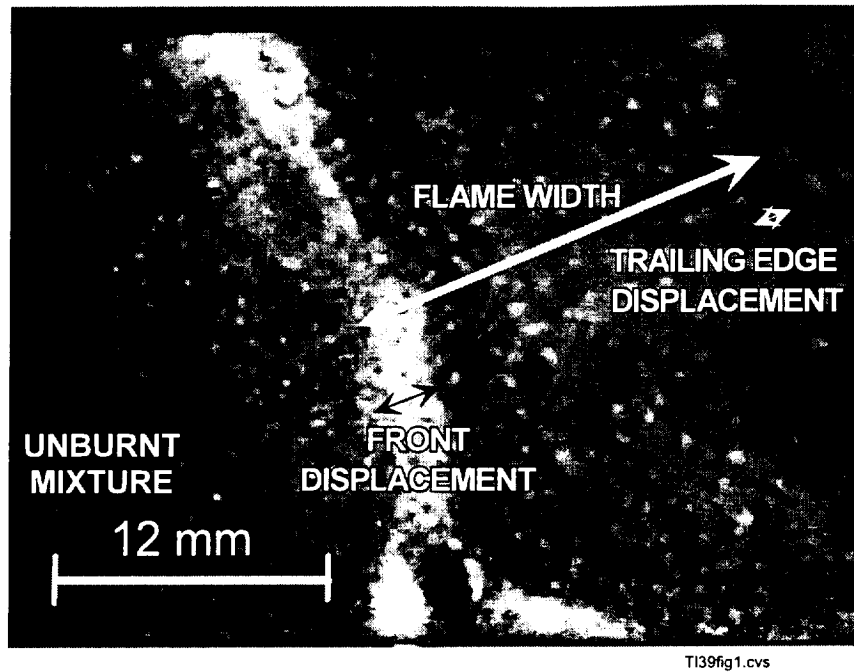


Fig. 2.8. An artificial T-D image produced as a difference between two sequential high-speed movie frames

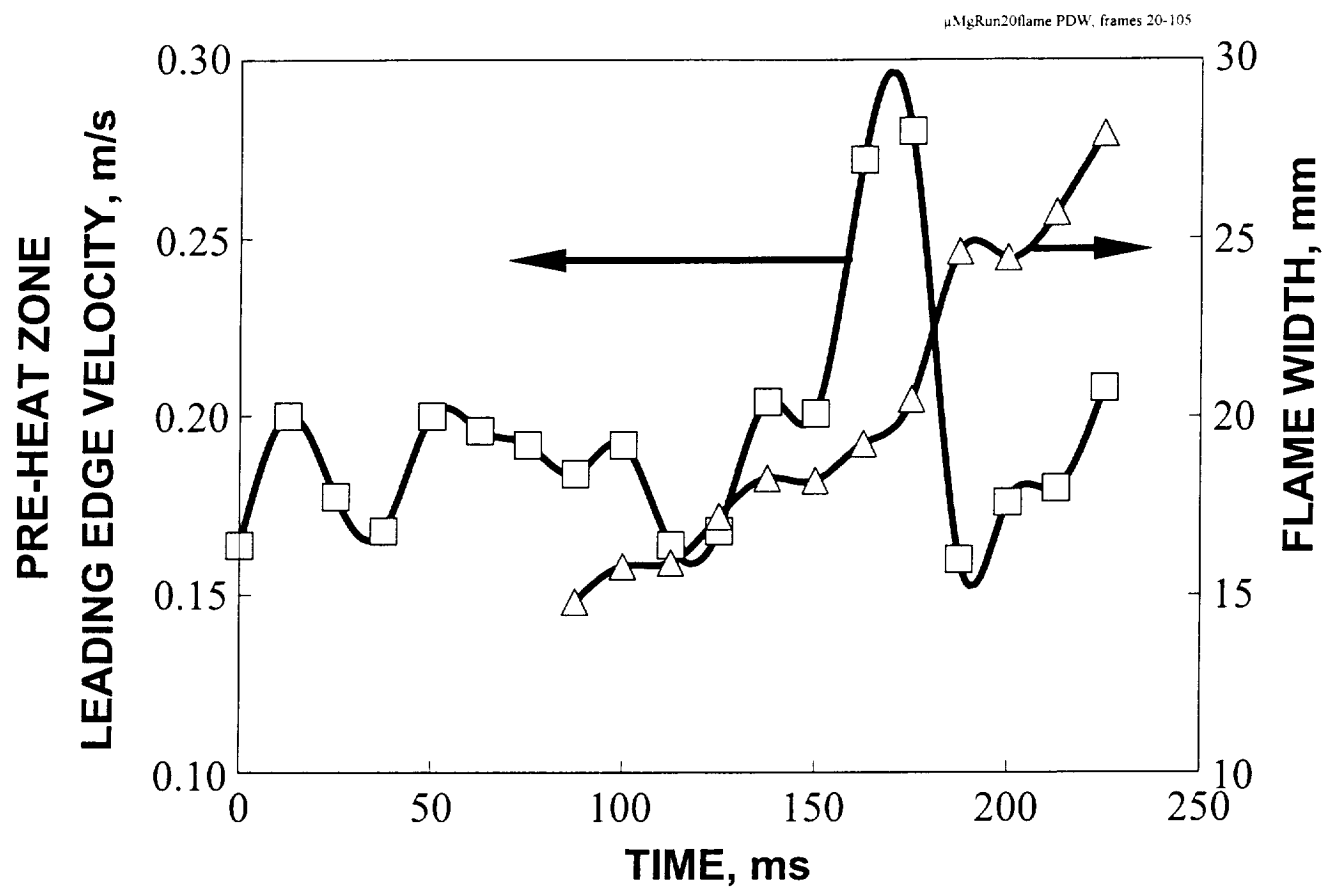


Fig. 2.9. Temporal variations of the propagation velocity of the leading edge of the pre-heat zone and the flame width inferred from the recorded high-speed movie. The time "0" corresponds to the moment the flame entered the camera field of view

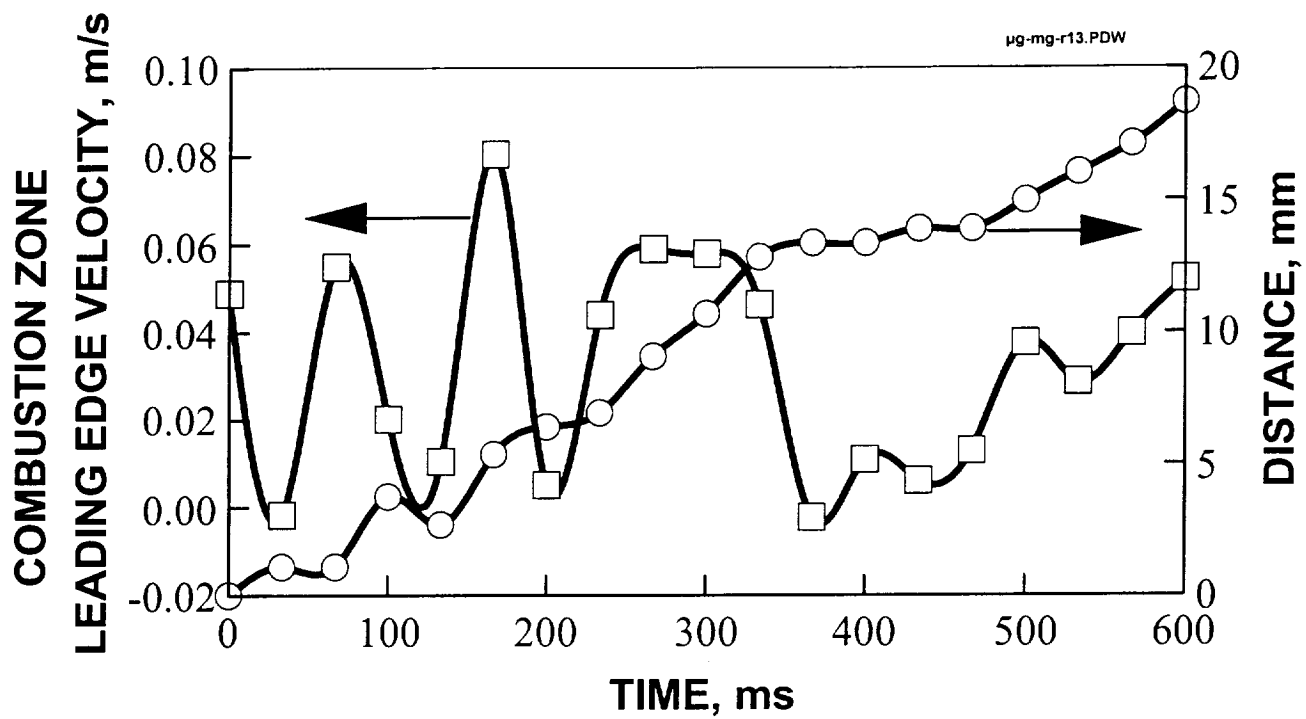


Fig. 2.10. Temporal variations of the propagation velocity of the leading edge of the combustion zone and distance this edge traveled inferred from the recorded high-speed movie  
The time "0" corresponds to the moment flame entered the camera field of view



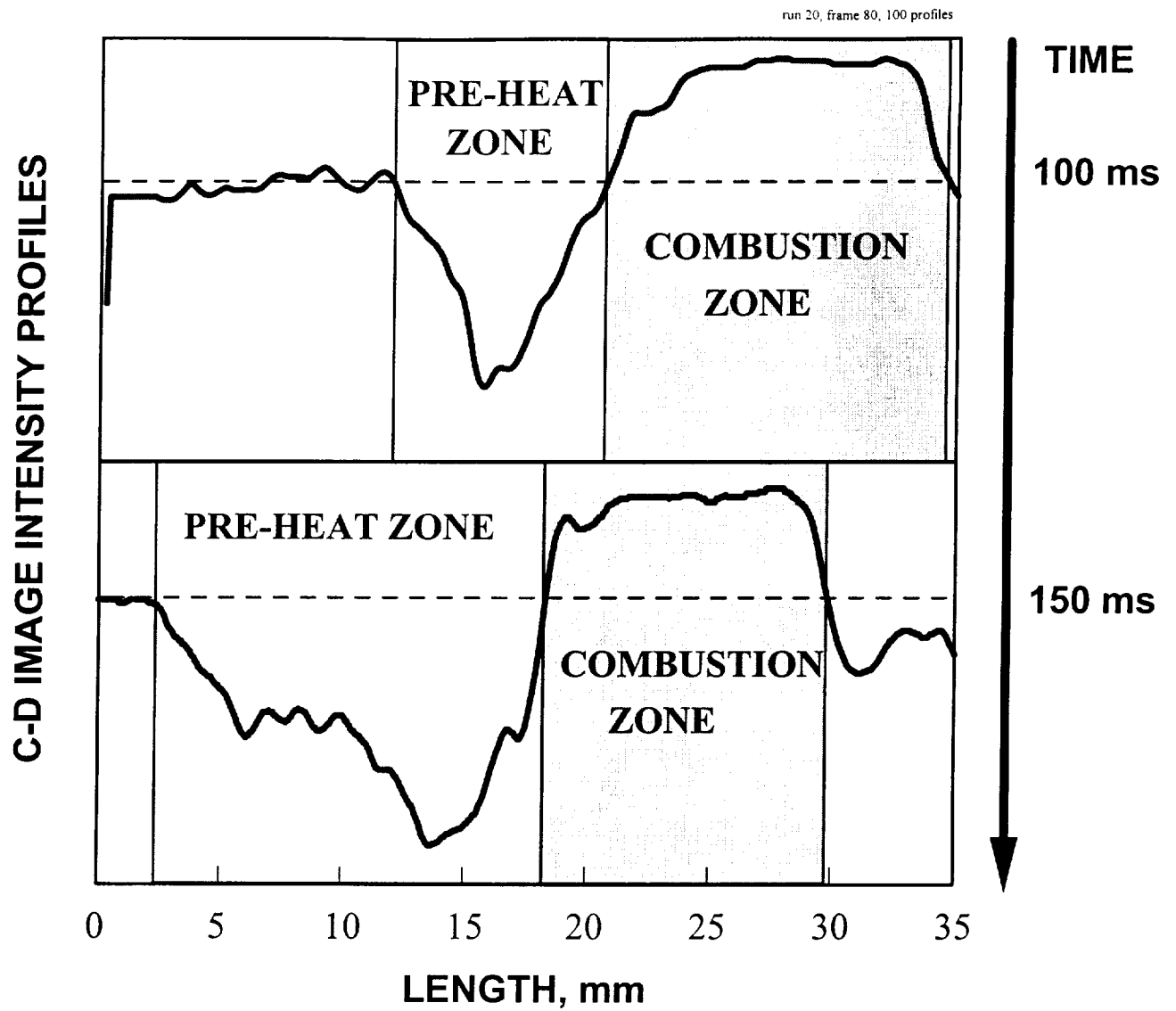


Fig. 2.11. Intensity profiles measured for two C-D images visualizing the structure of a magnesium aerosol microgravity flame at different moments

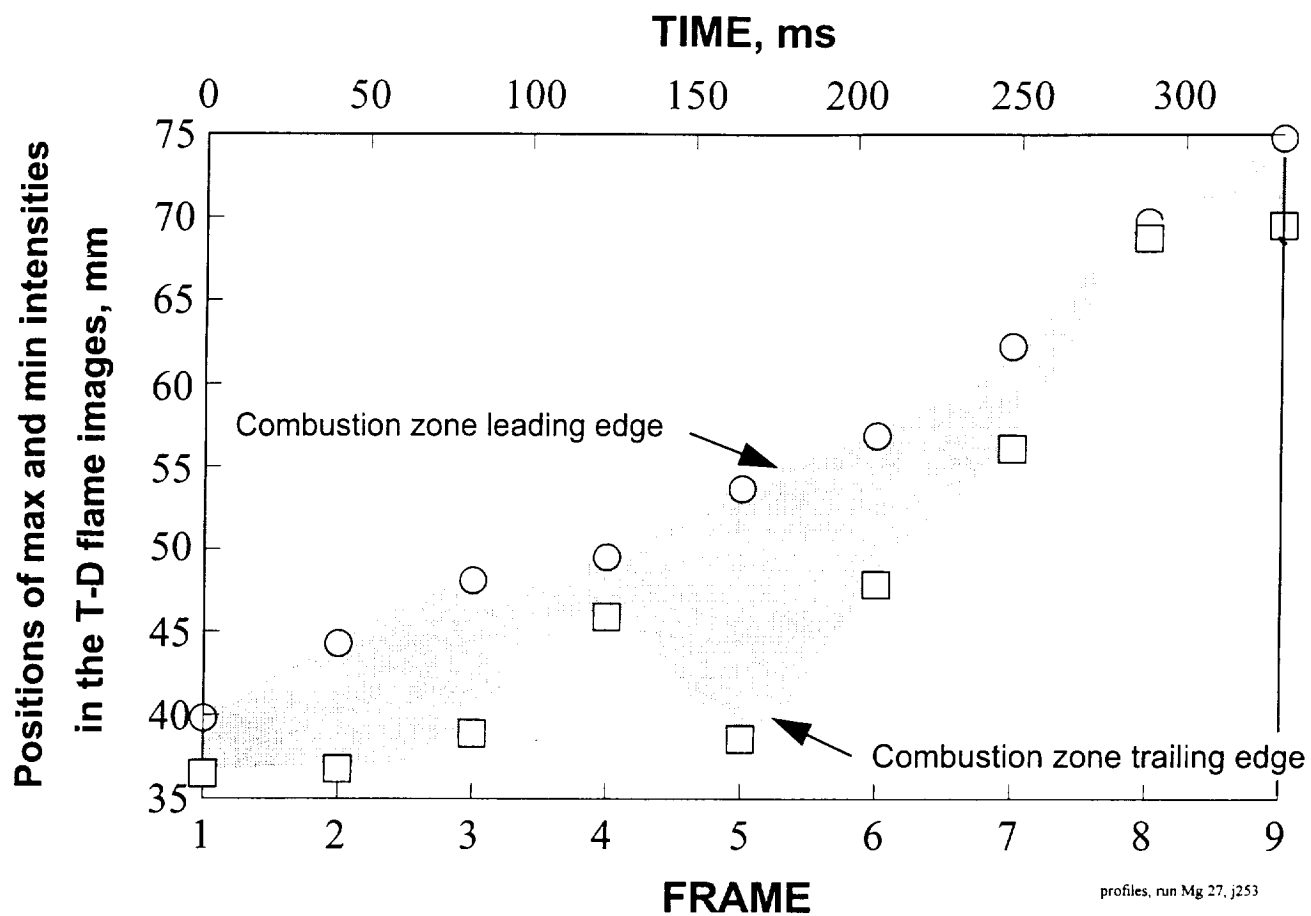


Fig. 2.12. Sequential positions of the leading and trailing edges of the combustion zone in the magnesium aerosol microgravity flame determined using regular speed video-record

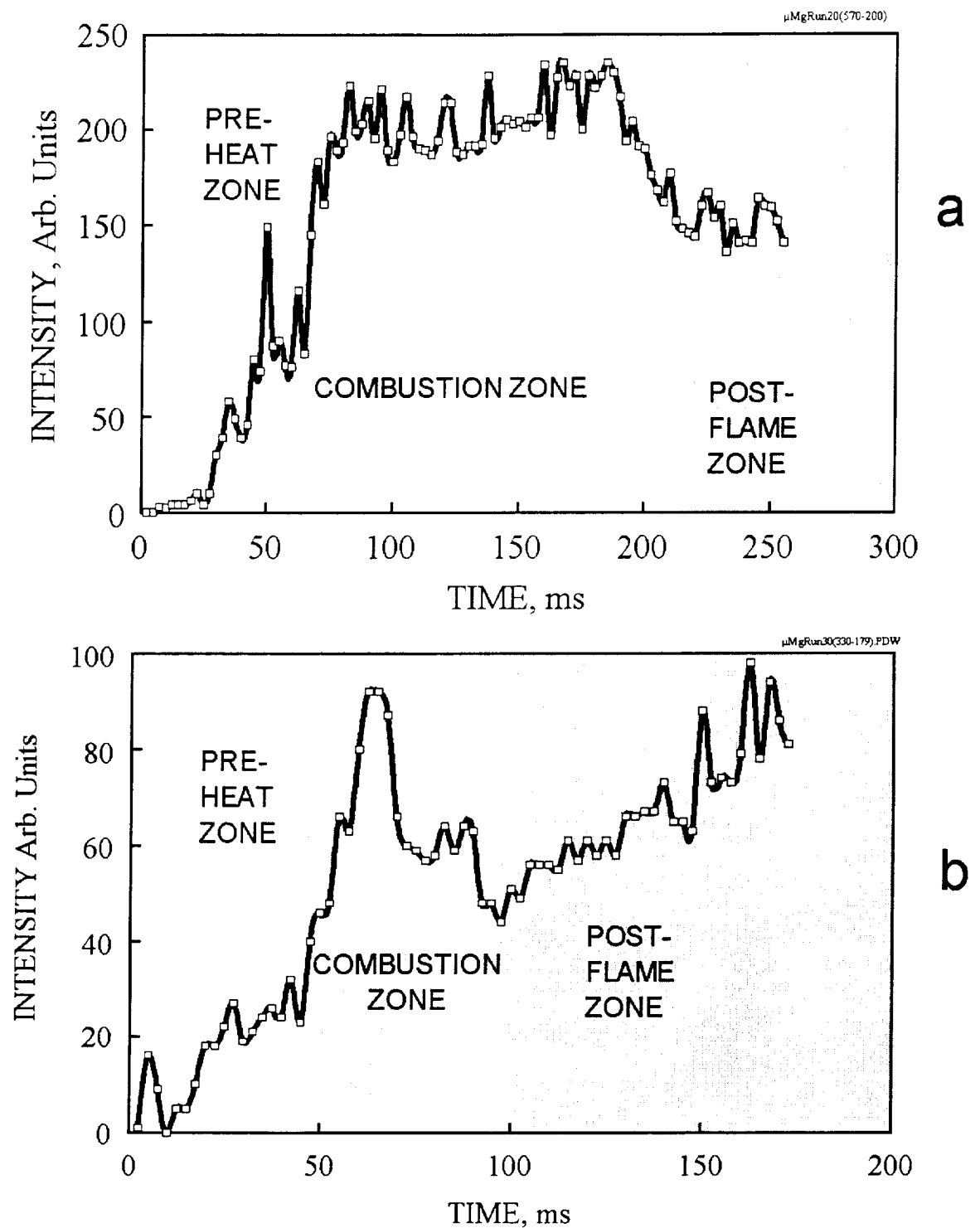


Fig. 2.13. Intensity of radiation measured at a chosen location during flame propagation in microgravity.

a. Run 20: 1.1 g of 180-250  $\mu\text{m}$  Mg powder in air

b. Run 30: 1.1 g of 150-180  $\mu\text{m}$  Mg powder in air

**DIRECTION OF FLAME PROPAGATION** ←

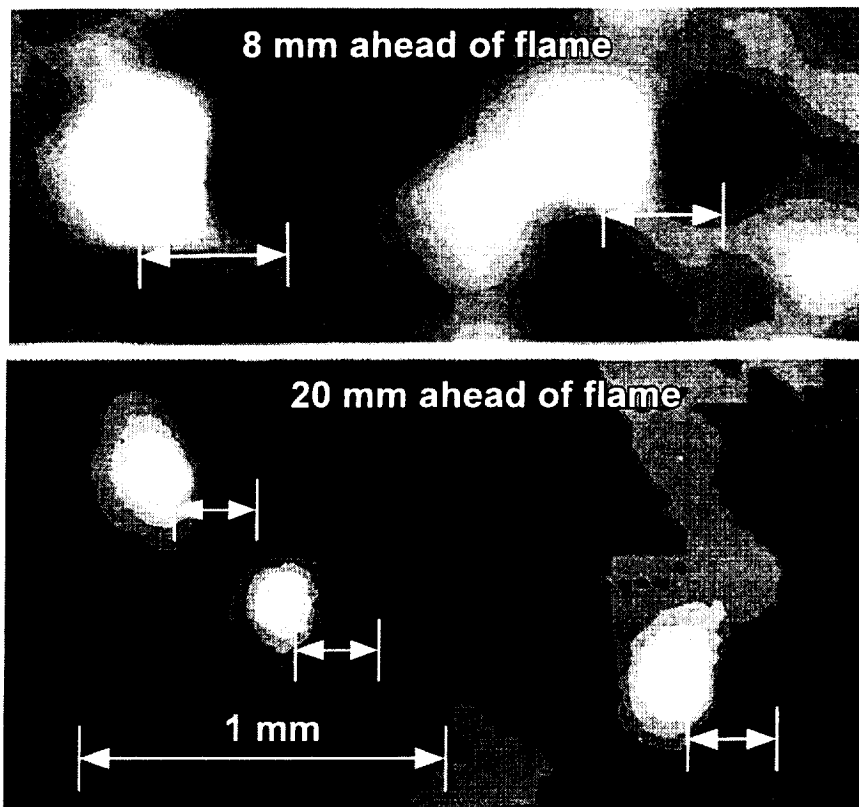


Fig. 2.14. Magnified portions of a T-D video-frame showing displacements of individual magnesium particles at different distances from the flame front. The distances between the centers of dark and bright regions show the displacement of particles for a period of 2.5 ms.

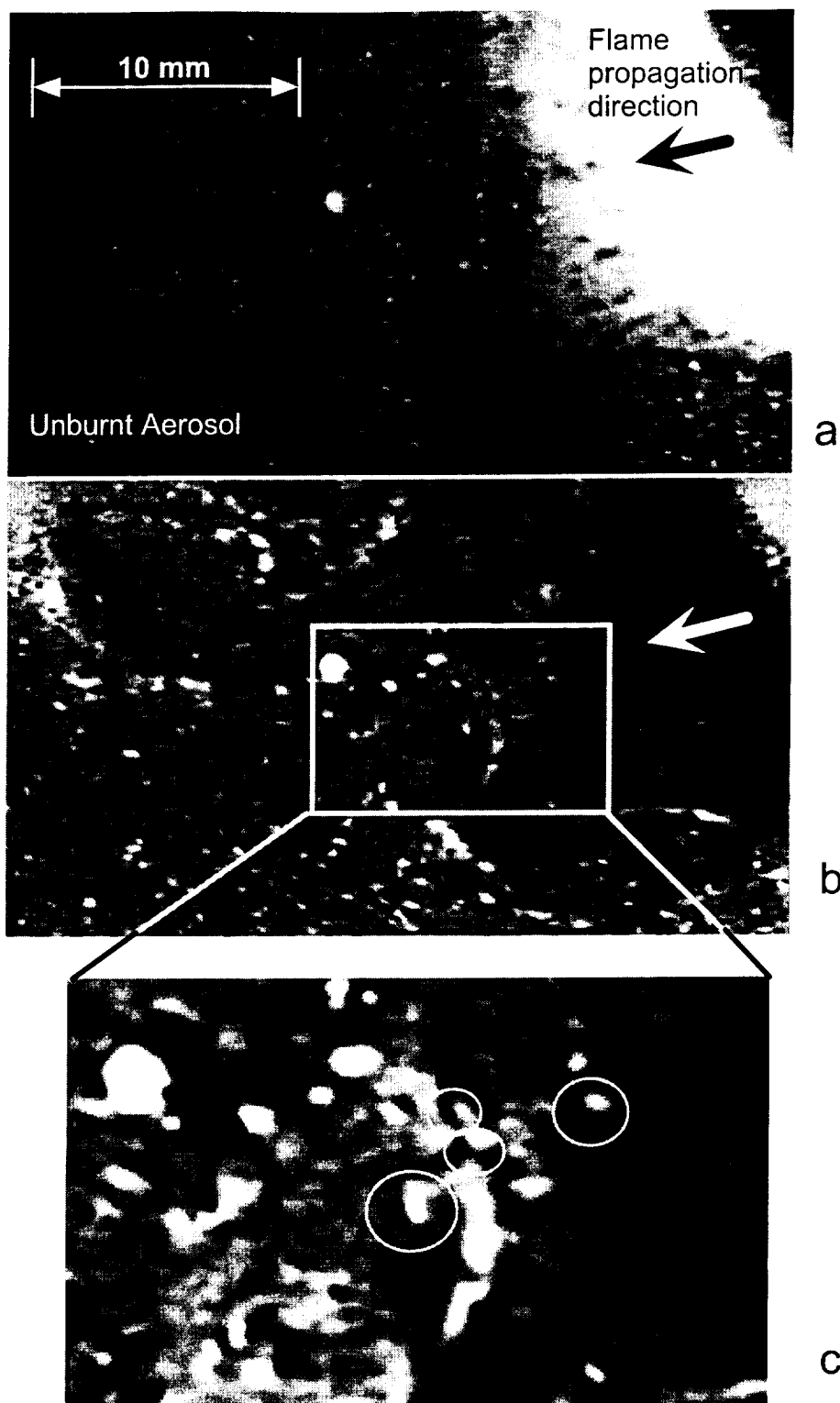


Fig. 2.16. True color (a) and artificial T-D image (b) of a flame front in aerosol of magnesium particles burning in microgravity. A magnified portion of the T-D image is also shown (c).

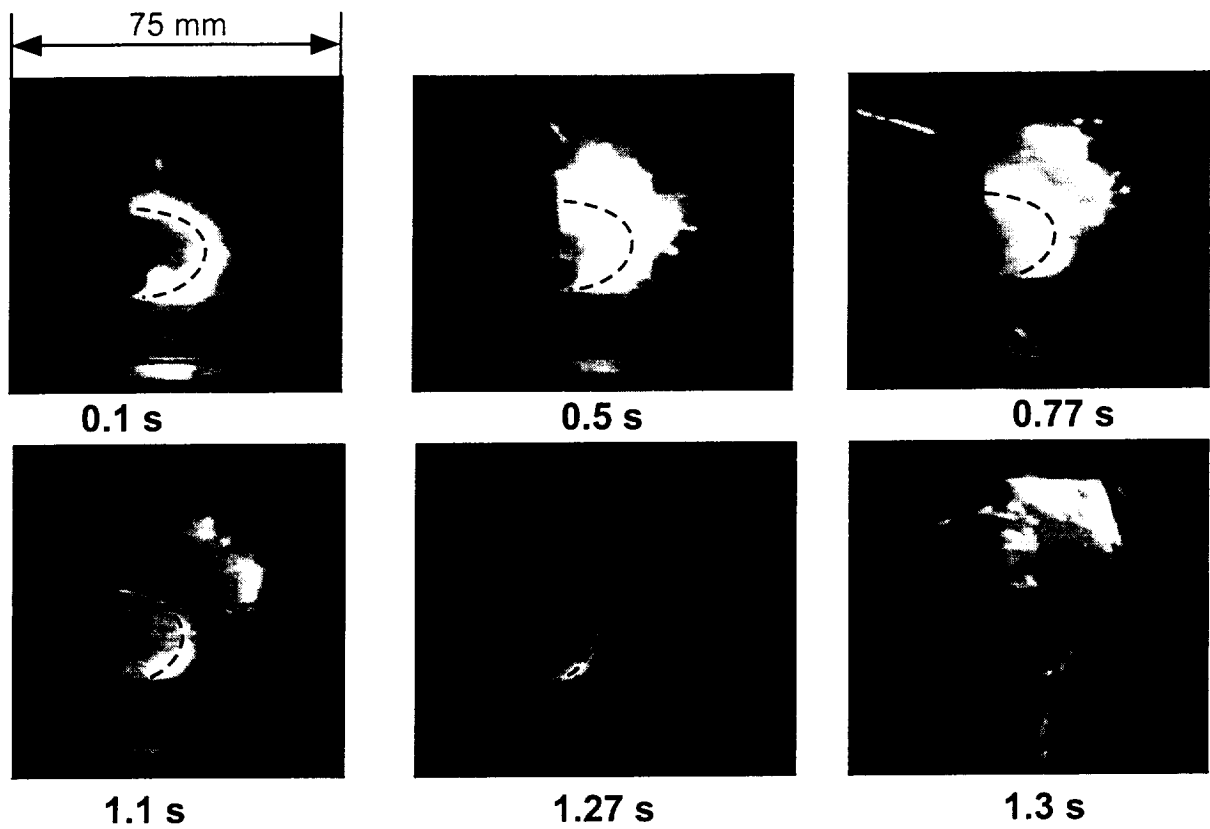


Fig. 2.17. A sequence of video-frames showing development and extinction of the original flame front, and subsequent re-ignition. Dashed lines show igniter wire location.

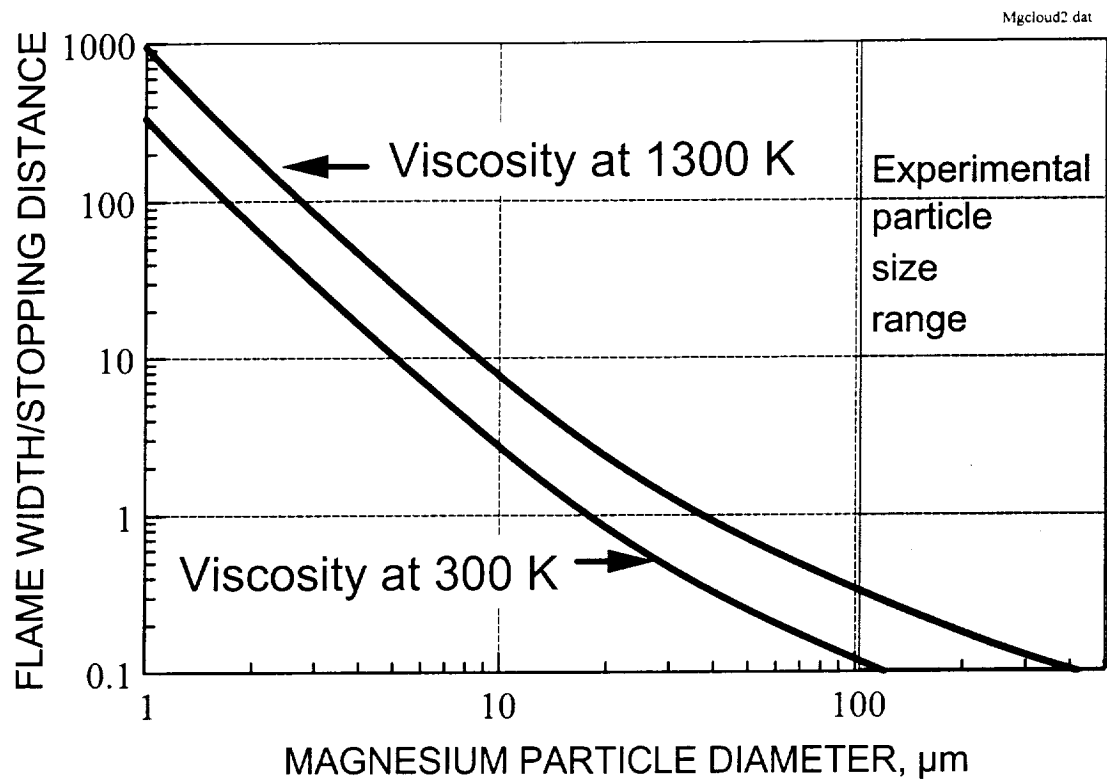


Fig. 2.18. Estimated ratio of the flame width to particle stopping distance for different size magnesium particles. Flame with estimated using [22]

### 3. FURTHER EXPERIMENTS ON MAGNESIUM AEROSOL COMBUSTION IN MICROGRAVITY

Reference: Combustion and Flame, 1999, submitted

#### ABSTRACT

An experimental study of the combustion of an aerosol of coarse magnesium particles in microgravity is reported. 180-250  $\mu\text{m}$  particles were aerosolized in a 0.5 L combustion chamber and ignited in a constant pressure, microgravity environment. Two flame images were produced simultaneously using interference filters separating adjacent MgO and black body radiation bands at 500 and 510 nm, respectively. The characteristic MgO radiation was used as an indicator of the gas-phase combustion. Comparison of the two filtered flame images showed that pre-heat and combustion zones can be distinguished in the flame. Experiments have also shown that in microgravity the flame speed depends on the initial particle speeds varied in the range of 0.02-0.4 m/s. This dependence is, most likely, due to the role the moving particles play in the heat transfer processes. Product analyses showed an oxide coating on the surfaces of particles collected after experiments in which the flame speeds were higher than 0.1 m/s. No oxide coating was detected in the products collected after experiments in which a slower flame propagation was observed. However, the particles collected after such experiments contained significant amounts of dissolved oxygen. Based on the observed in all the experiments, including those with the very slowly propagating flames, strong MgO radiation and production of dense MgO smoke clouds, it has been suggested that the MgO produced in the vapor phase flame is not the primary source of the MgO coating found on the burnt particle surfaces. An alternative mechanism of forming the oxide coating is, consistent with the earlier single metal particle combustion studies, via the formation of a metal-oxygen solution followed by a phase separation occurring within the burning particles.



### 3.1. INTRODUCTION

Mechanisms of combustion and flame propagation in two-phase systems and, in particular, in metal aerosols are of considerable interest because of numerous practical implications for propulsion, explosives, pyrotechnics, incendiaries, flame synthesis, and fire suppression techniques. Combustion of single particles of condensed fuels, e.g., hydrocarbons, coals, plastics, and metal particles has been extensively studied and modeling of the two-phase combustion system is usually based upon the single particle combustion mechanisms. However, some intriguing questions about combustion in the two-phase systems remain:

1. Do particle-particle and particle assembly-flame interactions affect and alter the single particle combustion processes in aerosol flames?
2. What are the specific particle-particle and particle-flame interaction effects that are significant in combustion of a two-phase system?

The microgravity environment can be exploited to experimentally address these questions. Specifically, a two-phase system using particles large enough to be observable, can be produced and ignited. In normal gravity, large particles would quickly fall down and the lifetime of such a two-phase system would have been very short. However, in microgravity, flame propagation through such an unusual two-phase system can be established, and the single particle combustion and the bulk two-phase system combustion mechanisms can be correlated with each other using experimental observations. The combustion can be analyzed adopting techniques developed for single particle combustion studies. With this approach in mind, an experimental apparatus has been designed and built and microgravity experiments have been conducted with aerosolized coarse metal powders burning at constant pressure [1-3]. Magnesium was used in the first experiments because Mg single particle combustion has been extensively studied and because Mg particles ignite readily, making the microgravity experiments simpler and more reliable.

For an aerosol of coarse magnesium particles, particle motion due to drag forces was found to change particle number density (and, thus, local equivalence ratio) in the unburnt aerosol during the constant pressure flame propagation experiments [2]. Interestingly, a similar observation has been reported for microgravity combustion of aerosolized iron particles [4]. Two luminous zones could be distinguished in the Mg aerosol flame propagating in microgravity based on the radiation spectra and intensity profiles [2]. Red color dominated in the radiation of a luminous flame zone adjacent to the unburnt aerosol and green color dominated in a more bright zone adjacent to the burnt aerosol. Because the peak of the characteristic MgO radiation lies in the green part of the spectrum, it has been suggested in Ref. 2 that the two zones can be identified as the pre-heat and combustion zones.

This paper presents further experimental results characterizing combustion of magnesium aerosol in microgravity. In addition to optical diagnostics, combustion products collected after microgravity experiments have been analyzed. Results of this work are compared with the recently reported experiments on single Mg particle combustion [5] that have indicated that oxygen dissolution and phase changes occurring in burning particle affect single particle combustion

scenario and product composition and morphology.

### 3.2. EXPERIMENTAL

A detailed description of the experimental apparatus is given elsewhere [2]. The 0.5 liter combustion chamber is rectangular in shape with a narrow, 19 mm wide central section through which the flame propagates. The chamber has transparent walls made of Lexan and elastic silicone rubber floor that oscillates to aerosolize particles before ignition. The flame structure and details of individual particle combustion are visualized using both high speed movie and regular speed video cameras. The microgravity experiments are conducted using the 2.2 s NASA Glenn Research Center drop tower.

Similar mass loads of 1.1 g of magnesium particles (Aldrich Chemical) with sizes between 180 and 250  $\mu\text{m}$  were used in all of the magnesium combustion experiments described in this paper. An optical setup including two mirrors tilted slightly relative to each other and two interference filters with the wavelengths of 500 and 510 nm (half bandwidth of 8 nm for each filter) separating the MgO [6] and black body radiations respectively, was used to produce simultaneously two filtered images of the flame on each video-frame. Because the filter wavelengths were very close to each other, the color sensitivity of the video camera is nearly the same for both of the filtered flame images. That made it possible to directly compare the radiation profiles measured at the MgO characteristic wavelength with those of the black body radiation. The MgO radiation intensity determined from these measurements was used as an indicator of the gas phase reaction.

Each test included aerosolizing metal particles under microgravity using oscillations of the chamber floor, a time delay required to produce a steady aerosol, and igniting such an "aerosol" at constant pressure using a hot wire igniter. The delay between the time when the chamber floor membrane stopped oscillating and when the aerosol was ignited, varied from 0.1 to 1.2 s to investigate the effect of the residual particle velocity on the flame propagation. Combustion products were collected and analyzed after the experiments. Samples of the combustion products were embedded into epoxy and cross-sectioned for the internal phase analyses. A Philips XL30 Field Emission Scanning Electron Microscope (SEM), a Cameca SX50 x-ray Electron Probe Microanalyzer (EPMA) and a Siemens D500 x-ray Diffractometer (XRD) using Cu  $K\alpha_1$  radiation were used for analyses of the collected post-experiment powders.

The high speed movies recorded during the experiments were transferred to SVHS video format. Both high-speed (transferred) and regular speed videos were digitized and used to characterize flame radiation and determine the flame propagation speed as a function of the ignition delay. NASA Glenn Research Center Tracker software was used to track (utilizing the threshold tracking procedure) the flame front position in time.

### 3.3. RESULTS AND DISCUSSION

#### *Flame speed measurements*

Three typical examples of flame front position versus time plots are shown in Fig. 3.1. For

each such set of data, an average flame speed was determined as a slope of a linear fit and a plot of the average flame speed as a function of the time delay is shown in Fig. 3.2. The error bars shown signify the standard deviations for the slope of the found linear fit. It is interesting that a clear trend to higher flame velocities at the shorter time delays is observed. Because the initial particle speed is the only parameter affected by the time delay, the observed trend indicates that the particle residual speed (that always is comparatively low, on the order of 0.1 m/s) noticeably affects the flame propagation. To better understand the nature of this correlation, the particle speed can be estimated as

$$v=v_0\exp(-t/\tau) \quad (1)$$

where  $v_0$  is the initial particle speed, and  $\tau$  is the relaxation time that can be found as

$$\tau=(\rho d^2 C_c)/(18\eta) \quad (2)$$

where  $\rho$  and  $d$  are the particle density and diameter, respectively,  $\eta$  is gas viscosity ( $\eta = 1.8 \cdot 10^{-5}$  kg/(m·s) for room temperature air), and  $C_c$  is Cunningham slip correction factor [7]. For reference, a velocity history estimated for a 200  $\mu$ m magnesium particle with  $v_0 = 0.5$  m/s (a typical experimental particle residual velocity) is plotted in Fig. 3.2. For such low particle velocities, turbulence effects are virtually non-existent. The rate of particle combustion, however, is slightly affected by the particle motion due to convection effects on the rates of the heat and mass transport processes. Therefore, two-phase flame propagation models that are based on single particle combustion models predict a weak dependence of the burning velocity (and thus, also flame speed) on the particle speed. For example, according to Ballal's model [8], burning velocity

$$S_u \approx D_r/t_c \quad (3)$$

where  $D_r$  is the thickness of the reaction zone, and  $t_c$  is the particle combustion time.

$$t_c=d^2/K, \quad (4)$$

where  $K$  is the evaporation constant depending on the particle velocity (forced convection) according to the Frössling correction [9]:

$$K=(8/\rho)(\lambda/C_p)\ln(1+B)(1+0.276Re^{1/2}Pr^{1/3}) \quad (5)$$

where  $\lambda$  and  $C_p$  are the gas mixture heat conductivity and heat capacity, respectively,  $Re$  and  $Pr$  are the Reynolds and Prandtl numbers, respectively, and  $B$  is the transfer number [9] and is defined as:

$$B=[Q_o Y_{o\infty} + C_p(T_\infty - T_s)]/(\gamma L) \quad (6)$$

where  $Q_o$  is the energy released in combustion per mole of oxygen consumed,  $Y_{o\infty}$  is the oxygen mole fraction in the mixture,  $T_\infty$  and  $T_s$  are the ambient and particle surface temperatures, respectively,  $\gamma$  is the stoichiometric factor, and  $L$  is the specific metal vaporization energy. To provide a simple

estimate, the reaction zone thickness,  $D_r$ , which is a function of the heat conductivity and the temperatures in the pre-heat and combustion zones, can be taken as a constant equal to the optically determined thickness of the combustion zone [1-3]. Substituting it and the equations (4), (5), and (6) into Eq. (3) and computing particle velocities using Eq. (1), the changes in the burning velocity  $S_u$  were estimated for delay times  $t$  in the range of 0 to 1.2 s. This resulting  $S_u(t)$  curve is also plotted in Fig. 3.2. Comparison of the estimated  $S_u(t)$  curve versus the changes in the experimental flame speed shows that the change in the estimated burning velocity is significantly less than that observed experimentally. One can also see that for the small time delays, predicted burning velocity is less than the experimental flame speed, and this trend reverses for longer delays. It is also interesting to note that the estimated particle speed becomes equal to the experimental flame speed at the same delay time at which the experimental flame speed coincides with the computed burning velocity.

This observed effect of particle speed on flame propagation speed can be rationalized considering the contribution of particles into the heat transfer mechanisms. Indeed, Fig. 3.2 shows that when low time delays ( $t < 0.6$  s) were used, the particle velocities were higher than the flame propagation velocity, therefore, particles could have served as the heat transfer agents. This effect can be significant when particle velocities are appreciably different from the gas velocity. Microgravity could have been essential in observing this effect since the buoyant flows developing in normal gravity would significantly intensify the heat transport and mask the contribution of the moving particles.

Finally, it should be noted that the flames ignited after long delay times ( $t > 0.9$  s) extinguished after propagation over a length of 20 - 30 mm rather than propagated through the entire combustion chamber, as the flames ignited after shorter delay times. Because the constant pressure apparatus was used, a flow of cold outside air entered the combustion chamber as soon as the flame extinguished. This flow rapidly cooled the partially burnt aerosol in the combustion chamber.

### *Flame radiation*

Two optically filtered images of the flame were simultaneously acquired in each video frame using tilted mirrors and interference filters, as described above. Comparisons of the radiation profiles measured along the same line in each of the two filtered images of the magnesium flame showed, consistently with the previous observations using color differential images [2], that a zone dominated by the black body radiation exists ahead of the flame whereas MgO radiation dominates within the brighter flame zone. An example of the two intensity profiles illustrating this observation is shown in Fig. 3.3. When comparing the intensities of the two profiles, a correction for black body emissivity difference between the two wavelengths used should be taken into consideration. Using Planck's equation for the black body emission, the ratio of the radiations at the two wavelengths  $\lambda_1$  and  $\lambda_2$  is

$$\frac{E_{\lambda_1}}{E_{\lambda_2}} = \left( \frac{\lambda_1}{\lambda_2} \right)^{-5} \frac{e^{c_2/\lambda_2 T} - 1}{e^{c_2/\lambda_1 T} - 1} \quad (7)$$

where  $c_2=1.436 \text{ cm}\cdot\text{K}$ , and  $T$  is temperature. For  $\lambda_1=510 \text{ nm}$  and  $\lambda_2=500 \text{ nm}$ , the ratio varies approximately from 1.6 to 1.1 as the temperature increases from 1000 to 2500 K. Therefore, a radiation signal filtered through a 510 nm filter should noticeably exceed the signal filtered through a 500 nm filter at low temperatures and that difference should become almost negligible as the temperature increases. That agrees with the higher signal measured through the 510 nm filter ahead of the flame front (cf. Fig.3.3). In the combustion zone, the intensity measured for the 500 nm radiation significantly exceeds that for the 510 nm radiation, indicative of the strong MgO band radiation. A combustion zone dominated by 500 nm radiation was observed to form in all the microgravity combustion experiments indicating development of a vapor phase flame in which the MgO products were produced.

### *Combustion Product Size Distribution*

A dense cloud of airborne smoke was observed in the chamber after each experiment. This smoke, produced usually in a vapor phase flame was not analyzed and simply vented prior to collection of the powder from the chamber floor. Powders collected from the chamber after combustion experiments were examined using an optical microscope. Feret diameter defined as the diameter of a circle having the same area as the object and computed as  $d_F=(4\cdot\text{area}/\pi)^{0.5}$ , was determined for each particle with image analyzing software (UTHSCSA ImageTool) and used to produce particle size distributions. The size distributions of both unburnt Mg particles (size-classified using sieves with nominal sizes of 180 and 250  $\mu\text{m}$ ), and the burnt powders are shown in Fig. 3.4. Even though magnesium burns actively in the vapor phase, the burnt particle size do not show a decrease. Instead, a slight shift towards larger particle size is observed for the burnt powder as compared to the original magnesium. This shift is most likely due to a thick and porous oxide coating produced on burnt particles (see below).

### *Combustion Product Surface Morphology and Elemental Compositions*

An SEM was used to compare the surface morphology of unburnt and burnt metal particles. Electron dispersive spectroscopy (EDS) was used to compare qualitatively oxygen contents in surface layers of different samples. General views of various magnesium particles are shown in Fig. 3.5 and close-ups of the particle surface are shown in Fig. 3.6. Five particle samples chosen for the SEM and EDS analyses were unburnt (virgin) particles and particles collected after runs 53, 56, 57, and 60, in which ignition delays of 0.4 s (a typical delay used previously [1, 2]), 1.05 and 0.95 s (long delays), and 0.1 s (a short delay), respectively, were used. "Virgin" magnesium particles have clean surfaces with small size, white particles attached (Fig. 3.6a). EDS analyses using standardless calibration showed that these white particles consist of stoichiometric MgO. Surfaces of particles collected after experiments in which different ignition delays were used, were markedly different. Particles collected after both runs #53 and 60 with the ignition delays of 0.4 and 0.1 s, respectively, are coated with a fibrous layer (Fig. 3.6 b,d). This surface layer is similar to the oxide coating observed on particles quenched in single magnesium particle combustion experiments [5]. EDS measurements showed that these surface layers contained high amounts of oxygen, generally comparable to that detected in the small MgO particles on the surface of virgin magnesium. The surfaces of the particles collected after runs 56 and 57, in which long delays of 1.05 and 0.95 s,

respectively, were used, were indistinguishable from the surfaces of the unburnt particles. However, EDS showed significant oxygen presence in surface layers (the depth of the electron beam penetration is about 2-3  $\mu\text{m}$ ) for most of these particles (see Table 1). Surface morphology and oxygen content detected for particles collected after runs 56 and 57 are very different from any of the quenched single magnesium particle samples analyzed in an earlier research [5].

The internal elemental compositions were analyzed using EPMA for three cross-sectioned combustion product samples. These were the same combustion product samples for which surface elemental analyses were conducted using EDS: samples 53, 56, and 60 for which the ignition delays in microgravity experiments were 0.4, 1.05, and 0.1 s, respectively. EPMA oxygen content measurements were calibrated using a commercial MgO standard sample by C.M. Taylor. Magnesium content measurements were calibrated using cross-sections of the 99 % pure (Aldrich Chemical) magnesium particles employed in our experiments. Consistent with the previous observations of the particle surfaces, a thick oxide layer was present on the surfaces of particles quenched after runs 53 (see example in Fig. 3.7 a and b) and 60, but not on the particles collected after run 56 (in which a long ignition delay was used, see Fig. 3.8). The cross-sections revealed the highly porous structure of the oxide layer as shown in Fig. 3.7 b. The particle interiors were metallic and, according to our analyses, contained essentially pure magnesium for most of samples 53 and 60. Local regions with detectable oxygen content inside the particles were also observed, the maximum measured oxygen contents are shown in Table 1. Significantly higher oxygen contents were measured in most of the particles from the sample 56, for which the longest ignition delay was used in the microgravity experiment and a slow flame propagation was observed (cf. Fig. 3.2). This higher oxygen content is consistent with the high oxygen/magnesium peak ratios found for these particles from EDS, also shown in Table 1. Note, that several oxygen-free particles that could not be distinguished from the unburnt Mg were also observed in this sample.

Table 1. Summary of electron microprobe analyses of magnesium combustion products

Sample	Time delay used in microgravity test to suppress particle motion, s	Maximum oxygen content measured in cross-section (WDS), atomic %*	Oxide layer (yes/no)	Surface oxygen/magnesium peak ratio (EDS)
MgO	-	-	-	0.42
Mg	-	-	No	0.05
Run 60	0.1	0.47	Yes	0.42
Run 53	0.4	0.49	Yes	0.30
Run 57	0.95	-	No**	0.20**
Run 56	1.05	3.26	No	0.20

\* Oxygen detection limit is approximately 0.3 atomic %

\*\*Several particles coated with oxide were detected. These particles were not used for surface oxygen/magnesium peak ratio measurements.

#### *Combustion Products Bulk Compositions*

Combustion products of magnesium collected after the microgravity experiments were

analyzed using XRD. Four samples collected after runs 53, 56, 57, and 60 were used (the same samples that were selected for SEM and EPMA analyses). For reference, XRD spectra for coarse magnesium powders used in our experiments were also collected. Silicon powder was used as an internal standard in these analyses. The measured XRD spectra are shown in Fig. 3.9. XRD spectra for runs 53 and 60 showed both magnesium and magnesium oxide peaks. This result supports the electron microscopy analyses in which oxide layers were detected on surfaces of particles recovered after these runs. As shown in Fig. 3.9, only magnesium peaks appeared in the XRD spectra for runs 56 and 57, for which longer ignition delays were used and measured flame velocities were also very low. The sensitivity of these measurements for MgO is about 1 %. The absence of oxide in products collected after runs with long ignition delays determined from XRD analyses is, also, consistent with the electron microscopy results that showed no oxide layers on particles collected after runs 56 and 57 (“long” delays).

### 3.4. CONCLUDING REMARKS

Observations of the luminous flame structure using interference filters have shown that the pre-heat and combustion zones can be optically distinguished in magnesium aerosol flames in microgravity, consistent with the earlier results based on the comparison of the green and red portions of the video-signal [2].

An effect of particle motion on the flame propagation speed in microgravity has been observed. It appears that this can be attributed to the role the moving particles play in the heat transfer through a steady gas. When the particle speeds were lower than 0.1 m/s, the observed flame propagation speeds became less than predicted by a simplified model [8]. Such slow moving flames were observed to extinguish before propagating through the entire combustion chamber. More detailed modeling appears to be necessary to interpret these observations fully.

Radiation measurements showed strong MgO emission for all the flames, indicative of vapor phase Mg combustion and MgO formation. In addition, a dense smoke (MgO) cloud, usually produced by the vapor phase flame, was observed after all experiments. Despite this visible and spectroscopic similarity between the “slow” and “fast” flames, the surfaces of the combustion product particles are markedly different. Powders collected after the experiments in which the flame velocities were low (i.e., those with long time delays) had no MgO layer and were indistinguishable by SEM from those of the unburnt powder (Fig. 3.6, 3.8). In addition, MgO was not detected for these “slow” flame products by XRD measurements (Fig. 3.9). In “fast” flames, the SEM and XRD measurements (Figs. 3.6, 3.7, 3.9) clearly show MgO coating on particles. It thus seems clear that the deposition of the smoke oxide produced in the gas phase flame on the surface of burning particles was inefficient for the slow flames. It also appears reasonable to suggest that the oxide smoke deposition process might not be the primary source of the thick MgO layer found on the surfaces of particles collected after the experiments with shorter time delays and higher observed flame speeds.

A higher dissolved oxygen content was detected inside the oxide-free particles collected from the “slow” flames. Since in these experiments flame extinguished before propagation through the

entire chamber, it is suggested that these combustion products represent partially burned particles that were rapidly quenched due to flame extinguishment. The difference between these particles and those collected from "fast" flames is, therefore, in the completeness of their combustion and quenching rate. The presence of the thick oxide layer on the surfaces and absence of oxygen in the interiors of particles collected from "fast" flames is consistent with the combustion mechanism including the formation of an Mg-O solution inside burning particles that saturates and undergoes a phase change producing the MgO phase, as was previously proposed based on single particle combustion experiments [5]. The absence of a surface oxide layer and the presence of dissolved oxygen inside the particles collected from the "slow" flames indicate that the phase transition has not occurred for these particles, i.e., that the particles were quenched before the solution has saturated. The results of this work indicate that the MgO formation mechanism via the phase separation from Mg-O solution could contribute more significantly to the formation of an oxide coating than the MgO deposition from the vapor-phase flame.

### 3.5. REFERENCES

1. Dreizin, E.L., *NASA CP 10194, Fourth International Microgravity Combustion Workshop*, Cleveland OH 1997, pp. 55-60
2. Dreizin, E.L., and Hoffman, V.K., *Combust. Flame* 118:262-280 (1999)
3. Dreizin, C.H. Berman, V.K. Hoffmann, and E.P. Vicenzi E.L., *NASA CP 1999-208917, Fifth International Microgravity Combustion Workshop*, Cleveland OH 1999, pp. 216-218
4. Sun, J.H., Dobashi, R., and Hirano, T., *Combust. Flame* (in press, 1999)
5. Dreizin, E.L., C.H. Berman and E.P. Vicenzi *Combust. Flame* (in press, 1999)
6. Pearse, R.W.B., and Gaydon, A.G. *The identification of molecular spectra*. Halsted Press, NY, 1976
7. Baron, P.A., and Willeke, K., Gas and Particle Motion, in *Aerosol Measurement. Principles, Techniques and Applications* (K. Willeke and P.A. Baron, Eds) Van Nostrand Reinhold, New York , pp. 179-206 (1993)
8. Ballal, D.R., *Proc. R. Soc. Lond. A* 385, pp. 21-51 (1983)
9. Williams, F. A., *Combustion Theory*, Benjamin/Cummings Publishing Co., Menlo Park California, 1985



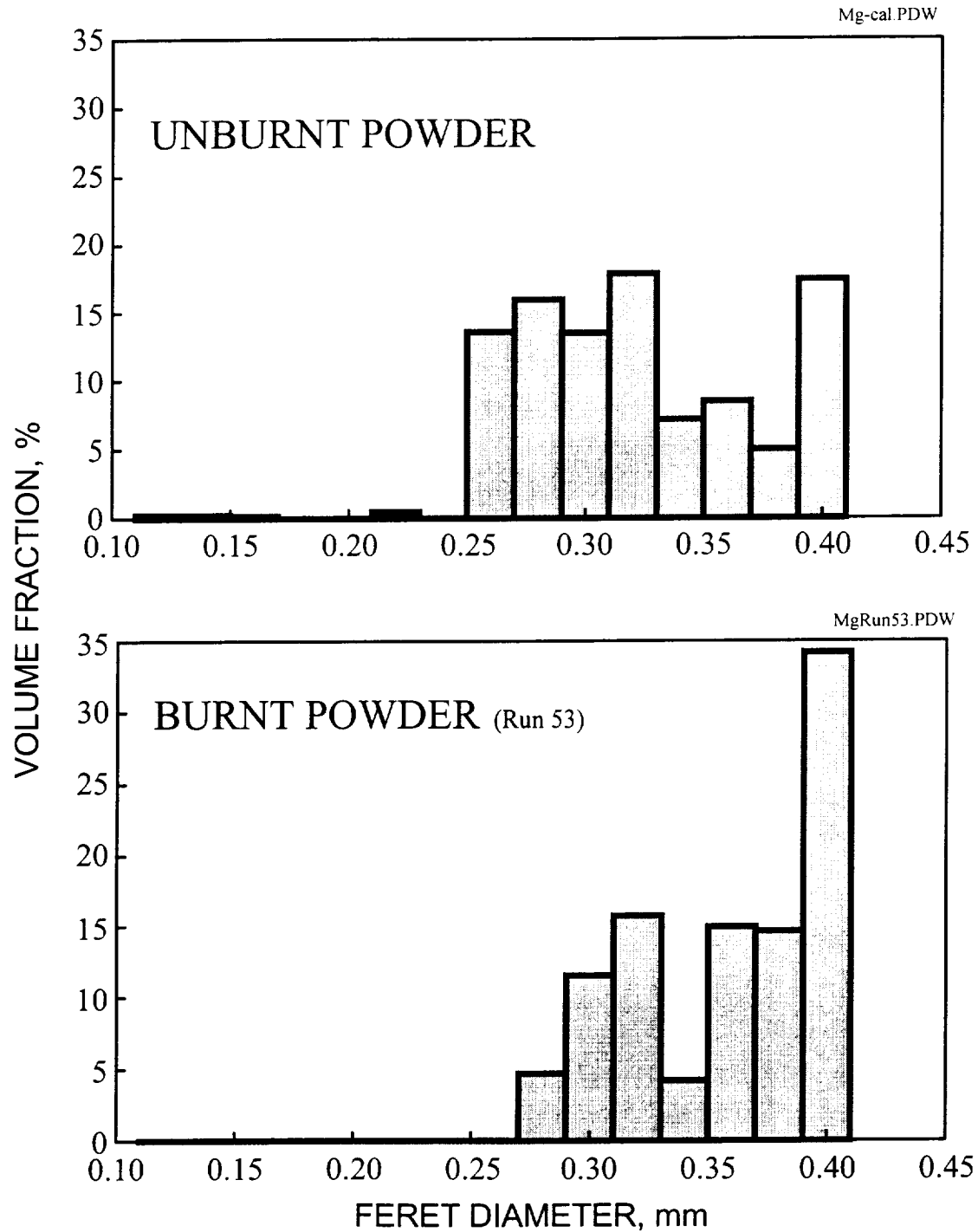


Fig. 3.4. Unburnt and burnt magnesium powder size distribution (normalized distributions using 500 particles)

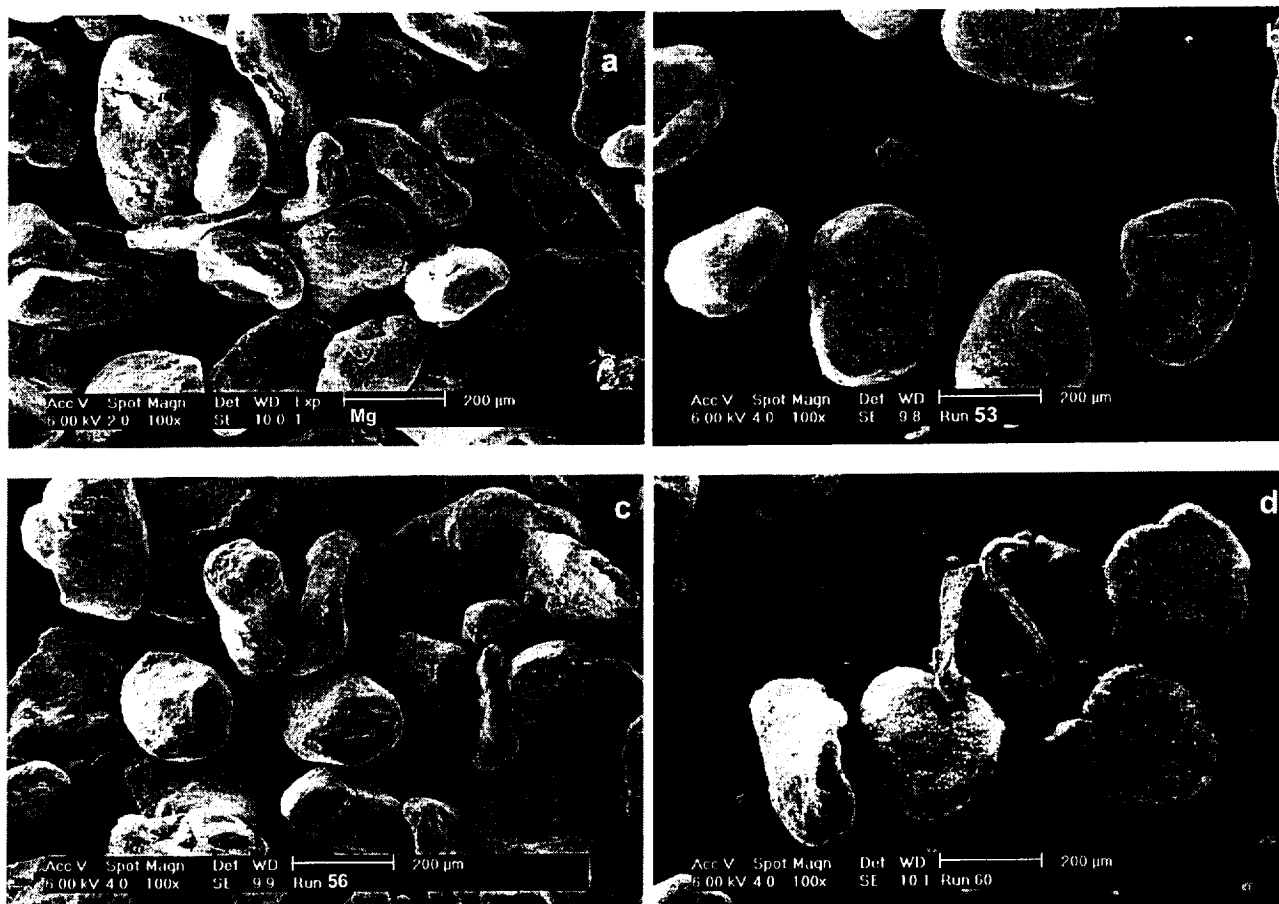


Fig. 3.5. SEM images of :  
a) "virgin" Mg particles;  
b) combustion products, Run 53, time delay 0.4 s  
c) combustion products, Run 56, time delay 1.05 s;  
d) combustion products, Run 60, time delay 0.1s;

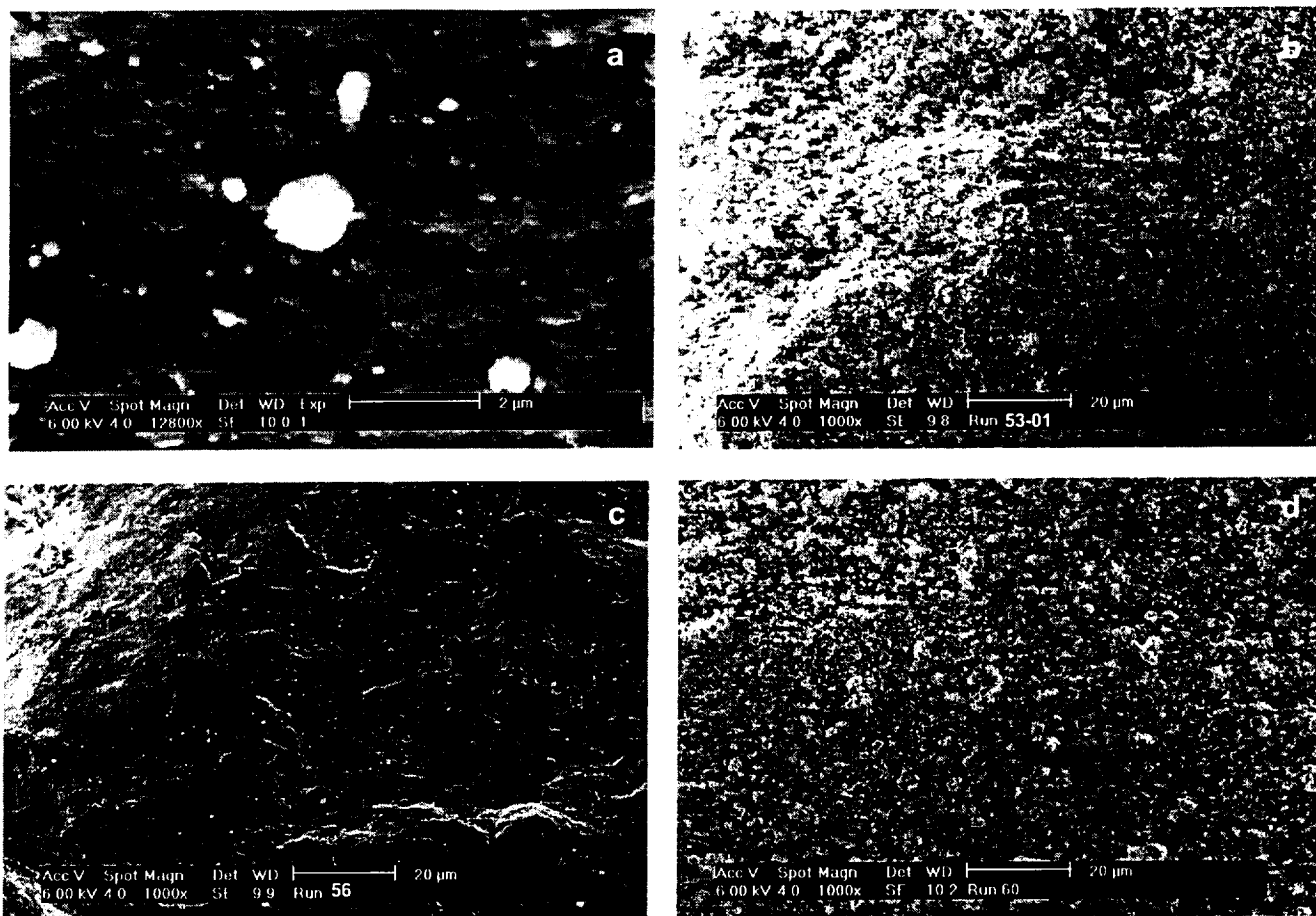


Fig. 3.6. SEM images of sutfaces of :  
a) "virgin" Mg particles;  
b) combustion products, Run 53, time delay 0.4 s  
c) combustion products, Run 56, time delay 1.05 s;  
d) combustion products, Run 60, time delay 0.1s;

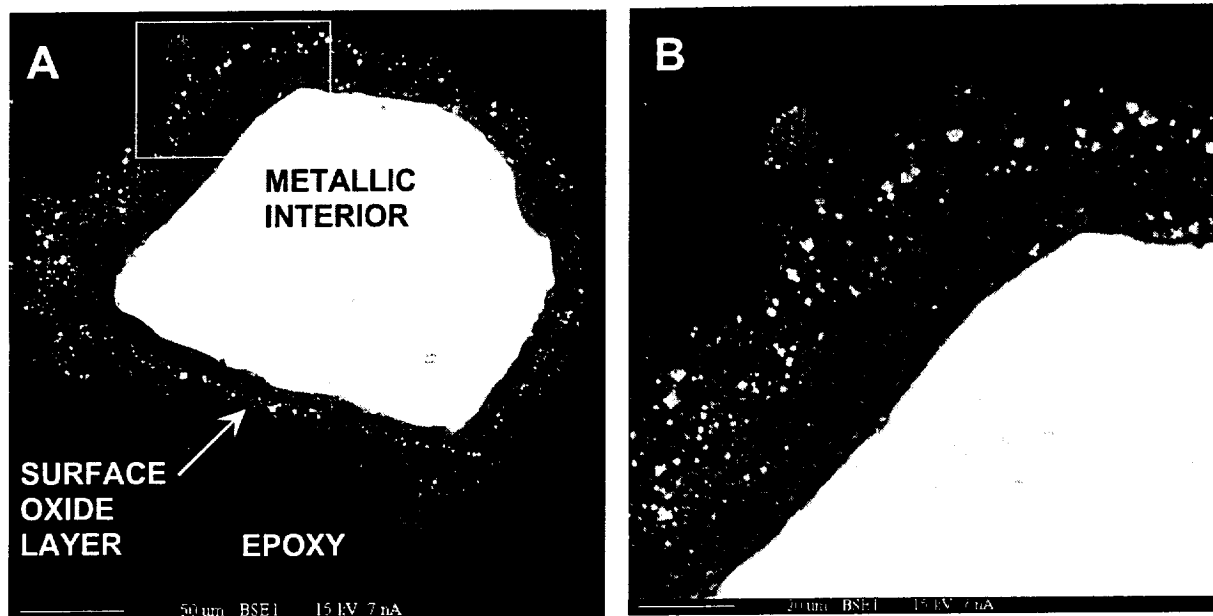


Fig. 3.7. Cross-section of a particle collected after microgravity Run 53 (ignition delay of 0.4 s) (A) and a close-up of a selected area showing the structure of the oxide layer (B).

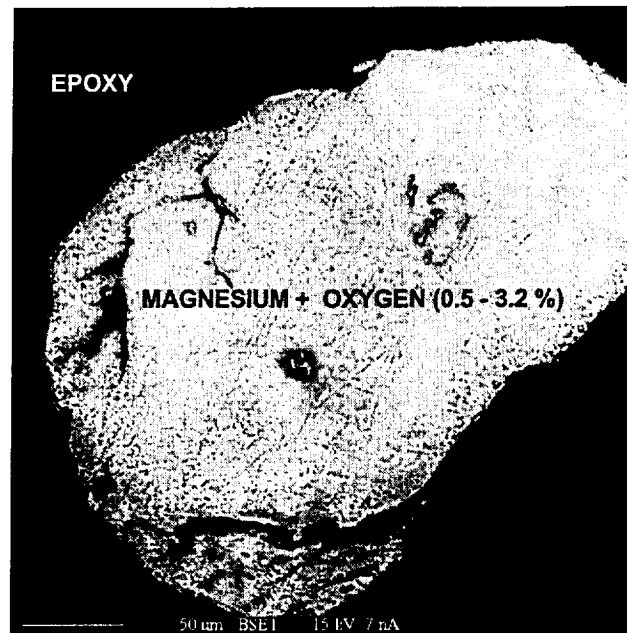


Fig. 3.8. Cross-section of a particle collected after microgravity Run 56 (ignition delay of 1.05 s)

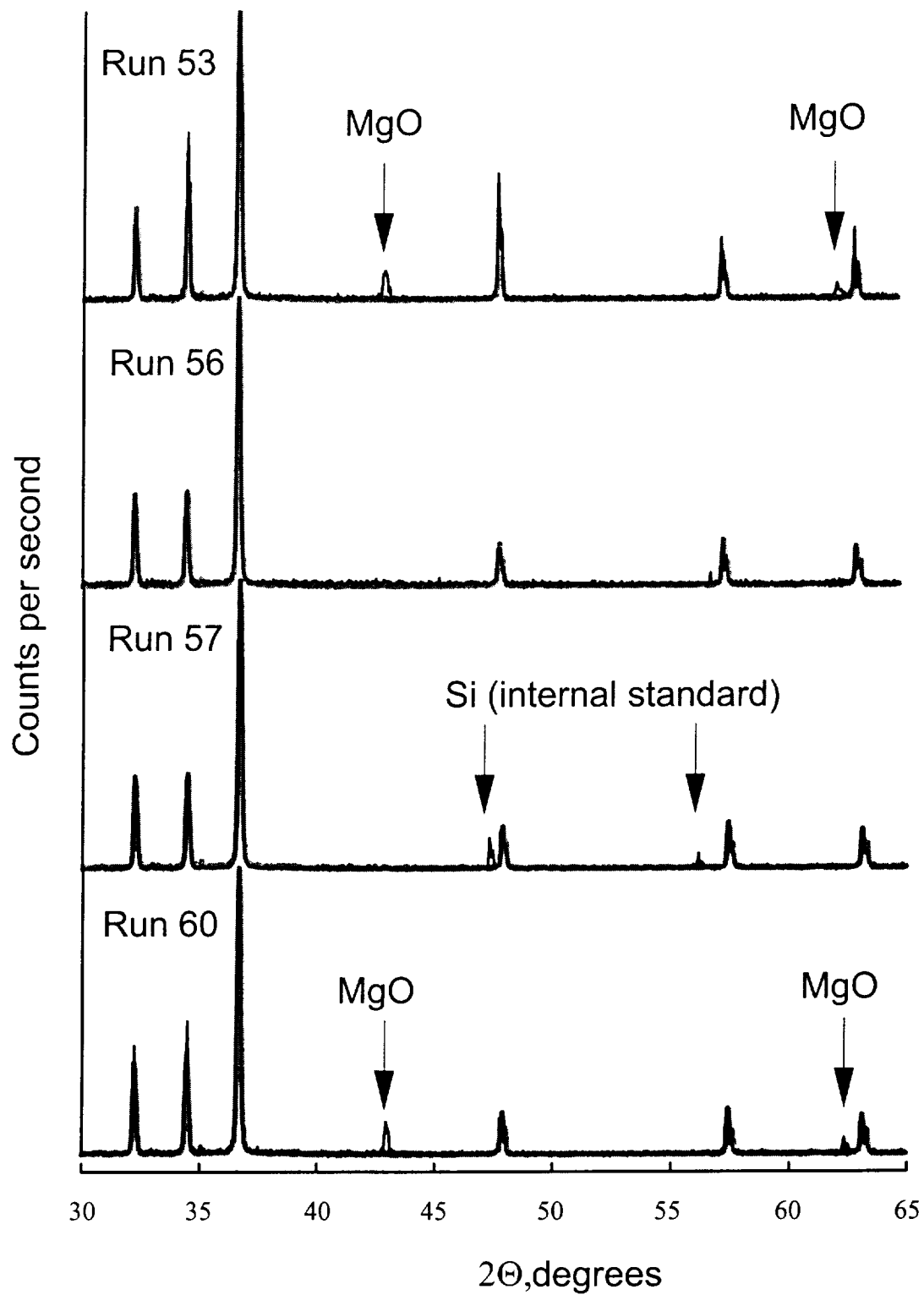


Fig. 3.9. XRD spectra of magnesium combustion products. Gray lines show spectrum for coarse magnesium powder used in experiments.

#### 4. MAGNESIUM AEROSOL COMBUSTION MODELING

This chapter discusses results of the modeling effort on flame propagation in magnesium cloud. A numerical model has been developed to interpret observed in microgravity experiments phenomena, such as variable flame speed, different directions for particle motion ahead and behind the flame zone, and flame extinguishment. It is also expected, that in the future, this model can be expanded and verified based on the results of the microgravity experiments, so that it will provide a useful and powerful tool for computational studying of the two-phase combustion phenomena.

The species considered are  $N_2$ ,  $O_2$ ,  $MgO$ , and  $Mg$  vapors and a condensed phase of  $Mg$ . The equations of conservation of the gas and condensed phase species are written in terms of the mole concentration  $[X_k]$  of those species. We will try to follow the notation of Kee and Miller [1].

Equations governing the conservation of each of the various species are in the form

$$\frac{\partial [X_k]}{\partial t} + \frac{\partial ([X_k] U_k)}{\partial x} = \frac{\partial}{\partial x} \left( D_k \frac{\partial [X_k]}{\partial x} \right) + \omega_k \quad (1)$$

where  $U_k$ ,  $D_k$ , and  $\omega_k$  are the species velocities, diffusion coefficients, and production rates, respectively.

The concentration for condensed phase  $Mg$  is taken as the product of the number of moles per particle and the particles per unit volume. The diffusion coefficients of all the gaseous species are taken to be that of  $N_2$  and scale as the  $3/2$  power of temperature [2]. The condensed phase  $MgO$  is taken to be finely divided and spread uniformly with the gas phase so that it will follow the gas motion.

The velocity of all the gases and the small  $MgO$  particles have the single value  $U_{gas}$ . For the condensed phase  $Mg$  particles the velocity  $V_{part}$  is computed considering inertia and drag forces acting on the particles:

$$\frac{dV_{part}}{dt} = \frac{1}{\tau} (U_{gas} - V_{part}) \quad (2)$$

with the particle velocity relaxation time  $\tau$  given by

$$\tau = \frac{D_p^2 \rho_p C}{18 \mu} \quad (3)$$

where  $D_p$  and  $\rho_p$  are the particle diameter and mass density, respectively,  $\mu$  is the gas viscosity, and  $C$  is a drag correction factor. The presently used choice,  $C = 1$ , corresponds to Stoke's drag law. Other values of  $C$  can represent finite Reynolds number effects for continuum flow or finite Knudsen number effects for rarefied flow.

All of the species, including the condensed phases, are considered to be in thermal equilibrium. A single energy equation is written with the convection velocity  $U_{gas}$  as shown next.

$$[M] \bar{C}_p \left( \frac{\partial T}{\partial t} + U_{gas} \frac{\partial T}{\partial x} \right) = \frac{\partial}{\partial x} \left( \lambda \frac{\partial T}{\partial x} \right) + \sum \omega_k H_k \quad (4)$$

Where T is temperature, [M] is the total molar concentration per unit volume (including the condensed phase Mg and MgO),  $\bar{C}_p$  is the mean molar specific heat,  $\lambda$  is the thermal conductivity of all the gas phase species,  $\omega_k$  is the molar production rate of each species, and  $H_k$  is the molar enthalpy of each species.

A separate equation could be written for the condensed phase Mg temperature, or the convective term in equation (4) above could be corrected to treat values of  $V_{part}$  that are not equal to  $U_{gas}$ . Such changes have not been implemented because the velocity differences are small and the temperature differences are estimated as being small.

The only reaction considered is



and its rate is determined from [3]

$$\omega_{Mg} = [X_{Mg}] [X_{O_2}]^{1/2} \exp\left(\frac{E}{RT}\right) \quad (6)$$

where  $E=167$  kJ/mol. The model assumes that the reaction occurs in the gas phase as the magnesium particles are vaporizing and the produced vapor quickly mixes with the ambient air.

Because the gas velocities are generally small, the combustion process occurs at essentially constant pressure. For this reason we impose a condition of constant pressure rather than using the standard equation of momentum that relates changes in pressure to changes in velocity.

Velocities are computed that satisfy constant pressure conditions of heat transfer, enthalpy changes due to reaction, and gaseous molar changes.

The aerosol is ignited by introducing an initial high-temperature region located at the closed wall of the combustion chamber. Temperature, velocity, and species profiles are computed as a function of time. Some preliminary computational results are shown below. Unburned gas velocity ahead of the flame front can serve as a general indicator of the flame propagation velocity visible in experiment. The velocities computed for two different ignition temperatures are shown in Fig. 4.1. The two temperatures used for these computations, 2700 and 3300 K are below and above the adiabatic flame temperature for Mg in air (3100 K). The higher ignition temperature results in the initially higher velocity, however, after about 0.5 s, the velocities in both cases become close. The order of magnitude of the velocity computed, 10 cm/s is in good agreement with the experimentally measured velocities of the combustion front. A more detailed view of the gas velocity field that develops in the burning magnesium particle aerosol is available from the plots in Fig. 4.2 showing gas velocities as a function of distance for different moments of the flame evolution. A minimum observed on each curve indicates effects of the consumption of Mg and  $O_2$  vapors in the flame zone. One can see that negative velocities are produced at some moments behind the flame front that is, again, consistent with the motion of particles in the direction opposed to that of the flame



propagation observed in some experiments. Computations for which the particles were allowed to burn as individual diffusion flames (i.e., reaction kinetics was assumed to be infinitely fast and the particle combustion rate was computed in a spherical diffusion flame approximation [4]) resulted in somewhat higher gas velocities.

The computations also predict changing local equivalence ratio. The plot in Fig. 4.3 shows the ratio of magnesium to oxygen ( $\text{Mg}/\text{O}_2$ ) as a function of distance for several different moments in the flame time evolution. One can see that initially, the  $\text{Mg}/\text{O}_2$  ratio changes monotonically from 2 (the initial ratio in the mixture) to infinity indicating the consumption of all the oxygen. However, at later times, a peak of the  $\text{Mg}/\text{O}_2$  ratio is produced just ahead of the combustion zone due to redistribution of magnesium particles.

Further computations and code development are anticipated to be carried out in the follow on research.

## REFERENCES

1. Lee, R.J., and Miller, J.A., A Structured Approach to the Computational Modeling of Chemical Kinetics and Molecular Transport in Flowing Systems. SAND86-8841 (1986)
2. Bird, B.R., Stewart, W.E., and Lightfoot, E.N., Transport Phenomena. J. Wiley & Sons, New York (1960)
3. Florko, A.V., Golovko, V.V., Ohrimenko, N.A., and Shevchuk, V.G., *Fizika Goreniya i Vzryva* 31:37-42 (1991)
4. Glassman, I. *Combustion* Third Edition, Academic Press, NY (1996)

## FIGURES

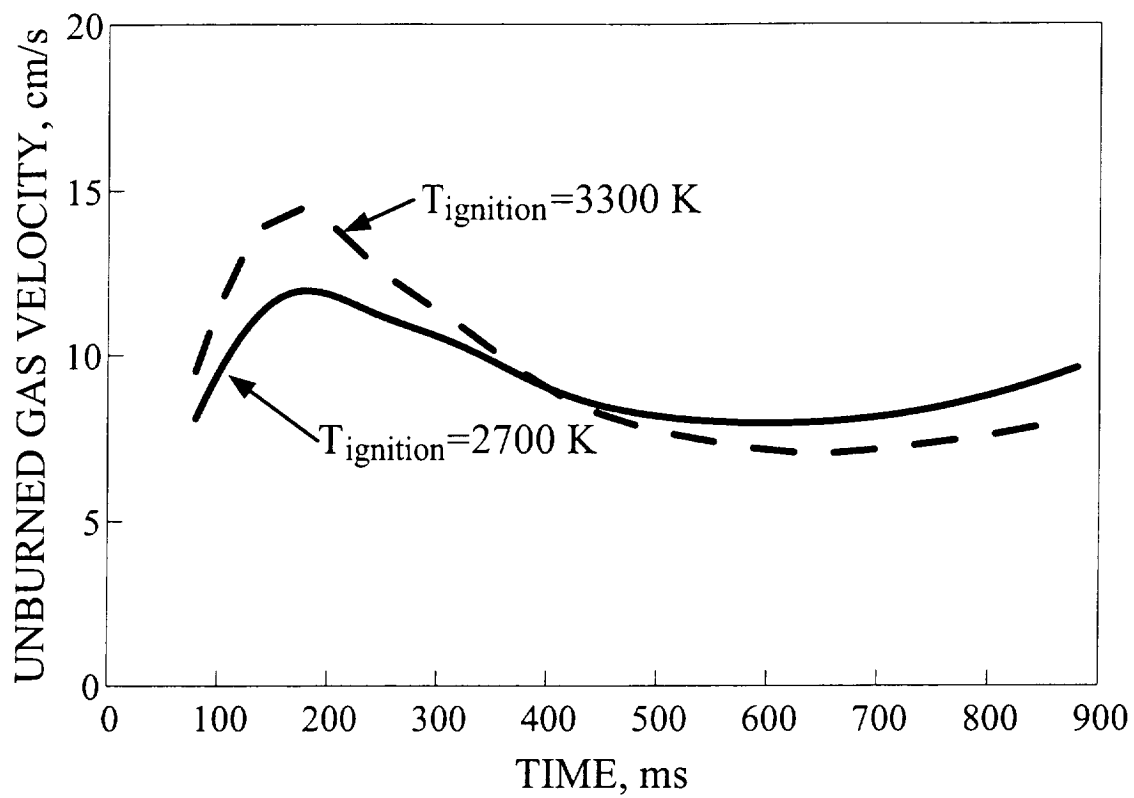


Fig. 4.1. Computed velocities of unburned gas as a function of time

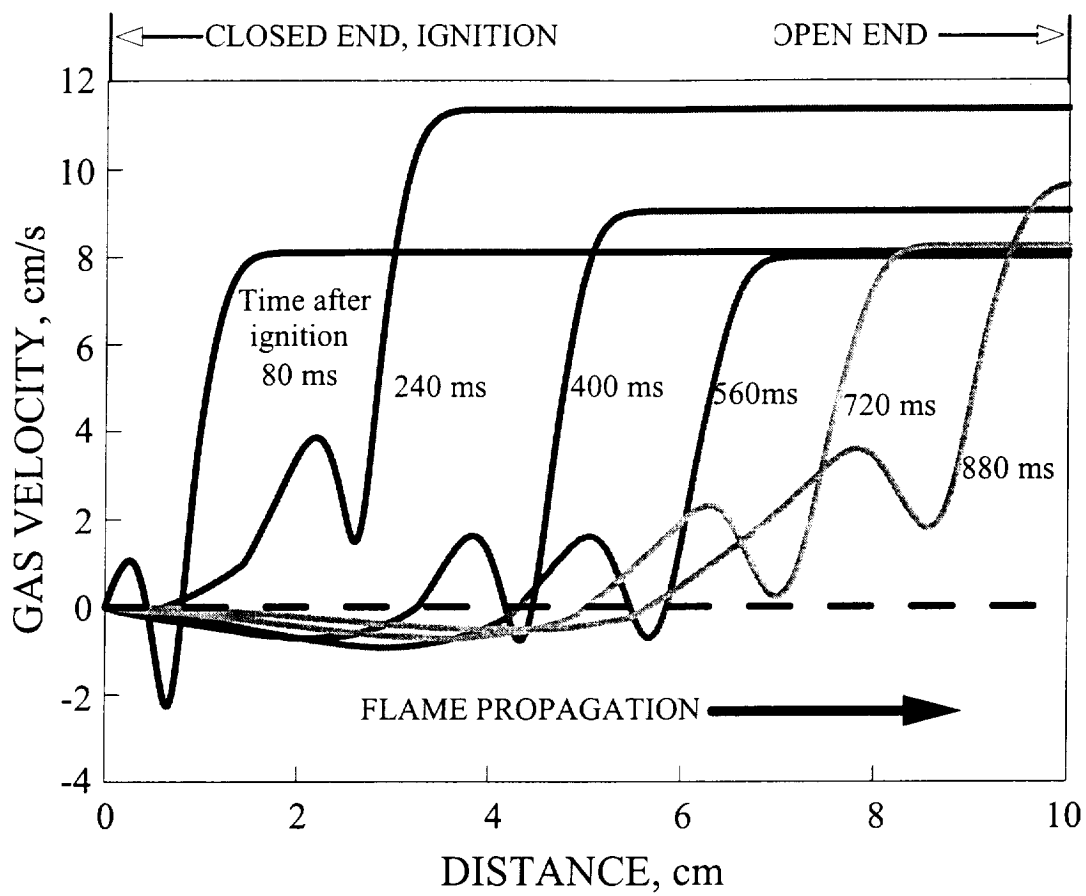


Fig. 4.2. Computed gas velocity profiles at different times

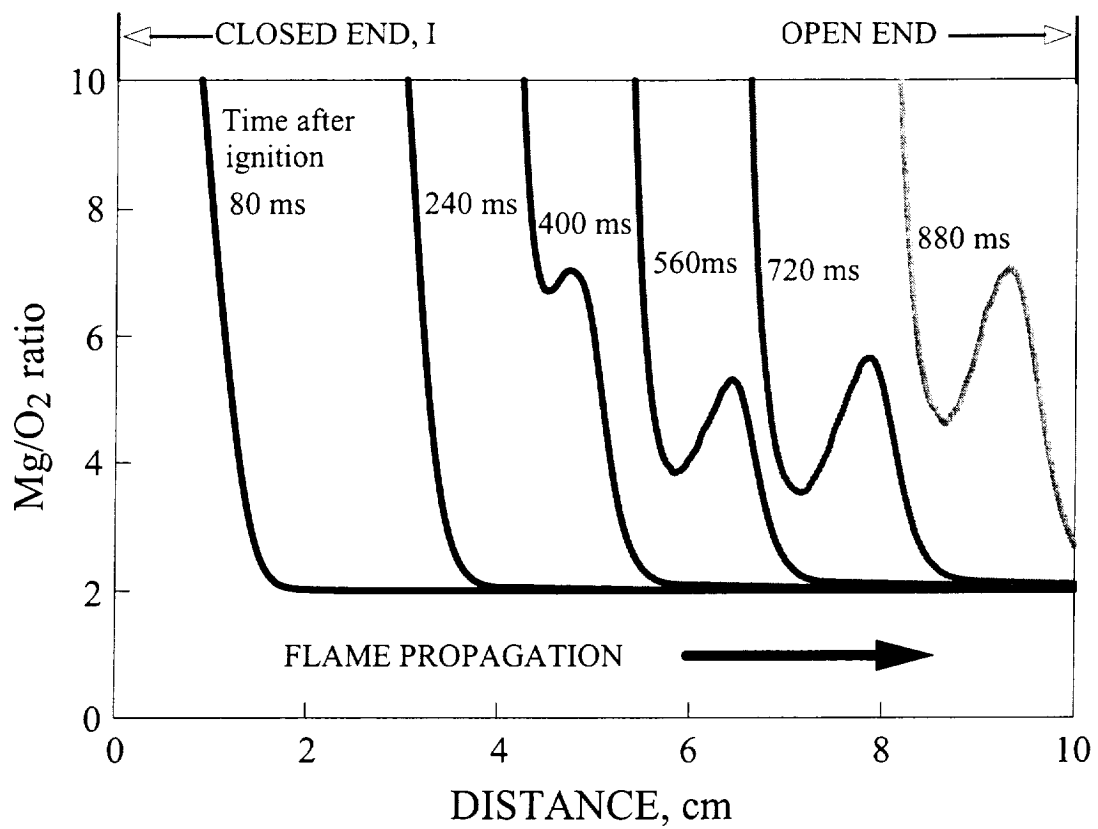


Fig. 4.3. Computed profiles for the Mg/O<sub>2</sub> mole ratio at different times

## 5. COMBUSTION OF AEROSOLIZED ZIRCONIUM AND TITANIUM PARTICLES IN MICROGRAVITY

### 5.1. FINE ZIRCONIUM POWDERS

Coarse zirconium particles (+50 Mesh, diameters greater than 297  $\mu\text{m}$ ) have been initially acquired but could not be ignited and finer particles (-375 Mesh, less than 44  $\mu\text{m}$  diameter) were used in the first series of microgravity experiments. In each experiment, a flame started to propagate from the igniter wire and was observed to consist of multiple bright spots, likely individual particle flames. A view of the flame structure from the high-speed movie images is shown in Fig. 5.1a. Large agglomerates are seen to form in the wake of the flame. These large, luminous agglomerates are observed to move around the chamber for a long time ( $\sim 0.5$  s) after the flame front vanishes. In some of the experiments, a secondary ignition occurred in the middle of the chamber (i.e., not in vicinity of the igniter wire). An example of the flame shape after the secondary ignition is shown in Fig. 5.1b. Two time differential images of the flame front for runs 70 and 72 shown in Fig. 5.2 indicate different processes developing in the flame front in these two runs. An almost continuous flame front formed in Run 70 whereas the flame front was composed of several less densely populated burning particle clouds in Run 72. Examination of the recorded films indicated that the secondary ignition occurred for those experiments in which the original flame front was not dense (e.g., runs 72, 73, and 75).

Two images of the flame were produced simultaneously using a regular speed video camera, tilted mirrors and two interference filters as was described earlier. In experiments with zirconium particles, filters with the wavelengths of 510 and 520 nm were used to separate black body and ZrO band radiation, respectively. An example of two filtered flame images is shown in Fig. 5.3. As expected, the overall radiation intensity is greater for the image taken through the 520 nm filter, but the flame shape is similar for both images.

Threshold tracking (Tracker software) was employed to follow the position of the flame front and estimate flame velocities for each experiment. The velocities were computed using both regular video (30 frames per second) and high-speed movie (270 frames per second in these experiments, less than the maximum of 400 f/s used in the previous experiments) images. Results of the flame front tracking measurements are shown in Fig. 5.4. Average flame velocities were estimated using linear fits for the flame position in time, as shown in Fig. 5.4. A summary of the parameters characterizing the zirconium combustion experiments and average flame velocities are given in Table 1.

TABLE 1. Summary of zirconium powder combustion experiments

Run #	Mass loaded, g	Average distance between particles		Equivalence ratio	Average flame speed m/s
		$\mu\text{m}$	particle diameters		
73	0.53	269	18.6	1.38	0.15
71	0.61	257	17.7	1.59	0.42
72	0.61	257	17.7	1.59	0.16
74	0.61	257	17.7	1.59	0.55
75	0.65	252	17.4	1.69	0.20
70	1.14	209	14.4	2.97	0.46
69	3.1	150	10.3	8.07	
68	4.9	128	8.9	12.75	2.12
67	5	101	7.0	13.01	1.02

A scanning electron microscope (SEM) was used to observe and compare the surface morphology of unburnt and burnt metal particles. SEM images of unburnt and burnt zirconium powders are shown in Fig. 5.5. Large agglomerates and multiple spherical particles of various sizes are clearly visible. Close-ups of the agglomerate surfaces showed multiple, various size, shapeless particles and spheres. Some spheres were broken indicating that some of them were hollow and others were not. The particle size distributions for unburnt and burnt powders are shown in Fig. 5.6. Average particle size is significantly greater for burnt powder, in addition, agglomerates produce a peak for particle sizes greater than  $27\ \mu\text{m}$  (that includes agglomerates of up to 1 mm diameter).

One possible mechanism for the formation of large agglomerates is due to the Stefan flow directed towards the particle surface. While the mechanism of individual zirconium particle combustion includes dissolution of both oxygen and nitrogen followed by nitrogen release and formation of a stoichiometric oxide [1], for a simple estimate this mechanism can be reduced to a zirconium-oxygen heterogeneous reaction with condensed  $\text{ZrO}_2$  as a product. Stefan flow is thus produced to compensate for the gas mass imbalance created by the inward oxygen diffusion to the burning particle surface that acts as an oxygen sink [2]. To roughly evaluate the significance of this effect we will consider a burning zirconium particle {1} with the radius  $R_1$  and a particle {2} with the radius  $R_2$  that is in vicinity of particle {1}. The time  $t_1$  required for the particle {1} to burn out will be compared to the time  $t_2$  required for the particle {2} entrained in the Stefan flow to reach the particle {1} surface.

Assuming that as a result of steady state, surface reaction the entire particle will be oxidized to  $\text{ZrO}_2$ , the combustion time  $t_1$  can be estimated as:

$$t_1 = \frac{4}{3} \frac{M_{O_2}}{M_{Zr}} \frac{\pi R_1^3 \rho_{Zr}}{I} \quad (1)$$

where  $M_{O_2}$  and  $M_{Zr}$  are molecular weights of oxygen and zirconium, respectively,  $\rho_{Zr}$  is the

zirconium density, and  $I$  is the mass flow rate of oxygen to the particle surface.

For a simple steady state diffusion controlled oxygen transport to the particle {1} surface, the mass flow rate of oxygen is [2]:

$$I = I_0 = 4\pi R_1 D (c_{O_2}^s - c_{O_2}^\infty) \quad (2)$$

where  $D$  is the diffusion coefficient,  $D = D_0 (T/T_0)^{1.75}$  for oxygen in air [3],  $D_0 = 0.178 \text{ cm}^2/\text{s}$ ,  $T$  is the temperature,  $T_0 = 273 \text{ K}$ , and  $c_{O_2}^s$  and  $c_{O_2}^\infty$  are oxygen mass concentrations at the particle surface and in the environment, respectively.

The combustion times predicted by Eq. (2) assuming that  $c_{O_2}^s = 0$  (while  $c_{O_2}^\infty = 0.2$ ) at the particle surface were compared versus experimental combustion times of single zirconium particles in air [1]. The comparison showed that the diffusion rate is underestimated, i.e., experimental times are shorter than predicted. Several factors could have contributed to this inconsistency, the most significant ones are the temperature gradient in air that efficiently increases the oxygen concentration gradient and the existence of a boundary layer due to particle motion. It has been found that the introduction of a boundary layer of thickness  $b$  equal to the particle radius ( $b = R_1$ ) allows one to achieve a good correlation between the estimated and experimental particle combustion times. Mathematically, the introduction of a boundary layer of thickness  $b$  is equivalent to the introduction of a boundary condition  $c_{O_2}^{r=b} = c_{O_2}^\infty = 0.2$ . This corrects the diffusion flow rate as [2]:

$$I = \frac{I_0}{1 - \frac{R_1}{R_1 + b}} \quad (3)$$

A plot showing combustion times  $t_1$  estimated using Eqs. (1) and (3) and experimental combustion times reported in Ref. [1] is shown in Fig. 5.7.

To estimate the time  $t_2$ , we will consider particle {2} to be entrained in the Stefan flow produced by the burning particle {1} with the gas velocity  $u_{St}$  that can be computed as [2]:

$$u_{St} = -D \frac{M_{air}}{M_{O_2} c_{air}} \frac{dc_{O_2}}{dr} \quad (4)$$

where  $c_{air}$  is mass concentration of air and  $M_{air}$  is molecular weight of air. The derivative  $\frac{dc_{O_2}}{dr}$  is the oxygen concentration gradient that can be determined as [2]:

$$\frac{dc_{O_2}}{dr} = -\frac{I}{4\pi D r^2} = \frac{I}{I_0} R_1 \frac{c_{O_2}}{r^2} \quad (5)$$

In the Stokes regime, particle {2} located at a distance  $r$  from the burning particle {1} will be entrained in the Stefan flow with an acceleration [4]:

$$a = \frac{6\pi\eta R_2}{m_2} (u_{st}(r) - v) \quad (6)$$

where  $\eta$  is dynamic viscosity, and  $m_2$  and  $v$  are the mass and velocity of particle {2}, respectively. Note that motion of the particle {2} is considered as one-dimensional, only along the line between the centers of particles {1} and {2}. Computing particle mass and substituting Eqs (3)- (5) in Eq. (6), we obtain for acceleration:

$$a = \frac{9}{2} \frac{\eta}{\rho_{Zr} R_2^2} \left( D \frac{M_{air}}{M_{O_2}} R_1 \frac{c_{O_2}}{c_{air}} \frac{1}{r^2} \left( 1 - \frac{R_1}{(R_1 + b)} \right) - v \right) \quad (7)$$

Using Eq. (7) for the acceleration of particle {2}, one can compute (numerically) the particle displacement versus time. The time  $t(r)$  when the distance  $r$  between the particles will become less than  $R_1 + R_2$  is considered as “collision time”,  $t_2$ . This time is a function of initial distance between the particles,  $r_0$ , and both  $R_1$  and  $R_2$ .

The plot in Fig. 5.8 shows the maximum size particles {2} that are predicted to be agglomerated with a given size particle {1}. All the particles with the sizes less than that shown by the line and positioned at a referred distance  $d$  (or closer) will be captured during the particle {1} combustion. For example, for an experimental particle separation,  $r_0 \approx 80 \mu\text{m}$ , the particles of average diameter of about  $12 \mu\text{m}$  used in our experiments would capture all the neighboring particles of the same and smaller size. The predicted effect is, therefore, very significant and can indeed cause strong particle agglomeration. It can further be amplified if unignited particles are captured by burning particles and ignite upon collision (e.g., because of contact with the hot burning surface). In this case, the burning time of the particle {1} becomes longer and its “sphere of influence” expands further.

The agglomeration due to Stefan flow becomes stronger for larger sizes of particle {1} but becomes less significant for larger sizes of particle {2}. Therefore, this effect may be significant in combustion of fine powders that are likely to be used in practical applications, such as propellants and explosives. Note that in normal gravity, buoyant flows can destroy the flow pattern produced due to Stefan flows and thus mask this effect.

## 5.2. COARSE POWDERS OF ZIRCONIUM AND TITANIUM

Coarse zirconium and titanium powders ( $\sim 160 \mu\text{m}$  average diameter, by Wah Chang Company) were used in these experiments. Velocities of flame propagation were measured for zirconium combustion experiments in which ignition delays were varied. The results of these measurements are shown in Fig. 5.9. For reference, an average particle velocity is also shown that was estimated for a  $160 \mu\text{m}$  diameter zirconium particle. Unlike the clear trend of slower flame velocities at longer ignition delays previously observed for magnesium, zirconium cloud flame velocity does not seem to depend on the ignition delays in the range covered by these experiments.



However, velocities in a wide range of 0.03 - 0.4 m/s were measured in the experiments in which the only controlled variable was the ignition delay. The spread of the measured velocities over a wide range for similar magnesium particle experiments has not been observed. Probably, that shows that for zirconium, aerosol flame speed is more sensitive to the uniformity of the cloud than for magnesium.

High-speed films showing flame evolution in more detail, both in terms of time and spatial resolution, have been preliminarily reviewed. An example of the flame appearance is shown in Fig. 5.10. As in the previous microgravity experiments using fine ( $\sim 14\text{ }\mu\text{m}$  average diameter) zirconium particles, the flame is observed to consist of multiple discrete single particle flames. Unexpectedly, it was found that zirconium particles burning in aerosol did not explode at the end of their combustion, unlike the same zirconium particles in single particle combustion experiments. In fact, in some of the microgravity experiments, when an aerosol flame was not established (presumably, because of the failure to well aerosolize the particles prior to ignition) single particle flames were observed. In these experiments, violent particle explosions were clearly visible, just like those occurring in normal gravity single particle experiments [1]. Also, multiple particle explosions were observed in the videos recorded during the previous set of microgravity experiments with fine zirconium particle clouds.

Combustion product particles were examined using optical microscopy and particle sizes have been analyzed for selected experiments with different measured flame velocities. Only a few spherical shape particles are found, whereas most of the particles have irregular shapes, similar to the shapes of the original zirconium powder. The measured size distributions for runs 91, 98, and 99 are shown in Fig. 5.11 together with the size distribution for the original zirconium particles used in these experiments. Average particle size for zirconium ( $168\text{ }\mu\text{m}$ ) is marked by a vertical line. The expected product size distribution was computed using the original powder size distribution and size correction due to the change in the molar mass and density of  $\text{ZrO}_2$  versus Zr. A solid line showing Gaussian profile for that computed product size distribution is also plotted for reference with each of the experimental product size distributions. The second vertical line shows the estimated size,  $192\text{ }\mu\text{m}$ , for a  $\text{ZrO}_2$  particle that would have been produced by oxidation of an average ( $168\text{ }\mu\text{m}$ ) size Zr particle. The peaks observed for particle sizes greater than  $300\text{ }\mu\text{m}$  are due to a small number of agglomerated particles observed in the combustion products. These agglomerates are clearly seen to consist of several particles bound together. The number of these particles is relatively small (e.g., 10 to 20 as compared to the total of 800-900 particles used for size distribution analyses), but due to their large size they produce significant peaks in the mass fraction distributions shown in Fig. 5.11.

Comparison of the overall shape of the size distribution measured in different experiments with the expected product size distribution indicates that the product particle sizes follow most closely the expected size distribution profile for run 98, in which the lowest flame speed was observed. Accordingly, the strongest shift towards the larger sizes is observed for products collected after Run 91 for which the flame speed was the highest. Thus, agglomeration appears to be more significant in the experiments in which the higher flame velocities are observed (see Fig. 5.11). However, in all the experiments with coarse Zr particles, the extent of the agglomeration is markedly

less than that observed in the earlier experiments with the fine Zr particles.

Combustion of clouds of titanium particles was qualitatively similar to those of zirconium. A summary of the experimental results is given below in Table 2. One can see that the flame velocities are, in general, comparable to those for the same size Zr particles (cf. Fig. 5.9). Similarly to zirconium, no clear trend of the dependency of the flame speed on ignition delay was observed. Flame appearance was also similar, containing multiple, clearly distinguishable individual particle flames. No particle explosions were observed in or behind the flame zone.

Clearly, the number of experiments available is very limited and additional experiments are needed for a more detailed characterization of Ti aerosol combustion.

TABLE 2. Summary of titanium powder combustion experiments

Run #	Ignition delay used, s	Mass, g	Distance between particles, mm	Equivalence ratio	Average flame speed m/s
102	0.6	1.3	1.55	4.83	0.098
104	0.9	1.3	1.55	4.83	0.079
105	0.4	1.3	1.55	4.83	0.078
106	0.8	1.3	1.55	4.83	0.056
111	1	1.63	1.44	6.06	0.020
112	1	1.63	1.44	6.06	0.063

### 5.3. REFERENCES

1. Molodetsky, I.E., Law, C.K., and Dreizin, E.L., *Twenty-Sixth Symposium (Int'l) on Combustion*, The Combustion Institute, Pittsburgh, 1997, pp. 1919-1927
2. Fuchs, N.A., *Evaporation and Droplet Growth in Gaseous Media*. Pergamon Press, London. Oxford, New York. Paris. (1959)
3. CRC Handbook of Chemistry and Physics. R.C. Weast, Ed., CRC Press, Cleveland, OH (1977)
4. Willeke, K., and Baron, P.A., *Aerosol Measurements: Principles, Techniques, and Applications*. Van Nostrand Reinhold. New York (1993)

## 5.4 FIGURES

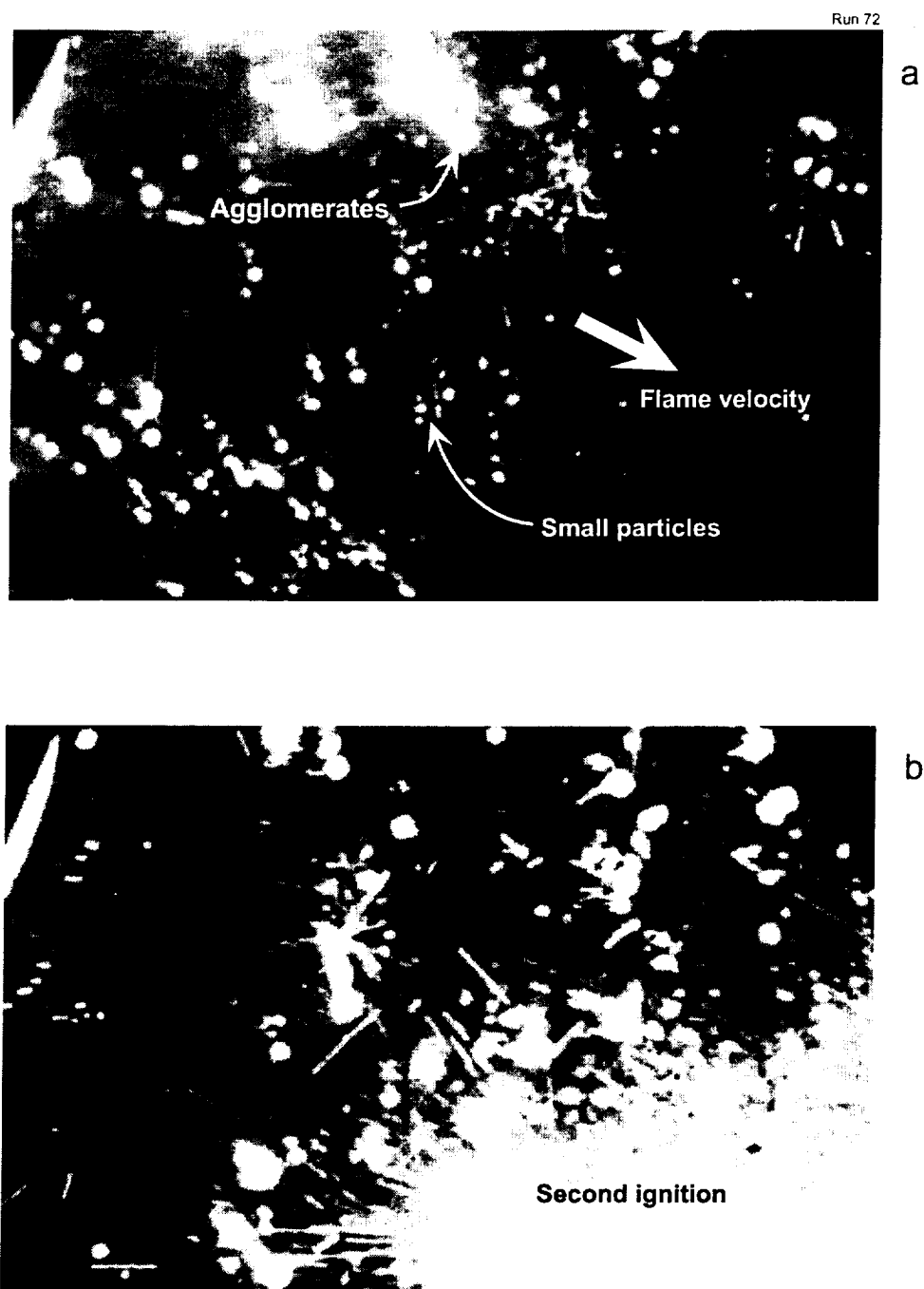


Fig. 5.1. High speed movie image of a zirconium cloud flame front (a) and secondary ignition (b)

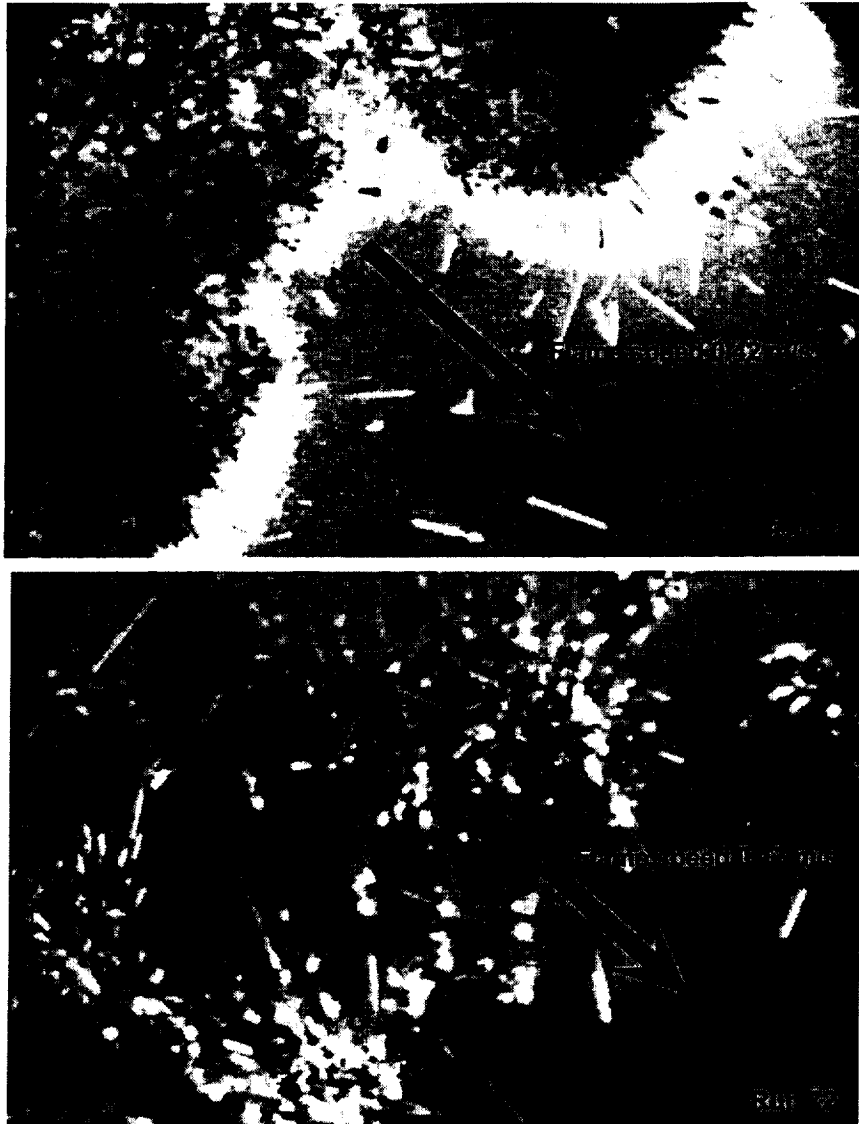


Fig. 5.2. Time-differential images showing flame propagation in zirconium particle cloud

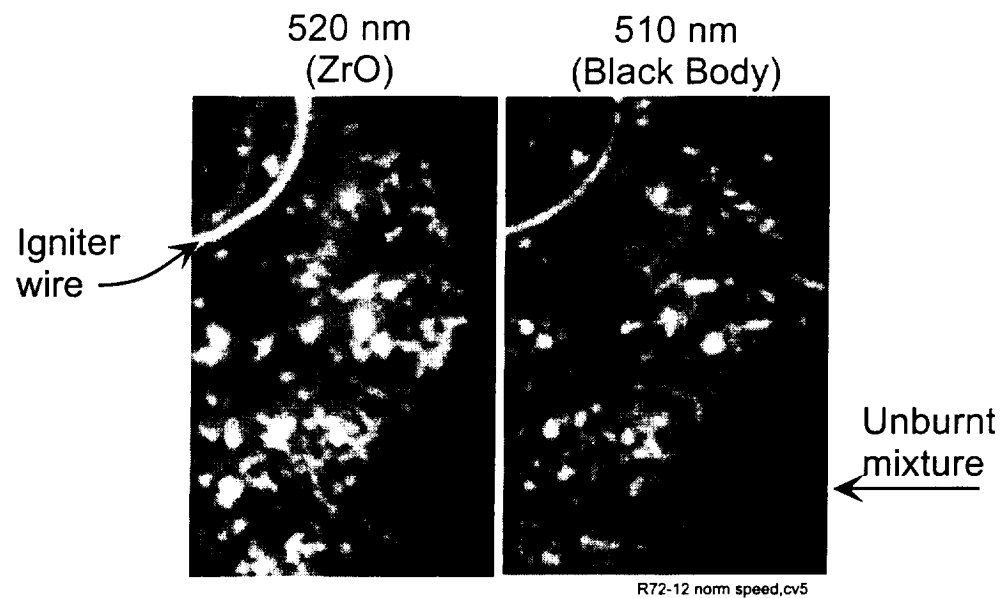


Fig. 5.3. Regular speed video images of a zirconium cloud flame front filtered to separate black body and  $\text{ZrO}_2$  radiation

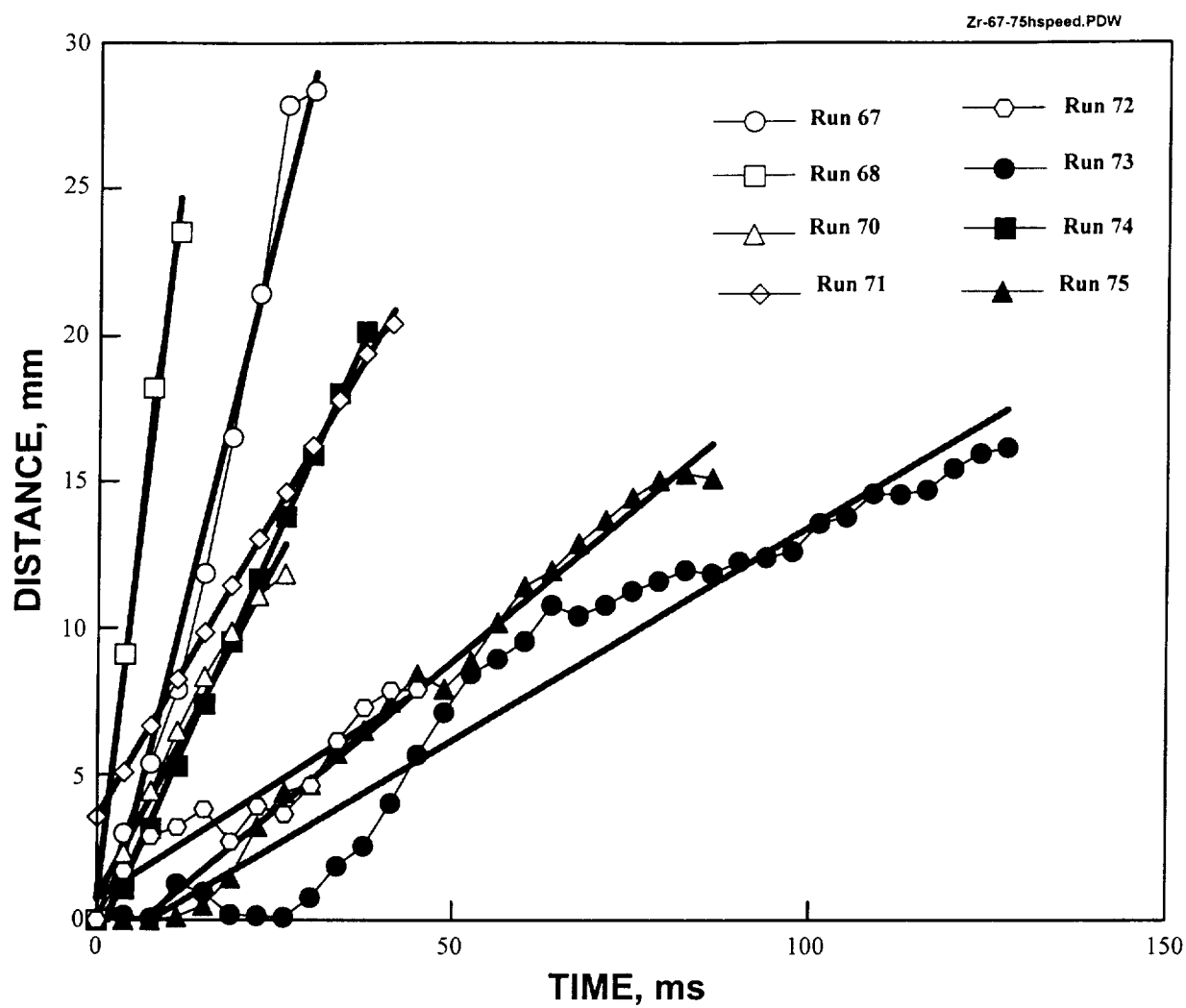


Fig. 5.4. Zirconium combustion flame front tracking measurements results

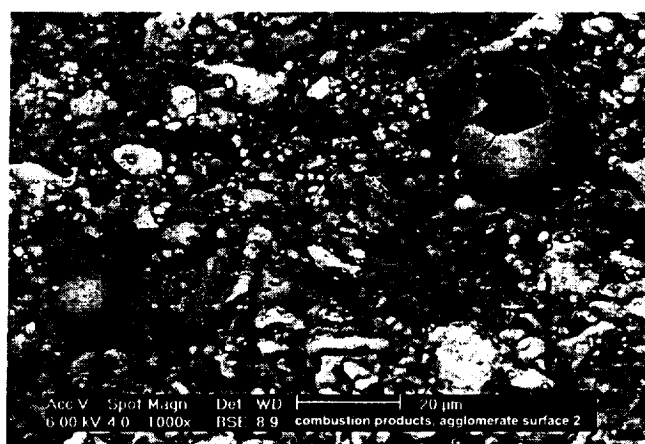
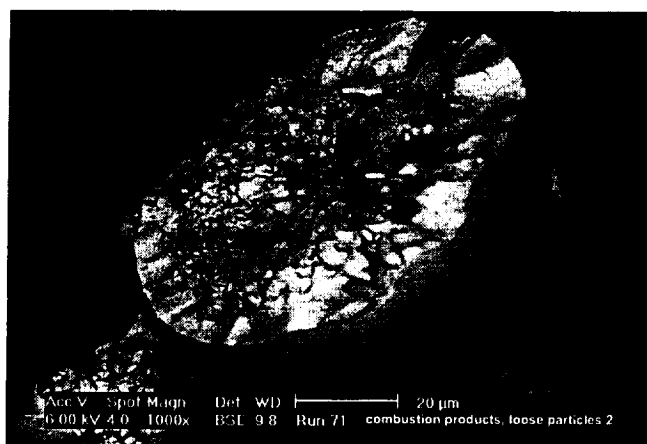
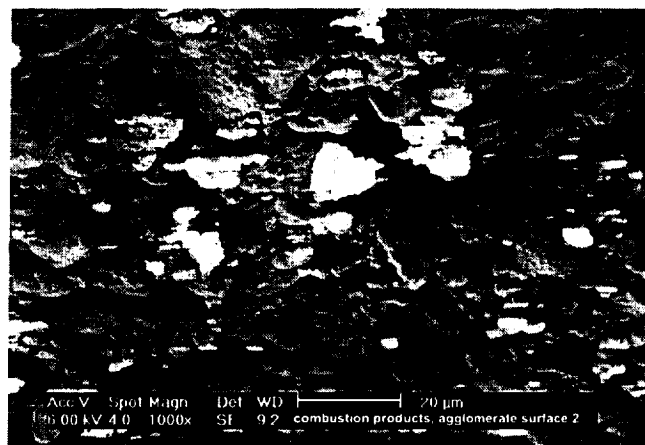
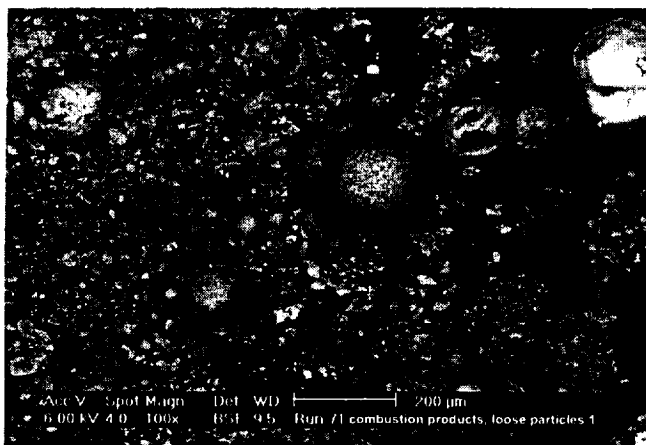
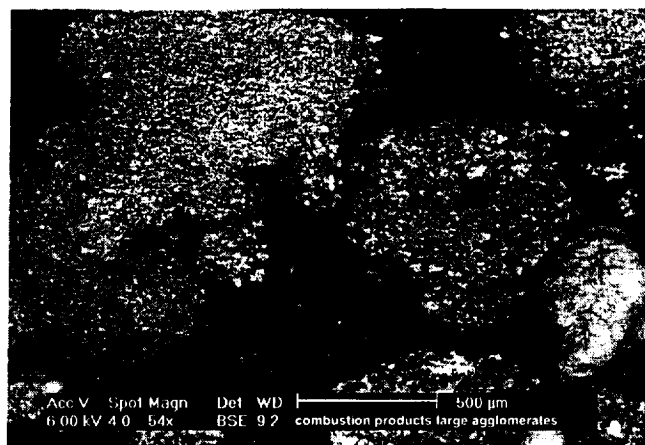
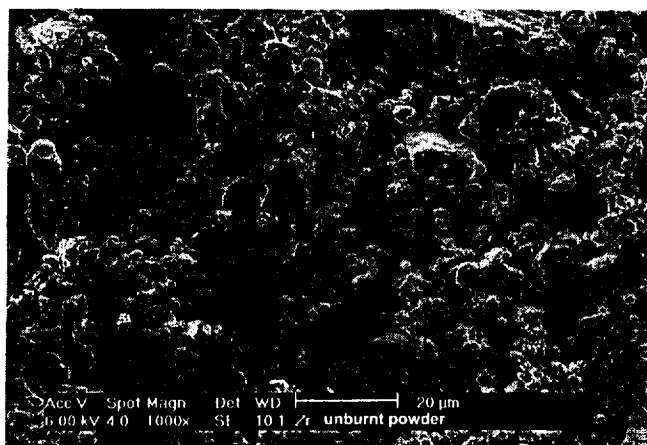


Fig. 5.5. SEM images of unburnt and burnt zirconium powder.

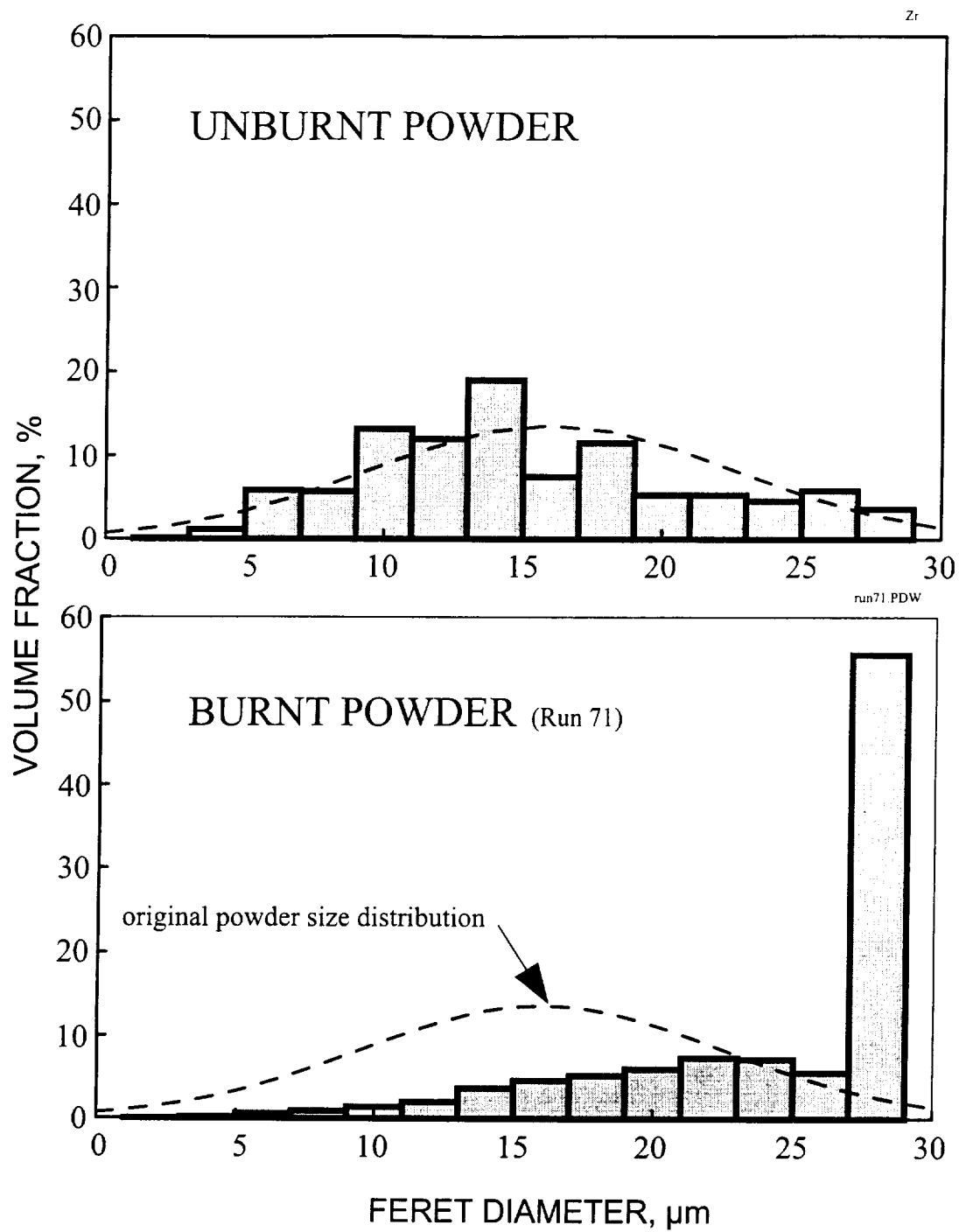


Fig. 5.6. Unburnt and burnt zirconium powder size distribution



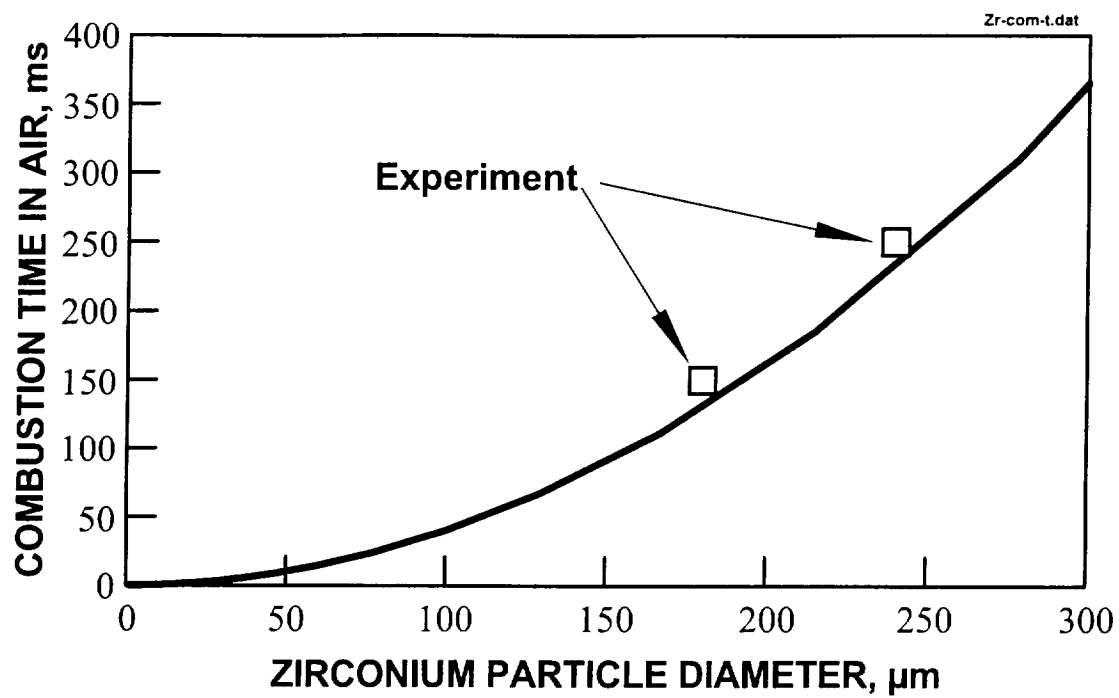


Fig. 5.7. Experimental [1] and estimated combustion times for Zr particles burning in air

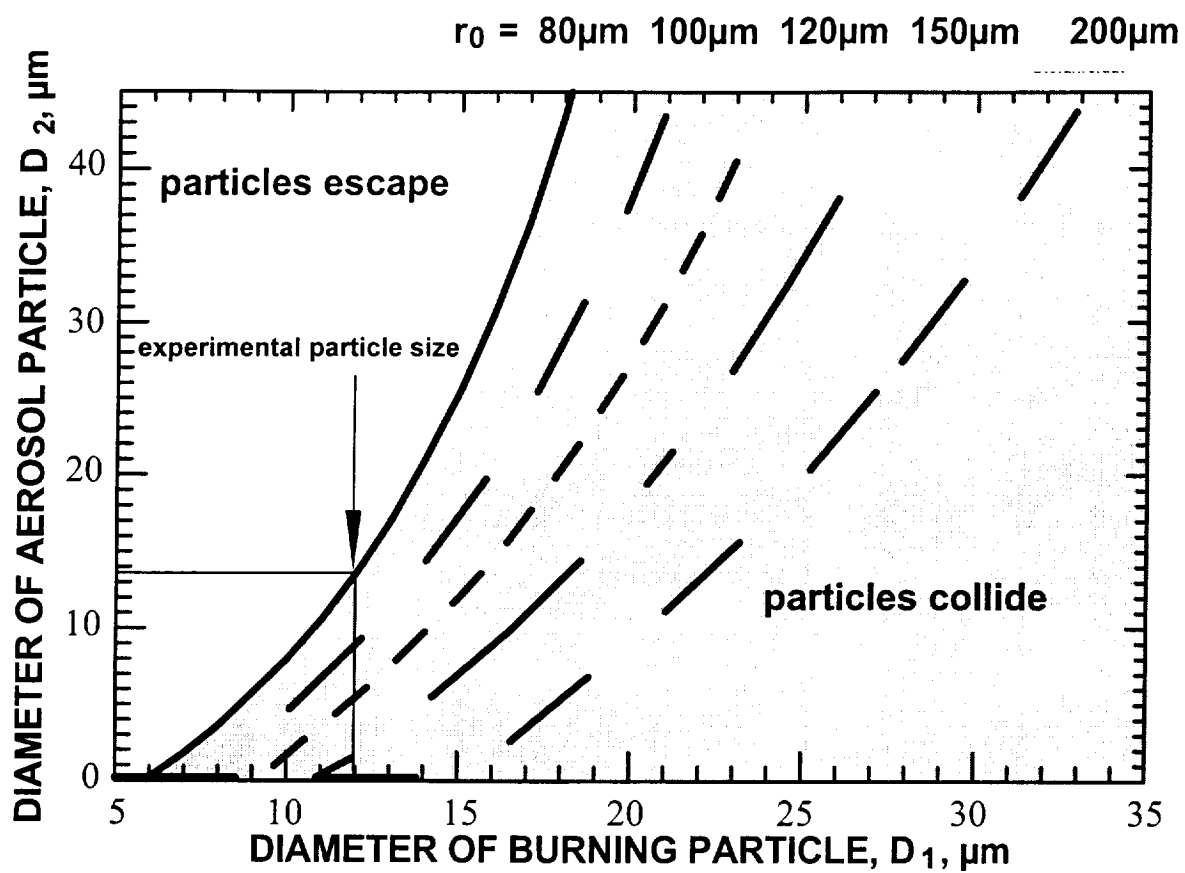


Fig. 5.8. Diameters  $D_2$  of aerosol particles adjacent to a Zr particle of diameter  $D_1$  burning in air that would agglomerate due to Stefan flow induced by the oxygen diffusion towards the burning particle

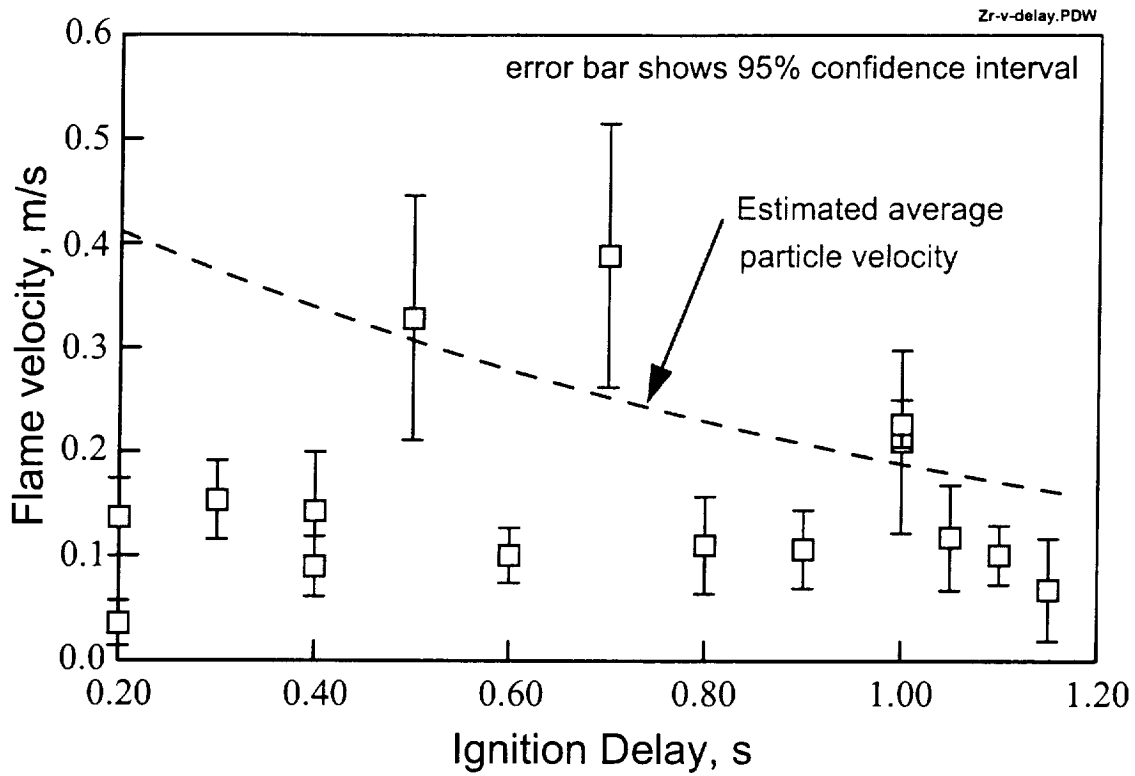


Fig. 5.9. Zirconium aerosol flame velocities observed at different ignition delay times.  
(particle average diameter 160  $\mu\text{m}$ )

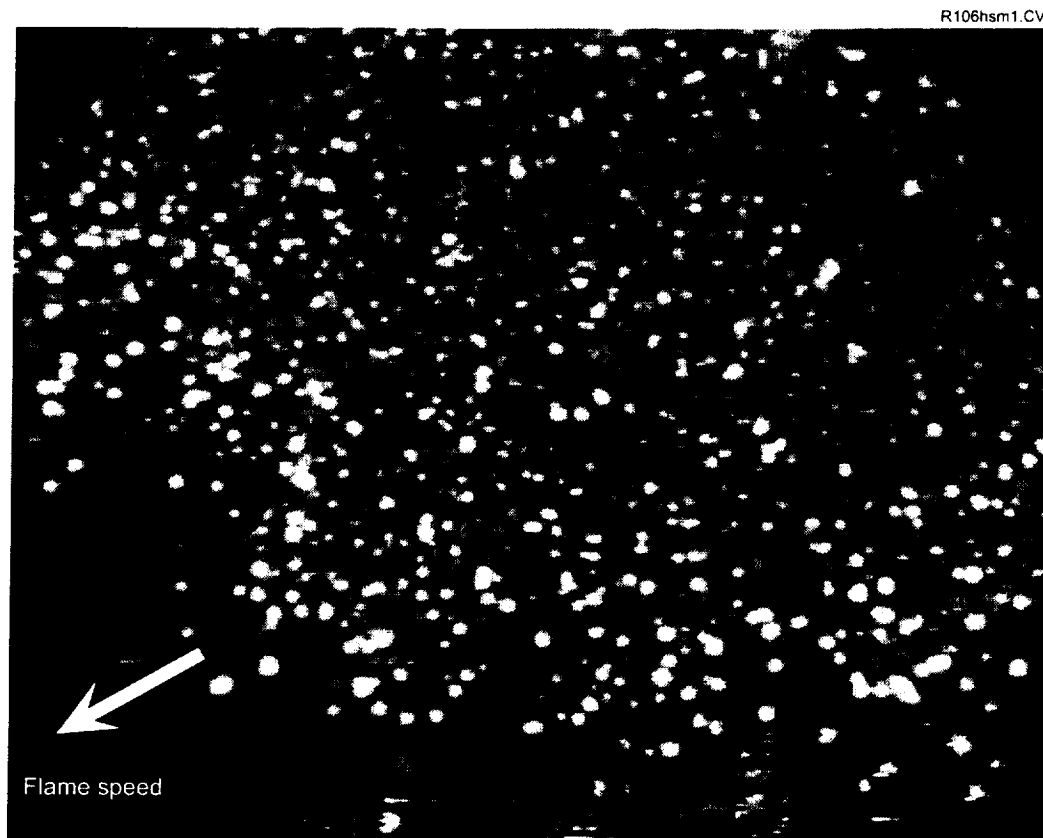


Fig. 5.10. A high-speed movie frame showing the structure of Zr cloud flame

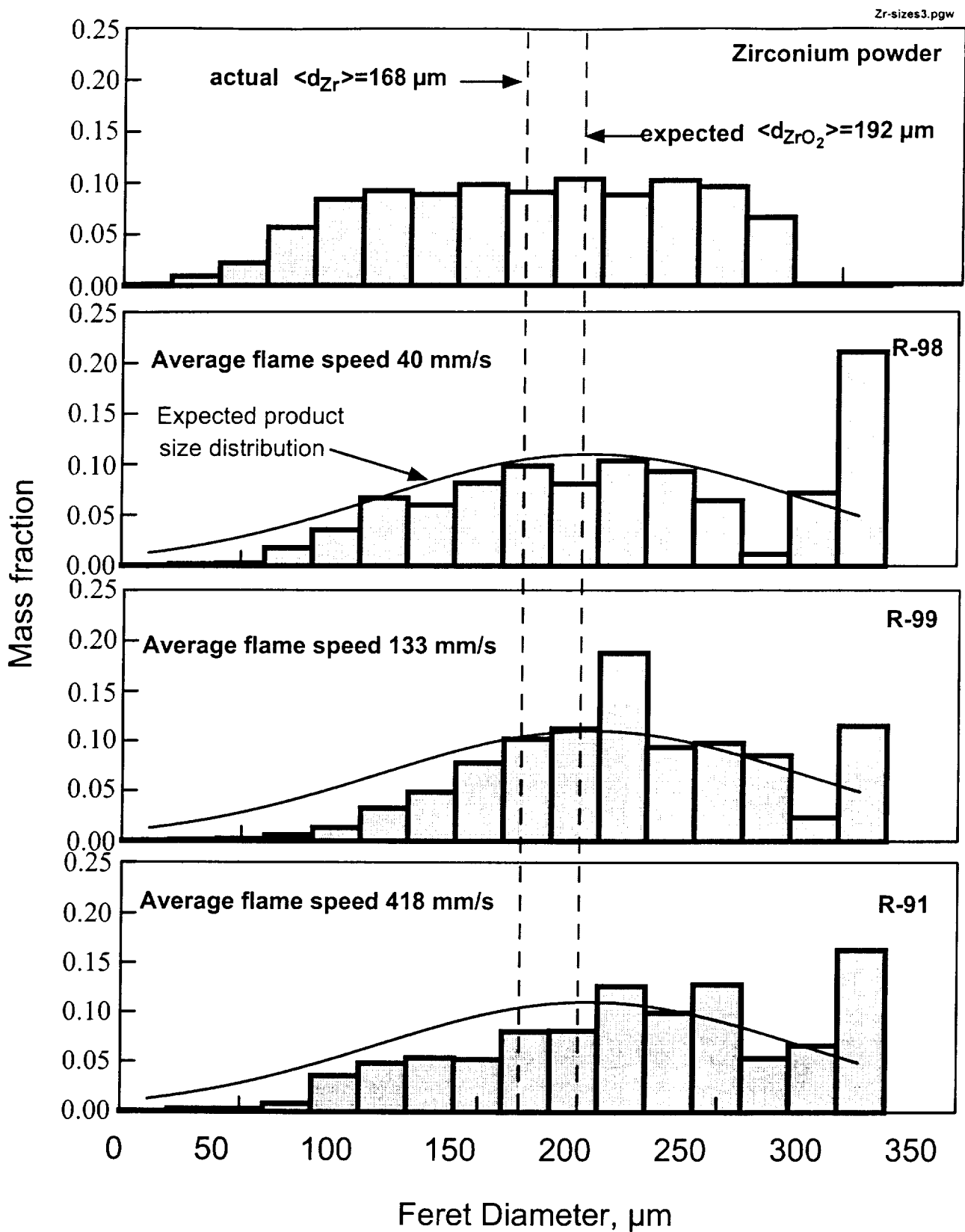


Fig. 5.11. Size distributions for original Zr powder and combustion products for selected microgravity experiments

## 6. HIGH TEMPERATURE PHASES IN TERNARY Zr-O-N SYSTEMS

Reference: Journal of Materials Research (in press, to appear in October 1999)

### ABSTRACT

Zirconium aerosol was ignited and burnt in atmospheric pressure air in microgravity using a 2.2 s drop tower. Combustion products were collected and analyzed using electron microscopy. The elemental composition analyses indicated that combustion product compositions fell along two linear traces on a ternary Zr-O-N diagram. Currently, the equilibrium Zr-O-N phases are not characterized at the temperatures above 2000 °C, typical of zirconium combustion in air, and it is suggested that the phases detected in zirconium combustion products can serve as a guide to further studies of the Zr-O-N system at high temperatures. It is also suggested that experimental metal combustion techniques can be adopted for studying high-temperature metal-gas phase equilibria.

### 6.1. INTRODUCTION

High-temperature portions of the metal-gas (specifically, metal-oxygen and metal-nitrogen) phase diagrams have been recently used to explain the occurrence of previously poorly understood metal combustion events, such as explosions and brightness jumps observed in burning metal particles [1-5]. Often however, the high-temperature portions of metal-gas phase diagrams and many phase equilibria that occur in ternary metal-gas systems are not well known. One reason is that the temperatures at which most metals burn exceed the temperatures accessible in furnaces employed in materials research. In addition, many metal-oxygen and metal-nitrogen phases formed from metal-gas reactions at high metal combustion temperatures are molten and difficult to handle. These experimental constraints virtually required that containerless methods be employed because most encapsulating materials will react with the metal and gas at conditions approaching those of metal combustion. This note suggests that metal combustion experiments can not only benefit from but also contribute to the area of materials science dealing with the metal gas phase diagrams and phase equilibria.

### 6.2. EXPERIMENTAL

Experiments on zirconium aerosol combustion in microgravity [6] were conducted and combustion product elemental compositions have been determined. Zirconium particles of 14.5 mm average diameter were aerosolized and ignited in a microgravity environment produced using the NASA Glenn Research Center 2.2 s drop tower. The flame propagated within a 0.5 L chamber that was connected to a 11.3 L vessel to maintain constant pressure during combustion. Details of the experimental apparatus and technique are discussed elsewhere [7,8]. Regular video and high-speed movie cameras were used to visualize microgravity combustion. The aerosol was ignited after a 0.5 s delay in microgravity used to achieve a steady flow-free condition after aerosolizing and burned for about 0.15-0.2 s. Since the microgravity environment continued for additional 1.4-1.6 s, combustion products cooled without contacting the walls of the chamber.

After the experiment, the combustion products were retrieved and examined using a Philips

XL30 Field Emission Scanning Electron Microscope. Samples of the products were embedded in epoxy, cross-sectioned, and polished to within 0.1  $\mu\text{m}$ . Elemental compositions were determined using a Cameca SX50 x-ray microanalyzer. Wavelength dispersive spectroscopy (WDS) analyses were conducted to determine local phase compositions. The x-ray monochromators and standard materials used for WDS analysis are as follows: W/Si multilayer (effective  $d=30\text{ \AA}$ ) for  $\text{N K}\alpha$  ( $\text{Si}_3\text{N}_4$ ) and  $\text{O K}\alpha$  ( $\text{ZrO}_2$ );  $\text{C}_5\text{H}_{12}\text{O}_4$  Pentaerythritol (PET) ( $d=4.375\text{ \AA}$ ) for  $\text{Zr L}\alpha$  (Zr). An accelerating voltage of 15 kV and a beam current of 20 nA were used during microanalysis.

In addition, samples of burnt powder were analyzed using a Siemens D500 x-ray Diffractometer (XRD) using  $\text{Cu K}\alpha_1$  radiation.

### 6.3. RESULTS AND DISCUSSION

Large numbers of 0.1-1 mm coalesced particles were observed in the combustion products. Cross-sectioning showed that most of them contained numerous voids that could have formed due to release of gas dissolved in the liquid metal at high combustion temperatures. Typical examples of the cross-sectioned coalesced particles imaged using backscattered electrons are shown in Fig. 6.1. Brightness in these images is a function of the average atomic number and, thus, for the Zr-O-N system, the zirconium-rich phases appear brighter and the phases rich with the dissolved gas (or stoichiometric oxide or nitride) appear darker. The images are characterized by brighter “inclusions” in a darker “matrix” phase.

Elemental compositions were obtained from several cross-sectioned particles and the data are represented by filled circles in a ternary diagram, Fig. 6.2. As indicated on the diagram, most of the brighter inclusions contain only small amounts of oxygen and some of them are rich in nitrogen. The more uniform, “matrix” phase is, in general, closer to the stoichiometric oxide. The observed phase composition appears to be consistent with the results of the single Zr particle combustion experiments [3] in which a phase rich in nitrogen was detected in the particles quenched at early times, but  $\text{ZrO}_2$  formed as the final combustion product. It is suggested that the observed composition of the coalesced particles could have formed if individual (small size) particles started to burn, acquired some nitrogen and then coalesced. Further oxidation of the already nitrogen-rich large coalesced particle would then produce a gradient of the dissolved oxygen and an oxygen-rich external layer would form.

The open squares plotted in Fig. 6.2 show locations of stoichiometric  $\text{ZrO}_2$  and  $\text{ZrN}$  for reference, and solid lines indicate the locations of the binary solid Zr-O and Zr-N solutions [9],  $\alpha\text{Zr}$  phases. It is interesting that our measured compositions appear to form two lines on the ternary diagram. One line, formed by compositions found in the matrix, coincides with the heavy dashed line showing all the possible compositions of  $\text{ZrO}_{2(1-x)}\text{N}_{4x/3}$ , a general formula for oxynitrides formed by the nitridation of zirconia. This line includes the compositions of a recently studied pseudo-binary  $\text{ZrN}_{4/3}\text{-ZrO}_2$  system and the open diamonds show the compositions corresponding to the  $\beta$  and  $\gamma$  phases reported to exist in such a system at temperatures below 970 and 840  $^\circ\text{C}$  respectively [10]. This line terminates at stoichiometric  $\text{ZrO}_2$ , the final product of zirconium combustion. Only a very small fraction of measurements closely approach the composition of  $\text{ZrO}_2$ ,

indicating that combustion was incomplete in these experiments. The second, short-dashed line, formed by the inclusion compositions, connects the nitride  $\text{ZrN}_{4/3}$  with the saturated Zr-O solid solution.

The XRD spectra measured for the burnt powder showed peaks correlated with those of both cubic and monoclinic  $\text{ZrO}_2$  phases,  $\text{ZrO}_{0.35}$  solid solution, and  $\text{ZrN}$ . The interpretation of these measurements is not obvious and analyses are currently in progress. It can be preliminarily noted that while the monoclinic phase is a stable low temperature oxide, the cubic phase is only stable above  $2357 \pm 30^\circ\text{C}$  [11]. However, it has been shown in Ref. [12] that the high-temperature oxynitride phase  $\text{ZrO}_{2(1-x)}\text{N}_{4x/3}$  decomposes below  $1000^\circ\text{C}$  to monoclinic zirconia and fluorite type (cubic)  $\beta$  oxynitride phases producing XRD peaks similar to those of the cubic zirconia. The standard of  $\text{ZrO}_{0.35}$  solid solution is produced by zirconium annealing at  $400^\circ\text{C}$  for one month and it is not clear whether a related phase detected in the burnt powder samples has been modified due to nitrogen presence. It should also be noted that stoichiometric  $\text{ZrN}$  composition has not been detected even though the typical  $\text{ZrN}$  peaks were observed.

Experimental procedures and conditions must be considered to interpret the phase compositions observed to form in our experiments and their role in phase equilibria at different temperatures. As one reference point, the maximum temperature of zirconium particle combustion in air is about  $2400^\circ\text{C}$  [3]. The elemental compositions observed in the combustion products do not coincide with the locations of the  $\beta$  and  $\gamma$  phases reported to be stable at low temperatures. It is thus reasonable to suggest that the compositions of the combustion products represent possible local equilibria in the Zr-O-N system at temperatures above  $970^\circ\text{C}$ . Measurements in which the cooling rates are varied or the combustion products are annealed in order to better characterize presently unknown phase equilibria in the Zr-O-N ternary system at high temperatures represent an obvious next step in further research.

Finally, it is worth noting that similar metal combustion experiments conducted with attention to the heating rate, maximum temperature, and quenching conditions could be useful for studies of high-temperature metal-gas equilibria.

#### 6.4. REFERENCES

1. Dreizin, E.L., *Combust. Flame*, 105:541-556 (1996)
2. Dreizin, E.L., and Molodetsky, I.E., *Mat. Res. Soc. Symp. Proc.* Vol. 418, pp. 195-200, 1996.
3. Molodetsky, I.E., Law, C.K., and Dreizin, E.L., *Twenty-Sixth Symposium (Int'l) on Combustion*, The Combustion Institute, Pittsburgh, 1997, pp. 1919-1927
4. Molodetsky, I.E., Vicenzi, E.P., Law, C.K., and Dreizin, E.L. *Combust. Flame*, 112:522-532 (1998)
5. Dreizin, E.L., *Combust. Flame*, 116:323-333 (1999)
6. Dreizin, E.L., Berman, C.H., Hoffmann, V.K., and Vicenzi, E.P. *NASA C/P-1999-208917, Fifth International Microgravity Combustion Workshop*, Cleveland OH 1999, pp. 215-218.
7. Dreizin, E.L., *NASA Conference Publication 10194, Fourth International Microgravity Combustion Workshop*, Cleveland OH 1997, pp. 55-60.



8. Dreizin, E.L., and Hoffmann, V.K., *Combust. Flame*, 118:262-280 (1999)
9. Massalski, T.B., Okamoto, H., Subramanian, P.R., and Kacprzak, L. (Eds) *Binary Alloy Phase Diagrams*. ASM Publ., Materials Park, OH, 1990
10. Lerch M., *Journal of Materials Science Letters*, 17: 441-443 (1998)
11. Ackerman, R.J., Rauh, E.G., Alexander, C.A., *High-Temperature Science*, 7:304-316 (1979)
12. Lerch, M., Krumeich, F., Hock, R., *Solid State Ionics*, 95:87-93 (1997)

## 6.5. FIGURES

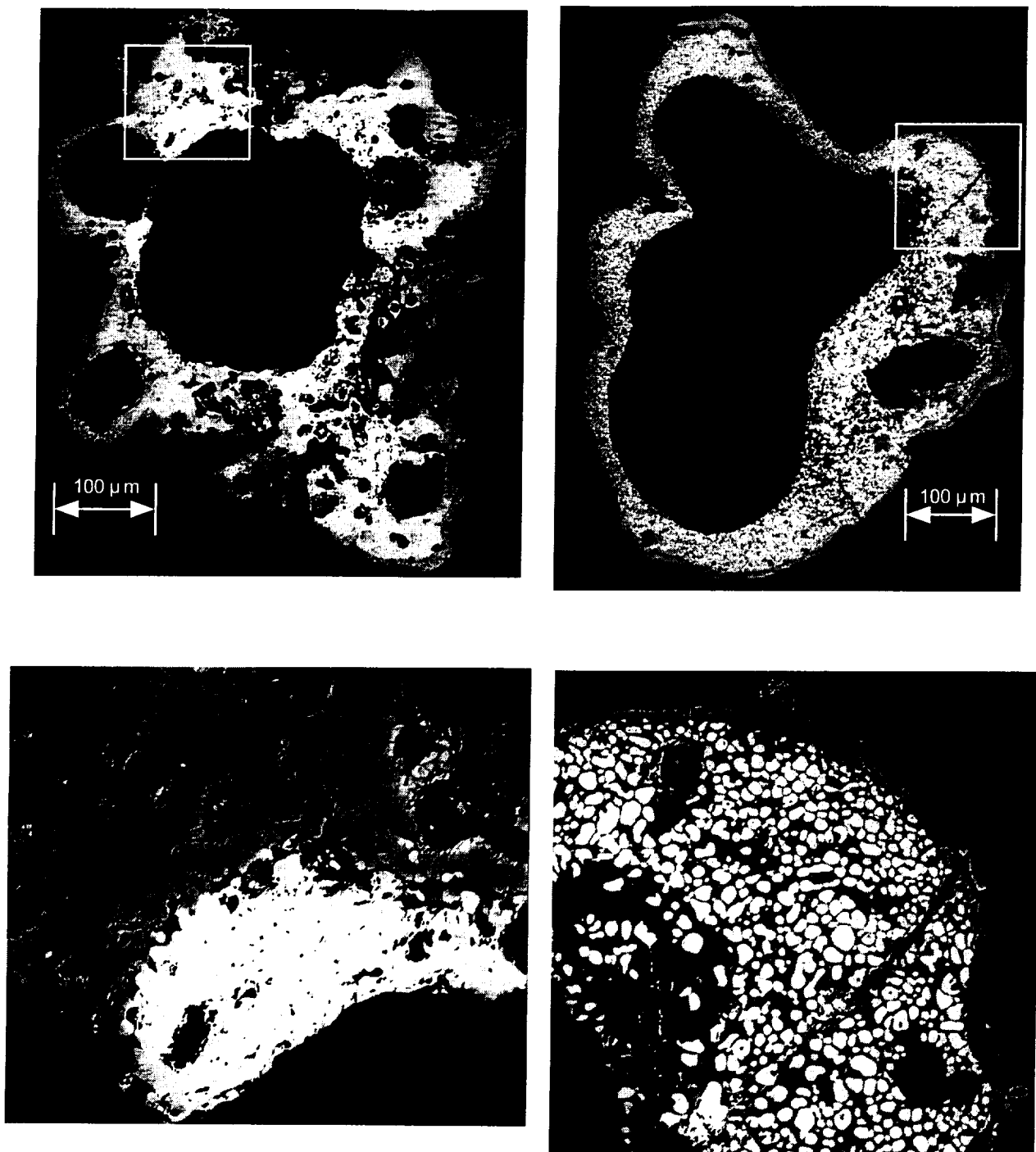


Fig. 6.1. Representative backscattered electron images of cross-sectioned zirconium combustion products (general view of agglomerate and closeup showing internal structure)

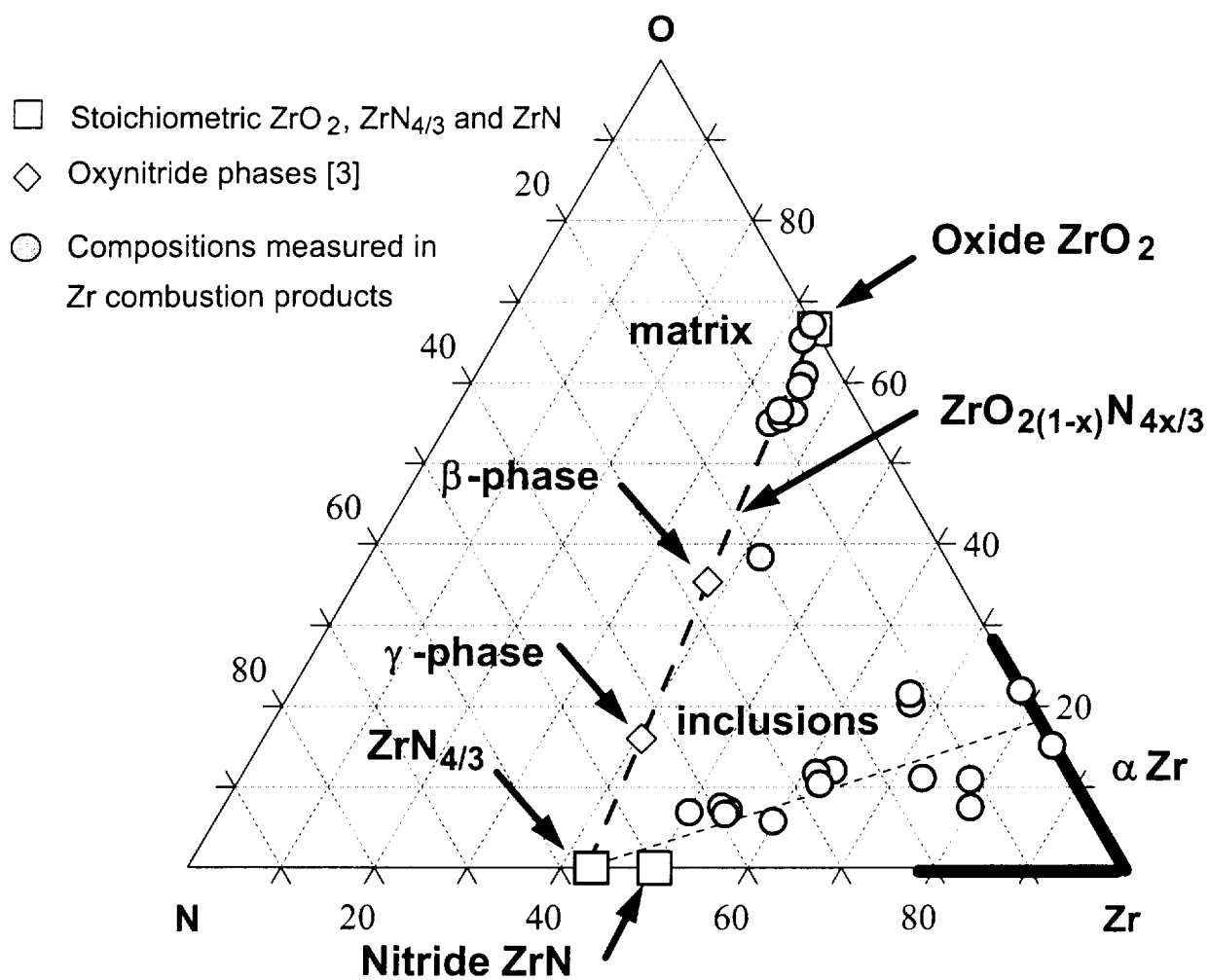


Fig. 6.2. Atomic proportions of zirconium combustion products measured by x-ray microanalysis. Bold line marked  $\alpha\text{Zr}$  represents an area of known solid solutions of nitrogen and oxygen in zirconium.

## 7. NEW TECHNOLOGY

No patentable or non-patentable discoveries or applications have been developed or found in the course of this project.

## 8. SUMMARY AND FUTURE WORK

Physical characteristics of the combustion of metal particle groups have been addressed in this research. The combustion behavior and interaction effects of multiple metal particles has been studied using a microgravity environment, which presents a unique opportunity to create an "aerosol" consisting of relatively large particles, i.e., 50-300  $\mu\text{m}$  diameter. Combustion behavior of such an aerosol could be examined using methods adopted from well-developed single particle combustion research. The experiment included fluidizing relatively large (order of 100  $\mu\text{m}$  diameter) uniform metal particles under microgravity and igniting such an "aerosol" using a hot wire igniter. The flame propagation and details of individual particle combustion and particle interaction have been studied using a high speed movie and video-imaging with cameras coupled with microscope lenses to resolve individual particles. Interference filters were used to separate characteristic metal and metal oxide radiation bands from the thermal black body radiation. Recorded flame images were digitized and various image processing techniques including flame position tracking, color separation, and pixel by pixel image comparison were employed to understand the processes occurring in the burning aerosol. The development of individual particle flames, merging or separation, and extinguishment as well as induced particle motion have been analyzed to identify the mechanisms governing these processes. Size distribution, morphology, and elemental compositions of combustion products were characterized and used to link the observed in this project aerosol combustion phenomena with the recently expanded mechanism of single metal particle combustion.

The results of the program have provided new insight into the mechanism of flame propagation in two-phase systems. The following new phenomena have been observed: monotonic increase in the powder number density (and, thus, equivalence ratio) in the unburnt aerosol ahead of the propagating flame; effect of the transport processes in the flame zone on the combustion product morphology; and formation of new metastable metal-gas phases during combustion. The analyses of the experimental results have shown that metal-gas solutions that are produced in burning metal particles affect the morphology and composition of the products formed in metal particle cloud combustion.

Since a new experimental apparatus and technique have been developed and tested in this program, only a limited number of experiments were conducted and only three metals were used in these experiments. Thus, more experiments are needed and, therefore, a renewal proposal for this project is planned to be submitted in response to the next microgravity combustion NRA. In particular, it will be proposed to expand the range of materials used in the microgravity experiments. A comprehensive set of experiments with Ti powder will be conducted and other metal and non-metal powders will also be used. This will enable us to compare the mechanism of flame propagation in various two-phase systems. In addition,  $\text{CO}_2$  oxidizer will be proposed for a series of experiments instead of air to address both fundamental effects of chemical reaction mechanism

REPORT DOCUMENTATION PAGE			Form Approved OMB No. 0704-0188	
Public reporting burden for this collection of information is estimated to average 1 hour per response, including the time for reviewing instructions, searching existing data sources, gathering and maintaining the data needed, and completing and reviewing the collection of information. Send comments regarding this burden estimate or any other aspect of this collection of information, including suggestions for reducing this burden, to Washington Headquarters Services, Directorate for Information Operations and Reports, 1215 Jefferson Davis Highway, Suite 1204, Arlington, VA 22202-4302, and to the Office of Management and Budget, Paperwork Reduction Project (0704-0188), Washington, DC 20503.				
1. AGENCY USE ONLY (Leave blank)	2. REPORT DATE 31 August, 1991	3. REPORT TYPE AND DATES COVERED Final report, 1 July 1996 - 31 August 1999		
4. TITLE AND SUBTITLE Interaction of Burning Metal Particles		5. FUNDING NUMBERS C NAS3-96017		
6. AUTHORS Edward L. Dreizin, Charles H. Berman, Vern K. Hoffmann				
7. PERFORMING ORGANIZATION NAME(S) AND ADDRESS(ES) AeroChem Research Laboratory Titan Corporation P.O. Box 2229 50 Washington Road Princeton, NJ 08543-2229		8. PERFORMING ORGANIZATION REPORT NUMBER TP 579		
9. SPONSORING/MONITORING AGENCY NAME(S) AND ADDRESS(ES) NASA Glenn Research Center 21000 Brookpark Road Cleveland OH 44135-3191		10. SPONSORING/MONITORING AGENCY REPORT NUMBER		
11. SUPPLEMENTARY NOTES Robert Friedman, NASA Contracting Officer's Technical Representative				
12a. DISTRIBUTION/AVAILABILITY STATEMENT UL		12b. DISTRIBUTION CODE		
13. ABSTRACT (Maximum 200 words)  Physical characteristics of the combustion of metal particle groups have been addressed in this research. The combustion behavior and interaction effects of multiple metal particles has been studied using a microgravity environment, which presents a unique opportunity to create an "aerosol" consisting of relatively large particles, i.e., 50-300 • m diameter. Combustion behavior of such an aerosol could be examined using methods adopted from well-developed single particle combustion research. The experiment included fluidizing relatively large (order of 100 • m diameter) uniform metal particles under microgravity and igniting such an "aerosol" using a hot wire igniter. The flame propagation and details of individual particle combustion and particle interaction have been studied using a high speed movie and video-imaging with cameras coupled with microscope lenses to resolve individual particles. Interference filters were used to separate characteristic metal and metal oxide radiation bands from the thermal black body radiation. Recorded flame images were digitized and various image processing techniques including flame position tracking, color separation, and pixel by pixel image comparison were employed to understand the processes occurring in the burning aerosol. The development of individual particle flames, merging or separation, and extinguishment as well as induced particle motion have been analyzed to identify the mechanisms governing these processes. Size distribution, morphology, and elemental compositions of combustion products were characterized and used to link the observed in this project aerosol combustion phenomena with the recently expanded mechanism of single metal particle combustion.				
14. SUBJECT TERMS microgravity metal aerosol combustion, two-phase system combustion		15. NUMBER OF PAGES 88		
		16. PRICE CODE		
17. SECURITY CLASSIFICATION OF REPORT UNCLASSIFIED	18. SECURITY CLASSIFICATION OF THIS PAGE UNCLASSIFIED	19. SECURITY CLASSIFICATION OF ABSTRACT UNCLASSIFIED	20. LIMITATION OF ABSTRACT UL	